Charge Carrier Dynamics in Hybrid Systems for Solar Energy Conversion

Dissertation

zur Erlangung des Grades

„Doktor der Naturwissenschaften“

im Promotionsfach Chemie

am Fachbereich Chemie, Pharmazie und Geowissenschaften

der Johannes Gutenberg-Universität

in Mainz

Max-Planck-Institut für Polymerforschung

Melike Karakuş Uzuner

geb. in İstanbul / Türkei

Mainz, 2017

Tag der mündlichen Prüfung: 15.05.2017

I hereby declare that I wrote this dissertation submitted without any unauthorized external assistance and used only sources acknowledged in the work. All textual passages which are appropriated verbatim or paraphrased from published and unpublished texts as well as all information obtained from oral sources are duly indicated and listed in accordance with bibliographical rules. In carrying out this research, I complied with the rules of standard scientific practice as formulated in the statutes of the Johannes Gutenberg University Mainz to insure standard scientific practice.

Melike Karakuş-Uzuner

Publications covered in this thesis

1- **M. Karakus**, S. A. Jensen, F. D'Angelo, D. Turchinovich, M. Bonn, E. Cánovas "Phonon-Electron Scattering Limits Free Charge Mobility in Methylammonium Lead Iodide Perovskites" The Journal of Physical Chemistry Letters, 2015, 24, 4991–4996.

2- **M. Karakus**, W. Zhang, H. J. Räder, M. Bonn, E. Cánovas "Electron transfer from 4,4'-dicarboxylic acid-2,2'bipyridine emerges upon dye photodegradation in N3 sensitized TiO_2" submitted.

3- **M. Karakus**, Y. Sung, H. Wang, Z. Mics, K. Char, M. Bonn, E. Cánovas "Correlating Carrier Dynamics and Photocatalytic Hydrogen Generation in Pt Decorated CdSe Tetrapods" accepted Journal of Physical Chemistry C.

Publications not covered in this thesis

4- E. Cánovas, H. Wang, **M. Karakus**, M. Bonn "Hot Electron Transfer from PbSe Quantum Dots Molecularly Bridged to Mesoporous Tin and Titanium Oxide Films" Chemical Physics, 2015, doi:10.1016/j.chemphys.2015.11.005.

5- H. Kim, E. Cánovas, **M. Karakus**, Z. Mics, M. Grechko, D. Turchinovich, S. H. Parekh, J. Hunger, M. Bonn "Coherent phonon-induced modulation of the optical band gap in methylammonium lead halide perovskites" submitted.

6- C. Yang, K. S.n Schellhammer, F. Ortmann, S. Sun, R. Dong, **M. Karakus**, Z. Mics, M. Löffler, F. Zhang, X. Zhuang, E. Cánovas, G. Cuniberti, M. Bonn, X. Feng "Coordination Polymer Framework-Based On-Chip Micro-Supercapacitors with AC Line-Filtering Performance" Angew. Chem. Int. Ed. 2017, 10.1002/anie.201700679.

Conference contributions

1- International Conference on Charge Carrier Dynamics at the Nanoscale (CCDNano16), (Germany), 12-13 Sep "Phonon-Electron Scattering Limits Free Charge Transport in Methylammonium Lead Halide Perovskites" *(poster presentation).*

2- International Conference on Charge Transfer and Transport at the Nanoscale (CTTN15), (Spain), 13-15 Sep "Phonon-Electron Scattering Limits Free Charge Transport in Methylammonium Lead Halide Perovskites" *(oral presentation).*

3- 2015 MRS Spring Meeting and Exhibit, (USA), 6-10 Apr 2015 "Phonon Scattering Impedes Charge Mobility in Methylammonium Lead Halide Perovskites" *(oral presentation)*

4- Hybrid and Organic Photovoltaics (HOPV14), (Switzerland), 11-14 May 2014 "Enhanced Electron Transfer in Dye Sensitized Oxides" *(poster presentation).*

Summary

This thesis covers the fundamental understanding of key processes; specifically, charge carrier dynamics, in hybrid systems with relevance in energy production (via solar cells) and energy storage (via water splitting). Charge carrier dynamics, including charge generation, interfacial charge transfer and charge transport, are interrogated by using time-resolved terahertz spectroscopy (TRTS) technique. The thesis is organized as follows:

Chapter 1: Introduction

Here we briefly introduce intrinsic loss mechanisms and efficiency limits in photoconversion, and some examples of photoconversion processes as: perovskite solar cells and dye sensitized solar cells for energy production and photocatalytic hydrogen generation for energy storage.

Chapter 2: Experimental technique, materials and sample preparations

In this chapter, we present time-resolved terahertz spectroscopy (TRTS) as a technique to investigate charge carrier dynamics and the nature of the charge transport in hybrid systems. Specifically, we present how to extract the frequency resolved photoconductivity from THz data and how to monitor charge carrier dynamics by TRTS measurements in a pump-probe scheme. A description of materials and sample preparation protocols used throughout the thesis are also presented.

Chapter 3: Phonon-Electron Scattering Limits Free Charge Mobility in Methylammonium Lead Iodide Perovskites

In this chapter, we study the temperature dependent charge carrier dynamics and complex valued photoconductivity in solution-processed films of methylammonium lead iodide perovskite to explain the nature of photo-generated charges (whether free carriers, excitons or both) and the nature of the charge transport. We find that the main photo-generated species are free carriers (rather than excitons). The nature of the conductivity is Drude-like and free charge carrier motion is characterized by an average scattering time. The scattering time determined from Drude fits shows a $\sim T^{-3/2}$ dependence (temperature range $150 < T < 300$ K); this figure approaches the theoretical limit for pure acoustic phonon (deformation

potential) scattering. Hence, we conclude that electron-phonon, rather than impurity scattering, sets the upper limit on free charge transport for this hybrid perovskite material.

Chapter 4: Electron transfer from 4,4'-dicarboxy-2,2'-bipyridine emerges upon dye photodegradation in N3 sensitized TiO_2

In this chapter, we study the evolution of interfacial electron transfer (ET) dynamics in N3 dye sensitized mesoporous TiO_2 electrodes upon controlled sensitized electrode photodegradation. We demonstrate that a sub-ps ET signal emerges and becomes practicaly time-invariant upon full photodegradation of the N3 dye. Notably, the amplitude signal corresponds to ~50 % of the original TRTS signal prior sample photodegradation. Frequency-resolved complex photoconductivity measurements confirm that the signal emerging upon full dye decomposition into fragments refers to free carriers populating the oxide conduction band. From Laser Desorption Ionization Mass Spectrometry (LDI-MS), ATR-FTIR spectroscopy and time-resolved terahertz spectroscopy (TRTS) we analyze the chemical identity of the compound from which this sub-ps ET component originates; we find that 4,4'-dicarboxy-2,2'-bipyridine remains anchored to the oxide surface upon full N3 dye photodegradation.

Chapter 5: Correlating Carrier Dynamics and Photocatalytic Hydrogen Generation in Pt Decorated CdSe Tetrapods

In this chapter, we study platinum cocatalyst decorated CdSe tetrapods as a function of Pt nanoparticle size by correlating carrier dynamics and photocatalytic hydrogen generation efficiency. We find that while the capture rate of photogenerated electrons from CdSe to the Pt nanoparticles (co-catalyst) increases as a function of Pt size, the photocatalytic H_2 generation is reduced for tetrapods decorated with larger Pt particles. Our results demonstrate the presence of a kinetic competition between electron transfer at the CdSe/Pt interface and electron transfer at the Pt / H_2O interface. This trade-off defines an optimum Pt size for photocatalytic H_2 generation in Pt decorated CdSe tetrapods.

Chapter 6: Conclusions and Outlook

In this chapter, we briefly summarize the general conclusions and outlook relevant for the studies in this thesis.

Zusammenfassung

Ladungsträgerdynamik in Hybridsystemen für Solarenergieumwandlung

Diese Arbeit behandelt das grundlegende Verständnis vom Schlüsselprozessen – insbesondere der Ladungsträgerdynamik – in Hybridssystemen mit Relevanz in der Stromerzeugung (im Solarzellen) und Energiespeicherung (über Wasserspaltung). Ladungsträgerdynamik, einschließlich Ladungserzeugung, Grenzflächenladungstransfer und Ladungstransport, wird unter Verwendung um zeitaufgelöster Terahertzspektroskopie (TRTS) Technik untersucht. Die Arbeit ist wie folgt gegliedert:

Kapitel 1: Einleitung

Im ersten Kapitel werden intrinsische Verlustmechanismen und Effizienzgrenzen in der Photokonversion vorgestellt – und einige Beispiele für Photokonversionsprozesse wie: Perovskit-Solarzellen und farbstoffsensibilisierte Solarzellen für die Energieproduktion und photokatalytische Wasserstofferzeugung zur Energiespeicherung.

Kapitel 2: Experimentelle Technik, Werkstoffe und Probenvorbereitung

In diesem Kapitel wird die zeitaufgelöste Terahertz-Spektroskopie (TRTS) als Technik zur Untersuchung der Ladungsträgerdynamik und der Art des Ladungstransports in Hybridsystemen vorgestellt. Speziell wird darauf eingegangen, wie man die frequenzaufgelöste Fotoleitfähigkeit aus THz-Daten extrahiert und wie man die Ladungsträgerdynamik durch TRTS-Messungen in einem Pump-Sonden-Schema erforscht. Des Weiteren erfolgt eine Beschreibung der Materialien und Probenvorbereitungsprotokolle, die während der gesamten Arbeit verwendet wurden.

Kapitel 3: Phonon-Elektronen-Streuungsgrenzen Freie Ladungsmobilität in Methylammoniumbleiiodid-Perowskiten

In diesem Kapitel wird die temperaturabhängige Ladungsträgerdynamik und die komplexwertige Photoleitfähigkeit in lösungsverarbeiteten Filmen von Methylammoniumbleiiodid-Perowskit untersucht, um die Art der photogenerierten Ladungen (ob freie Träger, Exzitonen oder beides) und um die Art des Ladungsstransport zu erläutern. Es wird gezeigt, dass die hauptfotogenerierten Ladungen frei beweglich sind

(anstatt Exzitonen), die Art der Leitfähigkeit dem Drude-Modell folgt und freie Ladungsträgerbewegung durch eine durchschnittliche Streuzeit gekennzeichnet ist. Die fits zum Drude-Modell ermittelte Streuzeit zeigt eine ~ $T^{-3/2}$ -Abhängigkeit (Temperaturbereich 150 K < T < 300 K) und nähert sich der theoretischen Grenze für rein akustische Phononen-Streuung (Deformationspotential). Daher schließen wir, dass Elektron-Phonon-Wechselwirkung, anstatt Verunreinigungsstreuung, dem freien Ladungstransport im diesen Perowskit begrenzt.

Kapitel 4: Elektronenübertragung aus 4,4'-Dicarbonsäure-2,2'-bipyridin tritt bei der Farbstoff-Photooxidation in N3-sensibilisierten TiO_2-Elektroden auf

In diesem Kapitel wird die Entwicklung der Grenzflächen-Elektronenübertragungsdynamik in N3-Farbstoff-sensibilisierten mesoporösen TiO_2-Elektroden bei kontrollierter Elektroden-Photooxidation untersucht. Es wird gezeigt, dass ein Subpicosecond-Elektronentransfersignal auftritt und bei voller Photodegradation des N3-Farbstoffs Zeitunabhängig wird; vor allem die Signale halbieren sich nach der Photodegradation. Frequenzaufgelöste komplexe Photoleitfähigkeitsmessungen bestätigen, dass das bei der Oxidation auftretende Signal sich auf freie Träger bezieht, die das Oxidleitungsband belegen. Aus der Laser-Desorption/Ionisation-Massenspektrometrie (LDI-MS), der ATR-FTIR-Spektroskopie und der zeitaufgelösten Terahertz-Spektroskopie (TRTS) Analyse wird gezeigt, dass das N3 Photoprodukt dcbpy (4,4'-Dicarbonsäure-2, 2'-bipyridin) ist verantwortlich für das beobachtete Subpicosecond-Elektronentransfersignal ist.

Kapitel 5: Korrelierende Trägerdynamik und photokatalytische Wasserstofferzeugung in Pt-dekorierten CdSe-Tetrapoden

In diesem Kapitel werden Ladungsträgerdynamiken in hybriden, mit Platinnanopartikeldekorierten CdSe-Tetrapoden als Funktion der Pt-Nanopartikelgröße untersucht, um die Trägerdynamik und die photokatalytische Wasserstofferzeugungseffizienz zu korrelieren. Die Ergebnisse zeigen die Präsenz einer kinetischen Konkurrenz zwischen den Elektroneneinfang an der CdSe / Pt-Schnittstelle, die mit der Pt-Nanopartikelgröße zunimmt, und der Elektronenfreisetzung an der Pt / H_2O-Grenzfläche, die mit der Nanopartikelgröße abnimmt. Dieser Trade-off definiert ein

Optimum für die photokatalytische H_2-Erzeugung in Pt-dekorierten CdSe-Tetrapoden als Funktion der Pt-Größe.

Kapitel 6: Schlussfolgerungen und Ausblick

In diesem Kapitel fassen wir kurz die allgemeinen Schlussfolgerungen und Aussichten zusammen, die für die Studien in dieser Arbeit relevant sind.

Abbreviations and list of symbols

AM	Air mass
Al_2O_3	Aluminum oxide
CdSe	Cadmium selenide
CB	Conduction band
Cl	Chlorine
dcbpy	4,4′-dicarboxy-2,2′-bipyridine
DOS	Density of states
D_L	Diffusion length
DSSCs	Dye sensitized solar cells
DMF	N,N-Dimethylformamide
e	Electron
Eg	Band gap
ET	Electron transfer
ETL	Electron transport layer
FFT	Fourier transformation
FWHM	Full width at half maximum
ΔG	Gibbs free energy
h	Hole
HOMO	Highest occupied molecular orbital
HTM	Hole transport material
Im [σ]	Imaginary conductivity
IR	Infrared
K	Kelvin
µ	Mobility
m*	effective carrier mass
$MAPbI_3$	Methylammonium lead triiodide
MLCT	Metal to ligand charge transfer
LDI-MS	Laser desorption ionization mass spectrometry
N	Charge carrier density

N3	Ru(4,4'-dicarboxylicacid-2,2'-bipyridine)$_2$(NCS)$_2$
Nb_2O_5	Niobium pentoxide
O.D.	Optical density
LUMO	Lowest unoccupied molecular orbital
$\sigma(\omega)$	Complex conductivity
Pt	Platinium
Re [σ]	Real conductivity
SEM	Scanning electron microscopy
STH efficiency	Solar to hydrogen conversion efficiency
SnO_2	Tin (IV) oxide
SQ limit	Shockley–Queisser limit
T	Temperature
TEM	Transmission electron microscopy
TiO_2	Titanium oxide
THz	Terahertz
TRTS	Time-resolved terahertz spectroscopy
TRPL	Time-resolved photoluminescence spectroscopy
τ_s	Scattering time
UV	Ultraviolet
VIS	Visible
VB	Valence band
WZ	Würtzite
XRD	X-ray Diffraction
ZB	Zinc blende
ZnO	Zinc oxide
ZnTe	Zinc telluride

Table of Contents

Chapter 1

Introduction

Addressing the ever-growing energy demand of the world is one of today's most challenging problems. This is because the consumption of resources have raised in proportion with the population and because non-renewable energy resources, such as oil, coal and natural gas, are causing severe environmental problems, such as the climate change by harmful byproduct emissions, e.g. CO_2 emissions (see footnote [1]). In order to confront this scenario, solar energy conversion represents a clean energy source in terms of being abundant, environmentally friendly and renewable. Making inexpensive, efficient, room temperature processable and environmently-friendly materials for solar energy conversion represents a great challenge (see footnote [2]). Several novel materials and architecutres have emerged as promising candidates for solar energy conversion, such as organic-inorganic hybrid perovskites, dye sensitized oxides, nanostructured photocatalyst, metal-organic frameworks…etc. For these library, fundamental understanding of charge carrier dynamics is urgently needed for further boost the their efficiencies. The motivation of this thesis is to investigate charge carrier dynamics, charge transport and interfacial charge transfer in photoactive hybrid systems which are promising candidates for solar energy conversion technologies, such as solar cells (coversion of solar energy into electricity) and photocatalysis (conversion of solar energy into chemical energy). Hybrid systems studied in this thesis include organic-inorganic components (organic-inorganic hybrid perovskites), molecules-metal oxide interfaces (dye sensitized oxides) and noble metal-nanocrystals (metal decorated tetrapods).

[1] Energy and Air Pollution 2016 - World Energy Outlook Special Report, http://www.worldenergyoutlook.org

[2] World Energy Assessment-2000.pdf

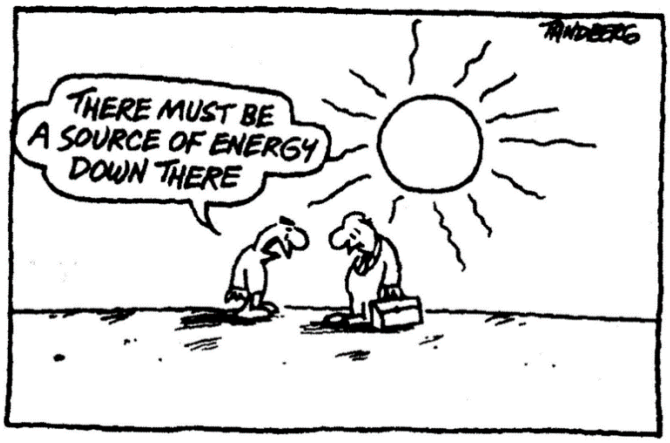

Figure 1.1 Solar energy (see footnote [3]).

1.1 Intrinsic loss mechanisms in photoconversion

To supply the energy demand of the world, considerable effort has been made to produce electricity and fuels (such as hydrogen, methane and methanol) from solar energy via solar cells and photocatalysis. The solar energy conversion efficiency of such systems depends strictly on the efficient light absorption through VIS to IR range, charge separation and charge transport processes in materials.[1] In this thesis, we focus our discussion on the fundamental understanding of charge transport and charge transfer in hybrid systems for solar cell and photocatalytic hydrogen generation applications.

The hybrid systems studied in this thesis, contain photoactive materials for absorbing the sunlight energy. The absorption of a photon from sunlight promotes an electron from a ground state (eg. valence band, VB or highest occupied molecular orbital, HOMO) to an excited state (e.g. the conduction band, CB or lowest unoccupied molecular orbital, LUMO). The photogenerated charges (electron in the excited state and hole in the ground state) in these photoactive materials either move freely (characteristic for inorganic semiconductors)[2] or form excitons depending on the exciton binding energy for the given material relative to kT. To harvest the photogenerated charge carriers for producing electricity or chemical energy, the electrons and holes must be separated and transported to the opposite electrodes inside a cell. The electron and hole transport may be disrupted by physical and

[3] http://thebreakthrough.org/archive/in_love_with_the_sun

energetical barriers and/or trapping sites. This implies that not all the charge carriers can be collected and finally contribute to the photocurrent, which limits the efficiency of the photoconversion process. Furthermore, there are several other intrinsic loss mechanisms for solar energy conversion processes which define the maximum attainable photoconversion efficiency:[3,4] (1) transmission loss and (2) thermal energy loss.

1.1.1 Transmission loss

As discussed in the previous section, the first step for an efficient solar energy conversion process is the absorption of sunlight. Figure 1.2a shows the AM1.5 solar irradiation spectrum reaching the earth surface; the intensity of sunlight peaks at visible range while the IR energies (wavelength higher than 800 nm) represents a substantial portion of the solar spectrum. To harvest efficiently the sunlight in a photoelectrochemical cell, the bandgap (Eg) energy (representing the difference between the energy of the ground state or VB, and that of the excited state or CB, of the photoactive material) is required to have an optimal value[3] in order to reduce losses given the available solar radiation at the earth's surface. This is because only photons with energies above Eg can promote an electron from VB to CB (or from the ground to the excited state). Therefore, photons with lower energy than the Eg will be transmitted through the material and will not contribute to the photoconversion process. For a wide bandgap (Eg) semiconductor (e.g. Eg > 3 eV), only photons with high-energy at the UV side of the solar spectrum can be absorbed while Vis-IR portion of the solar spectrum will be completely lost (see Figure 1.2b). On the other hand, a narrow Eg semiconductor (e.g. with Eg < 1 eV) is able to absorb a broad range of the solar spectrum (see Figure 1.2c). One might then think that narrow bandgap will be always favourable for high photoconversion efficiency (as it will produce large photocurrent). This is not the case if one accounts for thermal losses associated with the absorption of photons with energy exceeding the Eg onset.

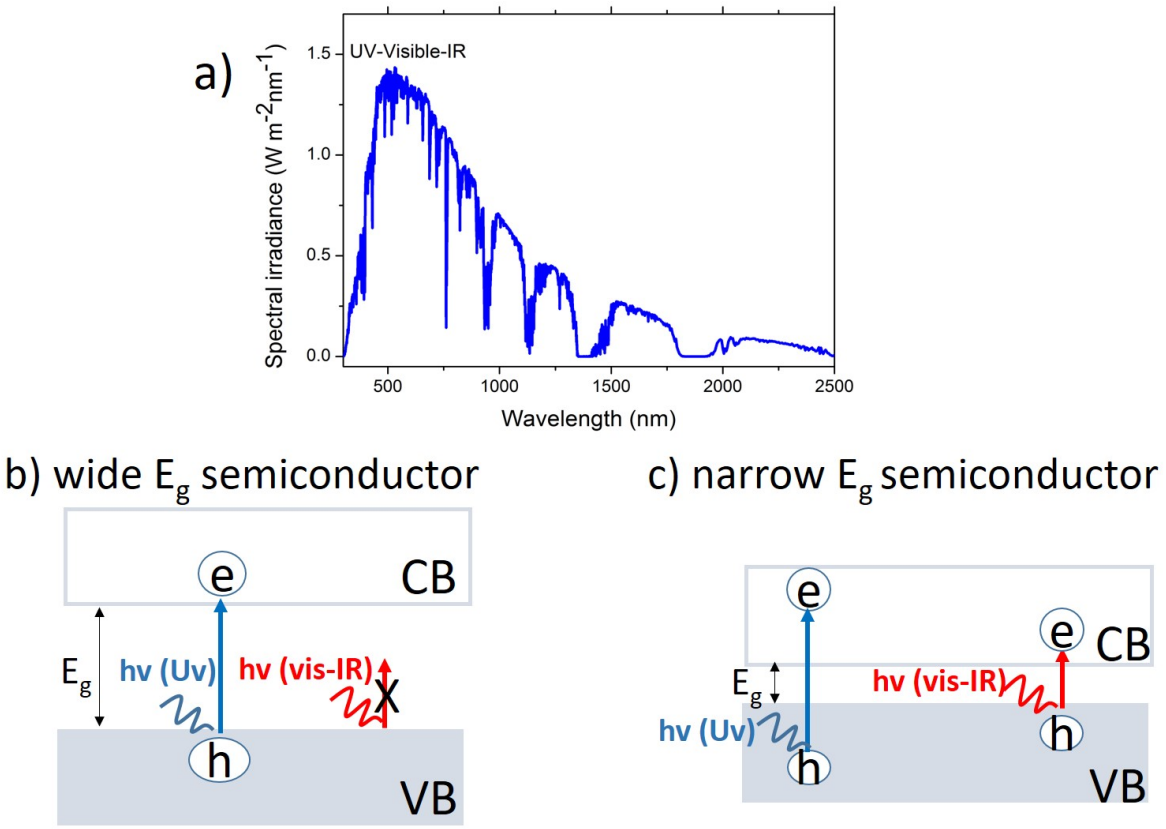

Figure 1.2 a) AM 1.5 Solar spectrum (see footnote [4]), b) The absorption of solar radiation for the case of a wide bandgap (Eg) semiconductor versus c) narrow bandgap (Eg) semiconductor. The energy range of incoming photons (hv) are represented as UV, Vis, IR.

1.2.2 Thermal energy loss

Photons with energy higher than the Eg energy of the active material can be absorbed efficiently; however, the excess photon energy is dissipated in the absorber as heat. Just after photon absorption, the "hot carriers" relax to the band edges via emission of phonons (see Figure 1.3). This proccess is often called thermalization or cooling of hot carriers. Narrow Eg absorbers, though absorbing a large fraction of the solar spectrum will have major losses associated with thermalization. This illustrates that a trade-off exists for maximum photoconversion efficiency.

[4] graph is plotted with the data taken from *http://www.pveducation.org/pvcdrom/appendices/standard-solar-spectra*

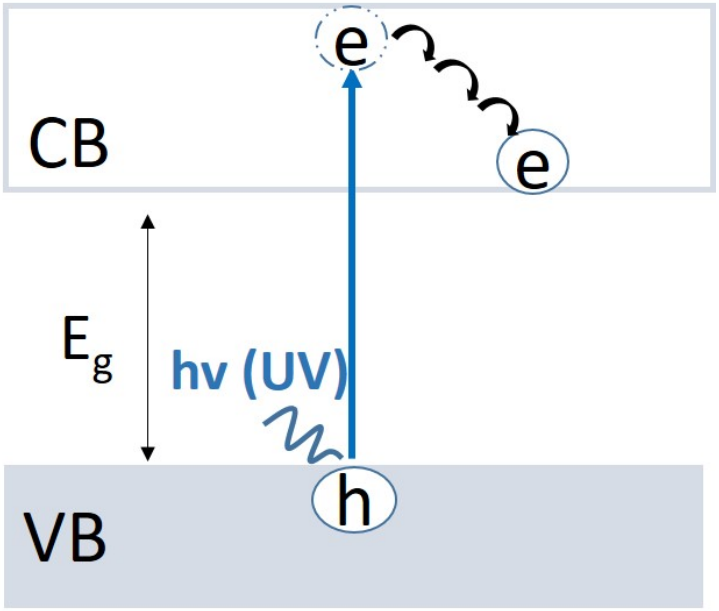

Figure 1.3 Sketch illustrating multiphonon relaxation from a hot electron in a semiconductor: Uv light is absorbed by a semiconductor that promotes electron from valence band (VB) to conduction band (CB) and leaves a hole behind in the VB. The excess energy is dissipated via multiphonon relaxation from the hot electron.

1.2 Efficiency limits of photoconversion

By considering transmission and thermal losses in a semiconductor given the solar spectrum, the optimum performance in a single junction solar cell based on a semiconductor achieved with a material with a Eg ~1.35 eV as ~33 %. This is known as the Shockley-Queisser (S-Q) limit (see Figure 1.4).[3] By using this approach, the maximum efficiency for solar to hydrogen (STH) for water splitting can also be estimated (~31 % for ~1.2 Eg semiconductor[4]). A summary for the dependence of theoretical STH efficiencies versus band edge positions of commonly used semiconductors is shown in reference [5].

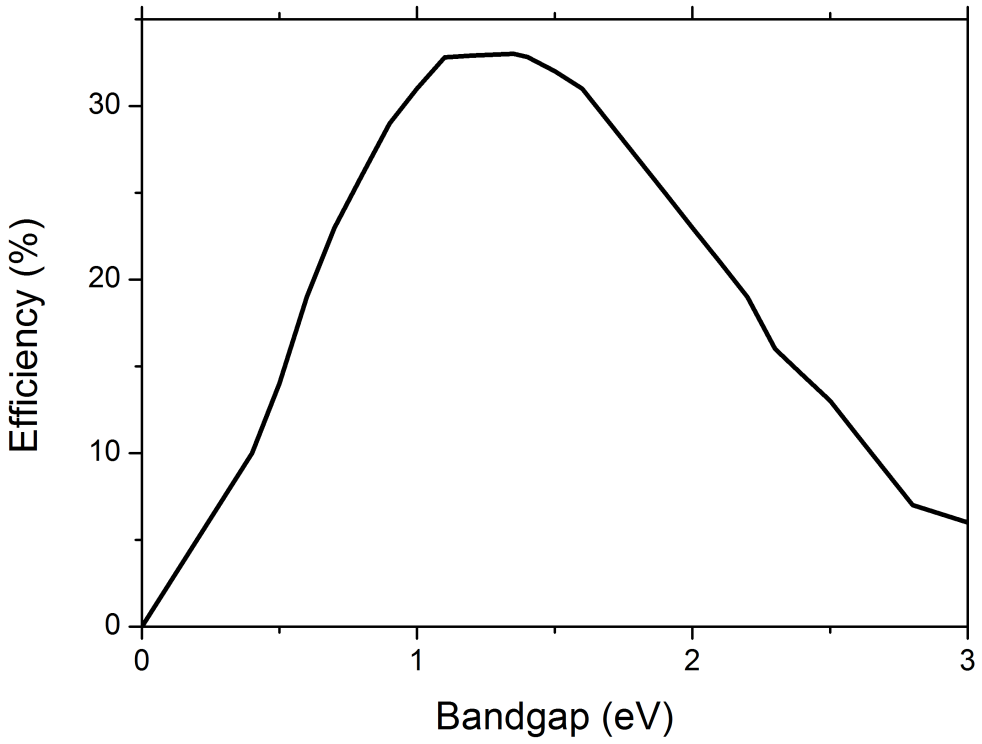

Figure 1.4 Dependence of efficiency versus band gap (Eg) for a semiconductor determined by Shockley-Queisser (SQ) limit (adapted from ref [3]).

1.3 Perovskite solar cells

Perovskite solar cells based on organic-inorganic hybrid perovskites (used as photoactive materials providing tunable band gaps 1.3-2.5 eV),[6] such as methylammonium lead triiodide ($MAPbI_3$), formamidinium lead triiodide ($FAPbI_3$), methylammonium lead tribromide ($MAPbBr_3$), methylammonium tin triiodide ($MASnI_3$), have showed an unprecedented rapid progress from 3.8 % efficiency to 22.1 % within the last six years (see footnote [5]).

Although these perovskites were synthesized and their semiconducting properties were investigated in the late 90's, they were applied for the first time in a mesoscopic solar cell architecture containing liquid electrolyte (~3.8 % photoconversion efficiency) in 2009.[7] As this material easily dissolves in the liquid environment, the stability of the reported

[5] NREL best research cell efficiency chart

device was very poor.[7] Later, solar cell with better stability and higher efficiency (~6.5 %) was achieved by replacing the liquid electrolyte with a solid hole transport material (HTM) and changing the deposition method of the perovskite layer.[8] An important finding was reported by Lee et al[9] that a mesoporous Al_2O_3 scaffold (which is unable to accept electrons from the perovskite owing to its higher lying CB level than CB of the perovskite) provided photoconversion efficiency of ~10.9 % which was similar with the efficiency of a device based on TiO_2 electrode (which is expected to assist electron extraction from excitons populating the perovskite). This study demonstrated that the perovskite itself could transport electrons to the external electrodes; and hence, suggested that a mesoscopic architecture could be replaced by a planar device structure. This was also supported by a study using the perovskite in a mesoscopic device architecture lacking a HTM.[10] This mesoscopic architecture provided the efficiency of 12.8 %, suggesting that these materials could transport holes as efficienctly as electrons. In line with these studies, transistor measurements have confirmed that $MAPbI_3$ perovskites are ambipolar; they are able to transport both electrons and holes.[11,12] These findings opened a new path towards planar solar cell applications (Figure 1.5-right) instead of mesoscopic architectures (Figure 1.5-left). However, the potential benefit, if any, of employing any mesoscopic scaffold in these devices has remained debated.[13–17] The presence or absence of excitons in perovskite materials is crucial to determine a plausible positive role for a mesoporous electrode rather than a planar one.

The working principle of an mesoscopic solar cell is sketched in Figure 1.5 as:[18,19] (a) a sensitizer (perovskite) anchored to a wide band gap semiconductor (such as TiO_2 or SnO_2) absorbs a photon that leads to the formation of an exciton (electron-hole pairs bonded by Coulombic interactions). Subsequently, (b) ET occurs from the sensitizer to the semiconductor by leaving a hole behind in the ground state of the sensitizer. (c) Then, a HTM, such as liquid or solid electrolyte, provides an electron to the sensitizer in order to regenerate the sensitizer, and (d) injected electron from the sensitizer is transported through the oxide phase and reach the negative electrode to complete the circuit. The characterization of these processes can be routinely done by time-resolved spectroscopic

methods, such as transient absorption,[15] terahertz,[20] and microwave[21] conductivity techniques.

On the other hand, the working principle of a planar p-i-n perovkite solar cell is expected to follow a sequence consisting of (Figure 1.5-right):[17,18] (e) photoactive perovskite layer absorbs a photon from sunlight that generates free electron and hole, (f) electron is transported within the perovskite layer (in this respect, diffusion lengths - D_L - larger than the pervoskite thickness are required, for Cl doped $MAPbI_3$ D_L > 1µm well beyond the thickness required for full sunlight absorption, approximately ~300 nm), (g) analogously the hole is transported within the perovskite layer towards counter electrode, while (h) electron transports towards the substrate electrode.

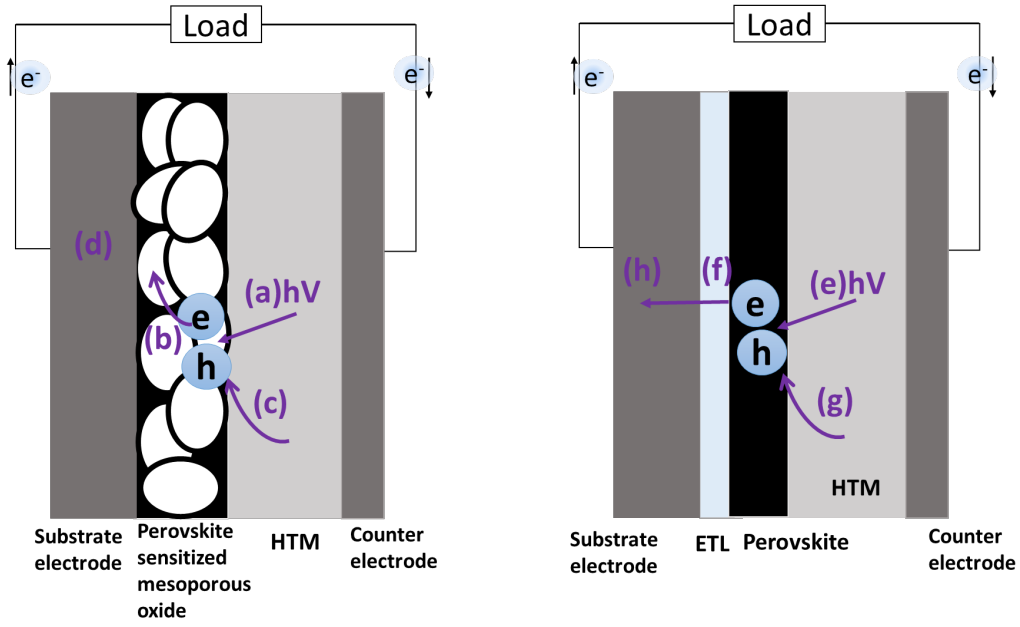

Figure 1.5 Perovskite solar cells; mesoscopic (left) versus b) planar (right) architecture. Left: (a) Photoexcitation of the sensitizer (perovskite) is followed by (b) electron injection towards the conduction band of the mesoporous oxide. (c) Hole transport layer (HTM) regenerates the perovskite, which itself is regenerated at the counter electrode by (d) electron coming from the substrate electrode passed through the load. Right: (e) Photoexcitation of the perovskite is followed by (f) extraction and (h) transport of electron from electron transport layer (ETL) towards the substrate electrode. (g) Hole transports from the hole transport layer (HTM) towards the counter electrode.

1.3.1 Organic-inorganic hybrid perovskites

Perovskites are the family of materials described by the formula ABX_3; they were named after L.A. Perovski who discovered this structure in the $CaTiO_3$ mineral in 1839.[19] In this thesis, we focus on one of the organic-inorganic hybrid perovskite types, namely methlyammonium lead triiodide ($CH_3NH_3PbI_3$ or $MAPbI_3$), which contains the organic ion CH_3NH_3, and inorganic ionic Pb and I_3 constituents as A, B and X in the general formula, respectively (Figure 1.6).

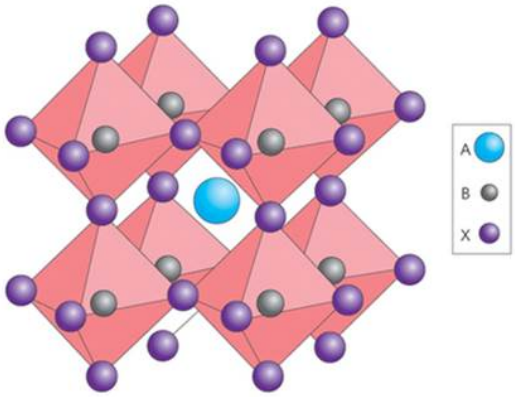

Figure 1.6 Cubic perovskite crystal structure (A= methylammonium ion (CH_3NH_3), B = Pb and X= the halogen ion (I or Cl) that forms at temperatures above 330 K (ref [18]).

These organic-inorganic hybrid perovskites have received a great attention for solar energy conversion applications owing to their high absorption coefficients, solution processability and Eg tunability.[6,13,18] Understanding chemical and physical properties of these hybrid materials has become crucial for development of materials and device performances. Although extensive studies relevant for these materials have been conducted, there are still many open questions regarding their stability,[13] toxicity[13] and their transport properties;[22,23] including factors limiting their mobility,[24] the nature of photogenerated charge carriers (whether excitons, free carriers or both)[14,18,25] and the relating choice of planar[26] versus mesoscopic device architectures.[27]

1.3.2 Charge transport in methlyammonium lead triiodide ($CH_3NH_3PbI_3$) perovskite film

An ideal photoactive material for photovoltaics should provide both efficient absorption and charge transport.[23,22] Organic-inorganic hybrid perovskites can, in principle, fulfill both of those requirements owing to the reported strong absorbance for their thin films and long diffusion lengths (D_L) for photogenerated charges (well beyond the optical thickness required for full absorption, 300 nm). Limited long range charge carrier transport has been commonly a drawback for low-temperature solution-processed photoactive films, prepared by techniques such as spin-coating and/or chemical bath deposition; as these films typically contain amorphous or polycrystalline phases[28,29] that necessarily impedes charge-carrier transport towards the external electrodes (exciton D_L - see footnote[6] - typically ~10 nm for semiconductor polymers).[30] Remarkably, solution processed organic-inorganic hybrid perovskite films provide long range charge carrier transport with characterisitic electron-hole D_L ranging from ~100 nm ($CH_3NH_3PbI_3$)[23] to more than 1 µm ($CH_3NH_3PbI_3$:Cl).[22] Studies analyzing their conductivity properties have reported that charge carriers are experiencing long lifetimes and diffusion lengths, indicating very low trap densities and hence slow recombination.[23,31–34] Even, these figures are found in polycrystalline films, this has been associated with the lack of grain boundary barriers and mid-gap defects at surfaces. Note however that long lifetimes do not necessarily correlate with high mobilities which are limited by scattering.[24]

Chapter 3 of this thesis is devoted to investigations into the nature of charge carrier transport and mobility in solution processed Cl doped methlyammonium lead triiodide ($CH_3NH_3PbI_3$:Cl) perovskite films by using TRTS (described in Chapter 2).

1.4 Dye sensitized solar cells (DSSCs)

The DSSC was first presented by O'Regan and Grätzel in their 1991 seminal paper.[35] DSSC is a photoelectrochemical cell where sunlight is converted into electricity. Over the last decade,

[6] Diffusion length; $D_L = \sqrt{\mu q / k_B T}$ where $\mu, q, k_B \; and \; T$ are mobility, electron charge, boltzman constant and temperature, respectively.

DSSCs have become promising for photovoltaic technology owing to their potential for high performances, flexibility in design and low cost production.[36] The initial efficiency of 7.9 %[35] using Ruthenium based molecular dye has been increased to 11.9 % (under air mass 1.5 irradiation (AM 1.5G) in small cells (area of 1.005 cm^2).[37] Also, large area DSSC modules (area of 100 mm x 100 mm) have been realized in a low cost roll-to-roll method, though with lower efficiencies when compared with small area devices.[38]

DSSC is a type of mesoscopic solar cell that is suited for the efficient collection of photogenerated excitons at electrolyte/dye/semiconductor interfaces. The working principle of a typical DSSC (as shown in Figure 1.7) is as follows:[35,39,40] (i) a molecular dye anchored to a wide band gap semiconductor (such as TiO_2, SnO_2 or ZnO) absorbs sunlight photon that generates an exciton in the dye molecule. (ii) The exciton is seperated at the dye/oxide interface if the LUMO of the dye is higher than the CB of the oxide by an electron transfer (ET) from the dye to the oxide. (iii) Subsequently, the dye molecule is regenerated by an electron coming from the electrolyte (e.g. iodide/triiodide) or a hole transport layer (e.g. spiro OMeTAD), while (iv) the free electron moves within the oxide (via diffusion controlled mechanism) towards the negative electrode to complete the circuit.

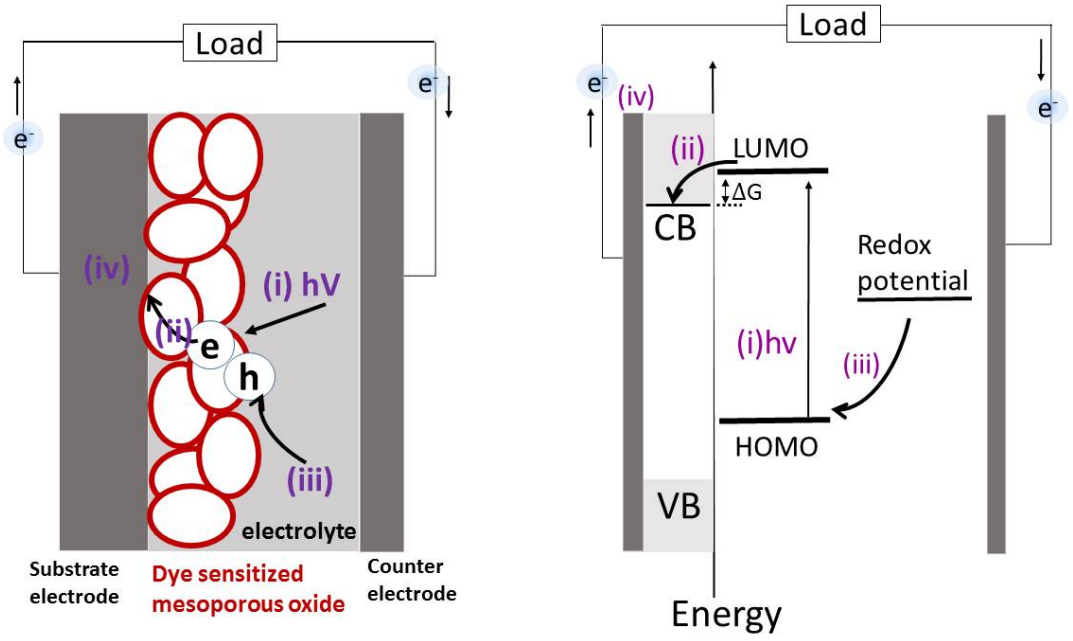

Figure 1.7 Principle of operation (left) and energy level scheme (right) of a dye sensitized solar cell (DSSC). (i) Photoexcitation of the dye promotes electron from the highest occupied molecular orbital (HOMO) to the lowest unoccupied molecular orbital (LUMO), followed by (ii) electron transfer towards the conduction band (CB) of the mesoporous oxide. (iii) An electrolye regenerates the dye molecule by providing an electron, which itself is regenerated at the counter electrode by an electron passing (iv) through the load.

In the operation of a DSSC, there are some possible pathways of losing charge carriers which can decrease the cell performance, such as (1) electron-hole recombination in the dye (occurs typically within millisecond timescales) which can compete with photo-induced ET (~femtosecond-nanosecond timescales), (2) recombination of the injected electron from the oxide's CB towards the dye's LUMO (~picosecond-nanosecond timescales) which can compete with the regeneration of the oxidized dye via hole transporting material (HTM) (lifetime of ~millisecond timescale) and/or (3) recombination of the free electron from the oxide's CB with the holes in the HTM (microsecond-millisecond timescale).[40,41]

1.4.1 Molecular dyes

Molecular dyes are used as sensitizers in DSSCs for harvesting sunlight energy. The ideal sensitizer for DSSCs should has a Eg of 1.35 eV according to the SQ limit (see section 1.2, Figure 1.4), for efficiently converting sunlight into electricity in a cell.[42] In addition, the molecular dyes should have an appropriate molecular head group, such as carboxylate or phosphonate, to anchor it to the semiconductor and enhance donor-acceptor coupling between the dye and the oxide. After dye photoexcitation, ideally, electrons must be transferred to the oxide with unity quantum yield (providing large photocurrent in devices). Futhermore, the lowest unoccupied molecular orbital (LUMO) of the dye should be matched well with the conduction band (CB) of the semiconductor oxide to minimize energetic losses during the electron transfer (promoting output circuit voltage in cells). This applies as well for the hole regeneration step between e.g. dye HOMO and VB of a solid state hole transport layer (HTM). Finally, the molecular dye should be stable during the device operation; market requirements are set on 20 years of exposure to the natural light. Therefore, common Ru dyes should be stable over ~10^8 turnover cycles.[40,42–44]

In this thesis, we mainly focus on Ruthenium metal complexes, namely N3 (Ru(4,4'-dicarboxylic acid-2,2'-bipyridine)$_2$(NCS)$_2$) (Figure 1.8), which is an intensively studied sensitizer, and so far has provided one of the best performances in DSSCs. In general, Ru-bipyridyl complexes, like N3, are efficient photosensitizers in DSSCs because of the long lifetimes of their excited states enabling efficient electron transfer (ET) (depending on the solvent/electrolyte environments, singlet states ^{1}MLCT and triplet states ^{3}MLCT of the Ru based molecular dyes are typically ranging from picosecond to nanosecond and nanosecond to millisecond timescales,[45] respectively). These photosensitizers are defined by electronic transitions in the UV and VIS regions such as metal centered (MC), ligand centered (LC), metal to ligand charge transfer (MLCT) and ligand to metal charge transfer (LMCT) . Also, the Ru metal center surrounded by bipyridyl ligands is an efficient redox (oxidation-reduction) architecture which is an advantage in DSSC operation.[44]

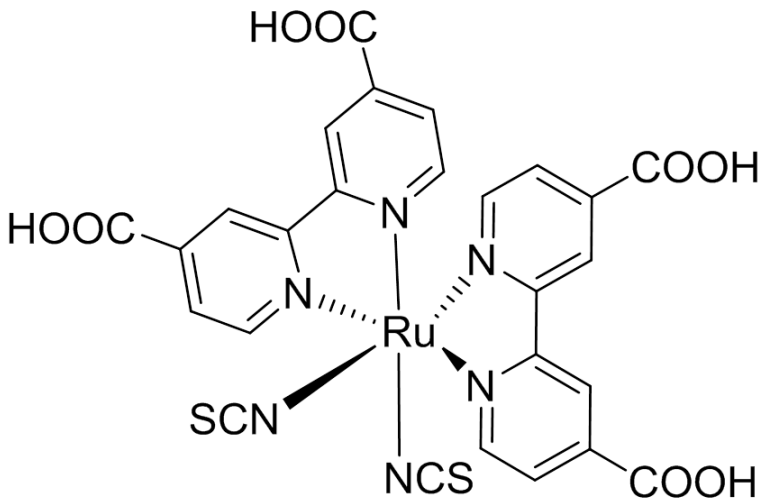

Figure 1.8 N3 (Ru(4,4'-dicarboxylic acid-2,2'-bipyridine)$_2$(NCS)$_2$) dye.

1.4.2 Mesoporous metal oxide

Metal oxides are wide band gap semiconductors (Eg ~ 3-4 eV) which are key elements for the operation of DSSCs. Electron injection from the sensitizer (molecular dye) into the oxide film is enough to turn this insulating metal oxide (under dark) to a conductive state.[41,46] The material of choice has been commonly TiO_2 (anatase, rutile or a combination of both) (Figure 1.9), though other oxides as SnO_2, Nb_2O_5 and ZnO have been widely investigated as well.[41,42,46,47] One of the key aspects for all of these oxides is the nanocrystalline film morphology; namely, mesoporous structure that provides large area to volume ratio. This feature is highly important to harvest efficiently the incoming sunlight by providing a large surface area for loading of the molecular dye (i.e. a 10 µm thick TiO_2 film provides a surface area 1000 times larger that that of a compact TiO_2 layer).[46] This architecture allows DSSCs to reach high photocurrents owing to the enhanced optical density associated with larger dye loading. This feature, is to a large extent determined by the average particle size of the oxide (commonly around ten's of nanometers). Smaller particle size of the oxide provides higher dye loading; and hence, affects charge transport as the number of grain boundaries that an electron needs to pass is increased. Overall, the thickness of the metal oxide needs to be

adapted according to the diffusion length of electrons in the oxide. For TiO_2, the optimum performance of DSSC is obtained for the mesoporous oxide matrices with ~10 μm thicknesses and average particle size of ~10-20 nm (Figure 1.9).

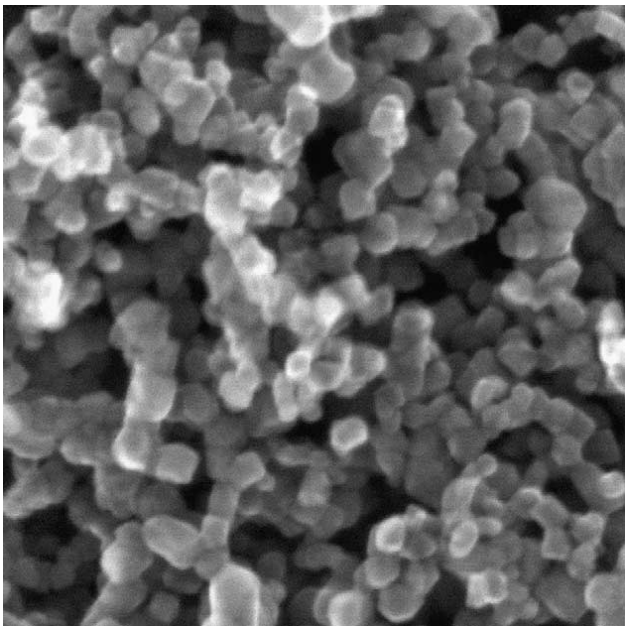

Figure 1.9 SEM image of mesoporous TiO_2 (anatase) (ref [42]).

1.4.3 Photo-induced interfacial electron transfer (ET) at dye oxide interfaces

Photo-induced interfacial electron transfer (ET) from molecular dyes to the mesoporous metal oxides is one of the most important steps in the operation of DSSCs (Figure 1.7-process, ii). ET is the first kinetic process for an efficient exciton dissociation. To achieve an efficient ET, one should consider the kinetic competition between ET and recombination channels, e.g radiative relaxation. This ET process will determine ultimately the quantum efficiency of the charge photogeneration and extraction processes in DSSCs.[45]

Dye sensitized mesoporous oxide system can be described as a donor-acceptor system. Here, the dye acts as the electron donor while the semiconductor oxide acts as the electron acceptor. Marcus Theory is the commonly accepted theoretical framework to describe ET reactions between donor and acceptor systems.[48] Within this picture, the ET process depends on the interfacial energetics (ΔG); where ΔG refers to the energy difference

between the LUMO of dye (donor) and the CB of the oxide (acceptor). ΔG acts as an ET driving force; therefore the larger ΔG the faster the ET rate will be within the Marcus normal region.[48] A second very important factor affecting the ET processes according to Marcus Theory is the electronic coupling (H_{AB}) between the LUMO orbitals of dye (A) and the acceptor states of the oxide (B); this is linked to the spatial overlap of donor and acceptor wavefunctions. Ultrafast ET is generally linked to the strong coupling between the dye LUMO and the oxide CB, which may be a function of the density of states (DOS) in the oxide.[45] Another factor affecting ET dynamics is the so-called reorganization energy (λ), which is the energy required to reorganize the structure of the system from its initial to final states without making the ET process. Reorganizational energy refers primarily to the contributions from solvation and vibrations assisting the ET process; these factors are expected to be Temperature dependent (non-adiabatic ET).

Although photo-induced interfacial ET at the dye/oxide interface has been extensively studied in various dye sensitized oxide systems over the last decades,[49–52] most of the current knowledge is rather qualitative. Further fundamental understanding of ET processes is needed to improve current DSSCs performances (~11 % for devices based on Ru dyes) and for establishing clearer structure-kinetics correlations. Also, achieveing long term stability of dye-oxide electrodes[36,53–55] represents one of the main challenges in this field. In Chapter 4 of this thesis, we analyse in detail photo-induced ET dynamics and their evolution upon dye degradation in dye sensitized mesoporous oxides by using TRTS.

1.5 Photocatalytic hydrogen generation

Solar energy can be converted into chemical energy and stored in fuels, such as the hydrogen generation process via photocatalytic water splitting or the photocatalytic generation of hydrocarbon based compounds via CO_2 reduction process.[5] Fujishima and Honda discovered photocatalytic water splitting in 1972.[56] Later, their group also discovered the photocatalytic CO_2 reduction in 1979.[57] Those two pioneering discoveries opened a new path of research for coverting solar energy into fuel. Since 1972, many types of materials, such as metal oxides, metal chalcogenides, metal nitrides, carbon nitrides, III–V and II-VI semiconductors[5,58,59] have been developed for photocatalytic water splitting. Fundamental

understanding of physico-chemical processes in these photocatalysts, including light absorption, charge separation, charge migration, charge recombination and surface redox reactions have received great attention for further development of photocatalysts and photocatalytic applications.[5,58,60]

In this thesis, we study hybrid, metal decorated CdSe tetrapods. These materials are used in an architecture which is suited for photogeneration and collection of charges at the semiconductor nanocrystal / metal interface followed by a charge migration towards metal / water interface. As shown in Figure 1.10, (i) a semiconductor nanocrystal absorbs sunlight energy that generates electron-hole pair, (ii) the metal which is used as co-catalyst captures the photogenerated electron from the semiconductor (the CB of semiconductor should be higher than the work-function of the metal (ΔG) in order to make electron capture possible). (iii) The captured electron catalyzes the redox reaction at metal / water interface to generate H_2 (see footnote[7] for water splitting) (The metal work-function should be higher than water redox potential ($\Delta G'$) in order to initiate the redox reaction before recombination with the hole residing in the semiconductor takes place, see footnote [8]) while (iv) photogenerated hole is removed from the semiconductor via hole acceptor.

[7] Overall reaction: $H_20 \rightarrow H_2 + 1/2\ O_2$

[8] Redox half cell reactions: $2H_2O\ (l) \rightarrow O_2\ (g) + 4H^+\ (aq) + 4e^-$, E_{red}^o =1.23 V (vs. NHE)

$4H^+\ (aq) + 4e^- \rightarrow 2H_2\ (g)$, E_{red}^o =0 V (vs. NHE)

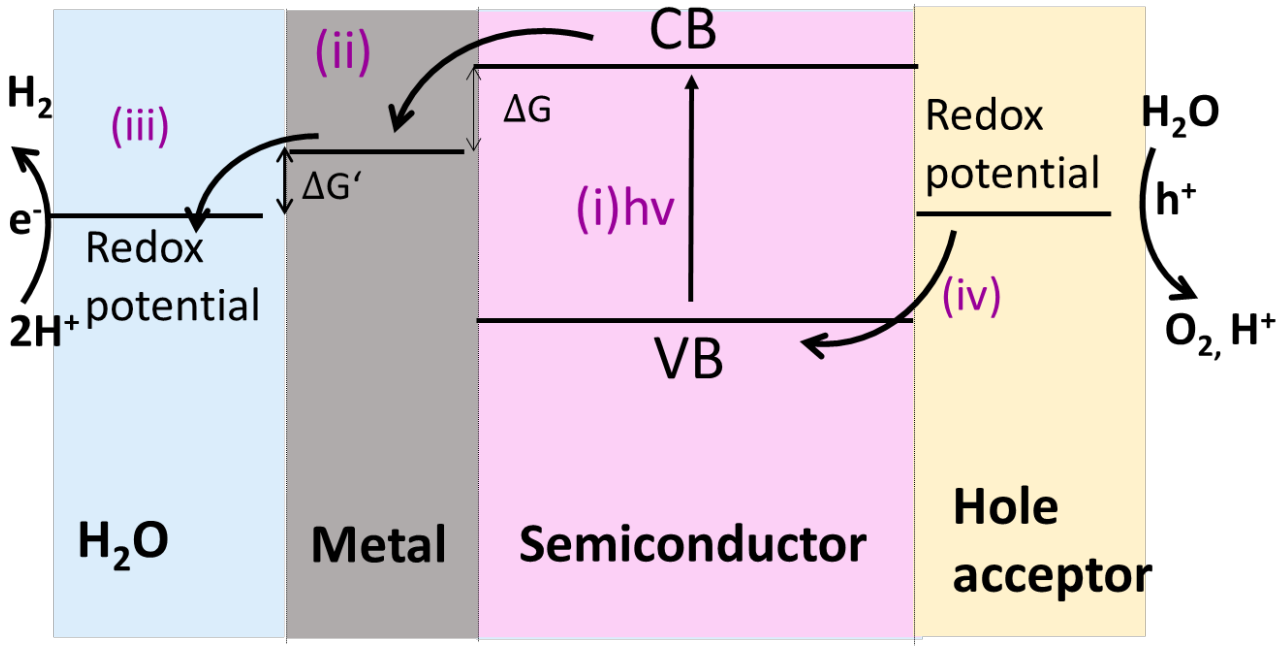

Figure 1.10 Schematic illustration of photocatalytic H_2 generation using metal decorated semiconductor: (i) Photoexcitation of the semiconductor from valence band (VB) to conduction band (CB) is followed by (ii) electron capture from semiconductor to the metal (ΔG is the difference of the energy between semiconductor CB and metal work-function). (iii) The captured electron at the metal is released to H_2O at the water/metal interface ($\Delta G'$ is the difference of the energy between metal work-function and redox potential of H_2O), while (iv) hole acceptor removes the photogenerated hole from the semiconductor at semiconductor/hole acceptor interfaces.

1.5.2 Metal decorated CdSe tetrapods for photocatalytic H_2 generation

CdX (X= Se, S, Te) semiconductors are used as photocatalysts for H_2 generation due to their tunable optical and electronic properties achieved by tuning their size, composition and morphology.[61–66] The ideal photocatalyst for water splitting is required to absorb a wide spectral range of sunlight because the band gap (Eg) of semiconductors determines the theoretical maximum solar-to-hydrogen (STH) efficiency.[4,5] Therefore, semiconductor should have an optimum Eg to achieve a high STH efficiency (see Figure 1.4). This can be achieved by tuning the size of CdX nanostructure. Another requirement for an ideal photocatalyst that can be achieved by CdX semiconductors is to separate the electron and hole within the

material. Using tetrapod morphology is one way of tuning wavefunction (electron and hole localization) in these nanostructures which directly affects the photo-induced charge carrier dynamics; and hence the photocatalytic H_2 generation.[64,67,68] Moreover, photocatalytic H_2 generation activity of these nanostructures can be improved by decorating them with metal nanoparticles that are used as co-catalysts.[5,63,64,69] Here, co-catalyst captures electrons from the semiconductor and co-catalyze the photocatalytic process by reducing the activation energy of the redox reaction at water / semiconductor interface (Figure 1.10). Therefore, controlling the size, composition, coverage and specific location of the metal co-catalysts is an important factor for improving photocatalytic H_2 generation efficiency.[62,70–75]

In Chapter 5 of this thesis, we study charge carrier dynamics in metal decorated CdSe tetrapods (Figure 1.11) (used for photocatalytic H_2 generation by our collaborators[70]) by using time-resolved terahertz spectroscopy (TRTS) to correlate their carrier dynamics and their photocatalytic H_2 generation activities.

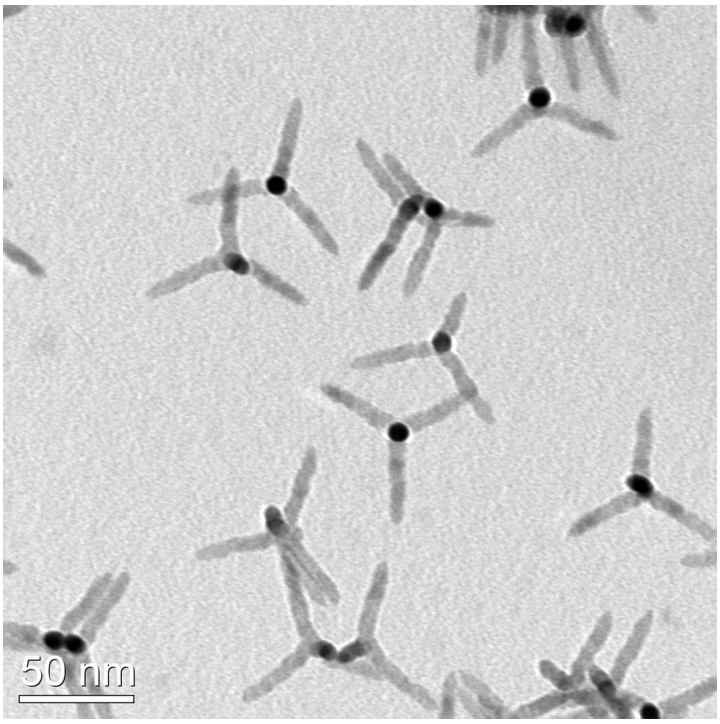

Figure 1.11 TEM images of CdSe tetrapods (adapted from ref [70]).

Chapter 2

Experimental technique, materials and sample preparations

In this chapter, we discuss the main experimental technique employed in this thesis, namely, time-resolved terahertz spectroscopy (TRTS). We introduce briefly the fundamentals of the generation and detection of THz pulses, the experimental set up, measurements of carrier dynamics by TRTS in a pump-probe scheme, including the data interpretation and common conductivity models. Furthermore, we describe the main aspects regarding sample preparation (e.g. preparation of methlyammonium lead iodide ($MAPbI_3$) perovskite films, metal oxide films, dye sensitized metal oxide films and Pt decorated CdSe tetrapods).

2.1 Time-resolved terahertz spectroscopy (TRTS)

The Terahertz (THz) frequency range lies between the far-infrared and the microwave regions in the electromagnetic spectrum as shown in Figure 2.1. As the typical timescales for randomization of carrier momentum via carrier-phonon interaction is ~picosecond (ps) (= 10^{-12} s)[76] and 1 THz is 10^{12} s^{-1}, the THz frequency range is ideal for studying these carrier dynamics. Furthermore, THz radiation can interact with excitons, phonons and vibrations in materials. Each of these quasi-particles has a specific fingerprint in the complex THz conductivity, which allows identifying the nature of the probed particles and quasi-particles.

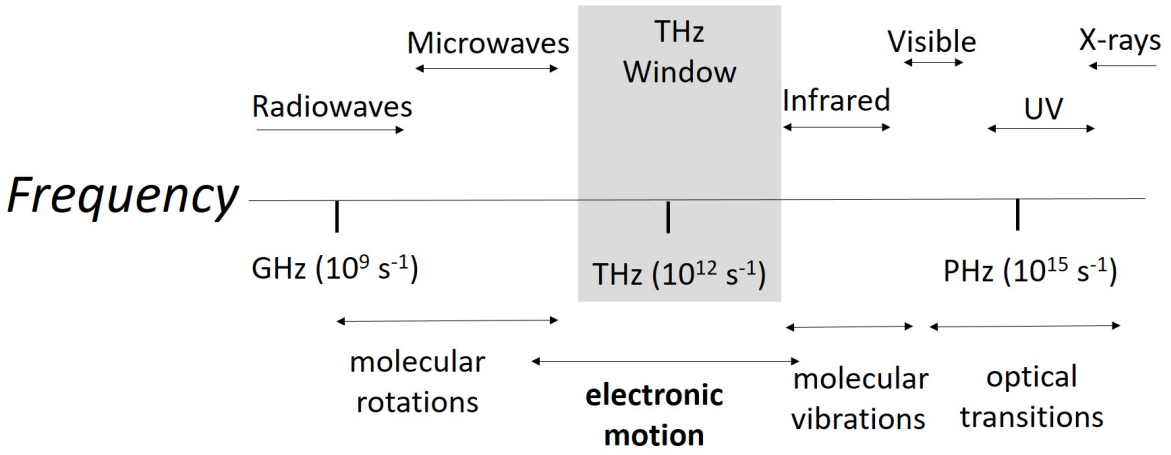

Figure 2.1 Electromagnetic spectrum from radio waves to X-ray (Adapted from ref[77]).

TRTS employs a freely propagating THz pulses to probe charge carriers. These probe pulses can be considered as wavepackets comprising frequencies in the range of 0.2-2.0 THz (for a ZnTe generation scheme) centered at 1 THz. The probe is strongly absorbed by the mobile charges and hence the THz absorbance provides the conductivity of the probed charges. As the field of the THz pulses can be recorded in the time domain with sub-picosecond time resolution (see the discussion of the detection) and the THz pulses are usually ~1 ps long, the dynamics of the complex THz photoconductivity of a photoexcited material can be measured with sub-ps time resolution.[76] As TRTS is a contactless technique, it is particularly suited to study photoconductivity at the nanoscale, where establishing metal contacts, apart from highly perturbative, is often not feasible.

2.1.1 Experimental setup

The layout of the TRTS set up employed in this thesis is shown in Figure 2.2. The system is based on an amplified Ti:sapphire laser system delivering pulses with 1 mJ pulse energy, 800 nm central wavelength and temporal length 100 fs (at 1 kHz repetition rate). The output pulse of the laser is split into three beams, refered to as the pump, the THz generation and the THz sampling beam, respectively.

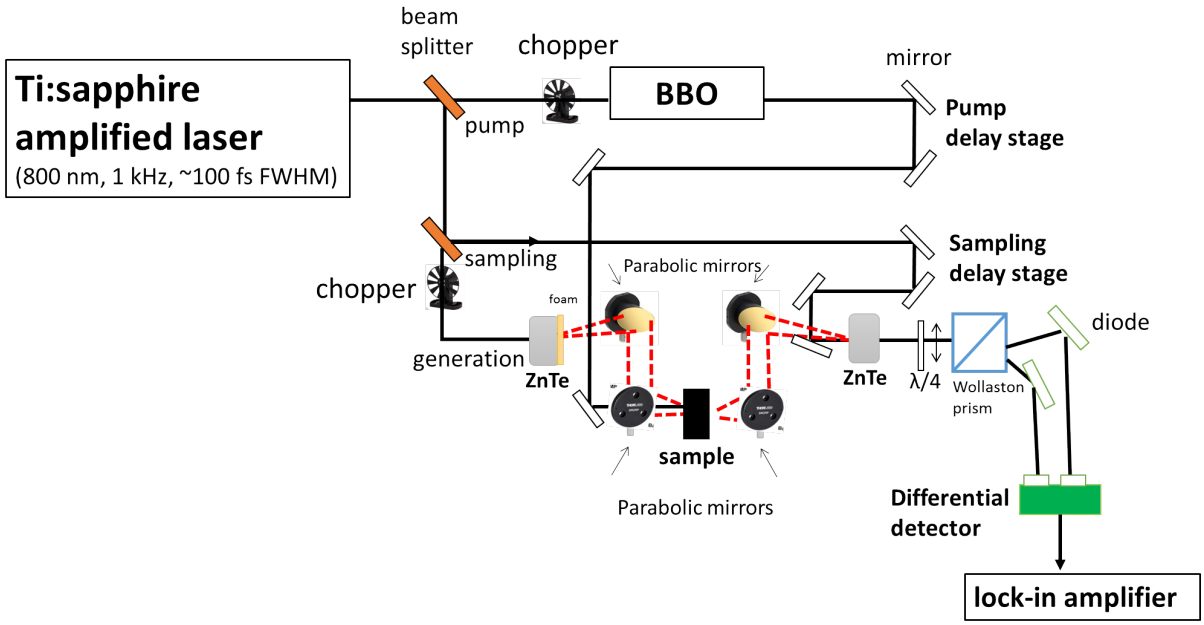

Figure 2.2 Layout of a time-resolved terahertz spectroscopy (TRTS) set up.

The 800 nm pump beam (normally 90 % of 1 W) is employed in order to photoexcite the sample investigated. The wavelength of the pump beam can be converted to 400 nm using second harmonic generation in a beta barium borate (BBO) crystal. The pump beam timing relative to the THz probe can be adjusted by a mechanical delay line, which allows us to vary the arrival time of the pump pulses to the sample (see Figure 2.2). To achieve homogeneous pumping, we ensure that the diameter of pump beam (> 3 mm) is larger than that of the THz beam (< 300 μm) at the focus of the sample.

The generation beam is employed to generate THz probe waveform by optical rectification (OR) in a 1 mm thick ZnTe crystal.[78] This process is a three-wave mixing process where the different spectral components of the generation beam interact with each other, generating a new electromagnetic wave with a frequency equal to the difference of the interacting components. The frequency of the generated electromagnetic wave falls into the THz range of 0.2-2.0 THz because the bandwidth is limited by phonons in ZnTe crystal. The temporal length of the generated pulses is ~1 ps. Using parabolic mirrors, the generated THz beam is collimated, then focused on the sample. The THz beam transmitted through the sample guided by other two parabolic mirrors onto the detector space. Here, the THz beam

propagates between the emitting ZnTe crystal and the detector which is kept under N_2 environment to prevent absorption of the THz radiation by the water vapor in the air.[79]

The sampling beam (800 nm) provides gated detection of the THz pulses in a 1 mm think (110)-oriented ZnTe crystal via the electro-optic (EO) Pockels effect.[80] The sampling beam is spatially overlapped with the focused THz probe beam at the position of the detection ZnTe crystal. The electric field of the THz pulse induces an anisotropic change in the refractive index of the detection ZnTe crystal (birefringence). This effect then changes the polarization of the sampling beam. The extent of this change depends on the strength of the electric field at the instant when the sampling pulse propagates through the detection ZnTe crystal.[76] The polarization change in the sampling beam through detection crystal is measured by splitting the beam into its vertical and horizontal components using a Wollaston prism and detecting the difference in the intensity of both components by differential photodiodes. The polarization of the sampling beam is tuned in such a way that the signal on the differential photodiodes is propotional to the electric field of the THz pulse.[81] By changing the arrival time of the sampling beam in detection crystal relative to the THz pulse, the THz pulse can be mapped out in the time domain (Figure 2.2).[81]

To increase the signal-to-noise ratio, the signal is collected using a lock-in amplifier, operating at a frequency of 500 Hz which is the half of the repetition rate of the laser (1 kHz). In this detection scheme, we place a mechanical chopper synchronized with the lock-in amplifier operating at 500 Hz either into the generation beam, thus detecting the field of the THz pulses E(t) transmitted through our sample, or into the pump beam, detecting the change in the transmitted THz field ΔE(t) caused by the photoexcitation of the sample. Using Fourier transformation (FFT), the time domain data can be analysed in the frequency domain allowing us to retrieve the complex valued response function of the sample,[82] as the complex refractive index (n(ω)), complex permittivity (ε(ω)) and/or complex conductivity (σ(ω)) (Equation 2.1). These are equivalent ways to describe the response function of a material. The relation between them is described by the equation:

$$\hat{\sigma} = -i\hat{\varepsilon}\varepsilon_0\omega = -i\hat{n}^2\varepsilon_0\omega \quad (2.1)$$

where ε_0 and ω are vacuum permittivity and angular frequency of oscillating THz probe ($\omega = 2\pi v$, where v is frequency). In this thesis, we primarily focus on the frequency resolved

data obtained with THz probe in terms of complex conductivity $\sigma(\omega)$ to discuss the nature of the conductivity in hybrid photoactive materials. By applying FFT of the THz field in the time domain ($E(t)$), we can obtain the THz profile in the frequency domain $E(\omega)$.

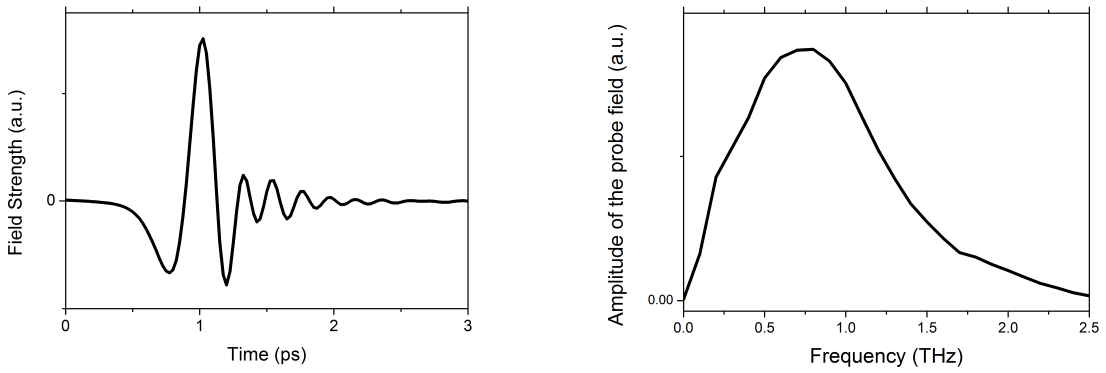

Figure 2.2 Typical waveform of THz probe in time domain (left) and the spectral amplitude of the THz waveform obtained using Fourier transformation (FFT) (right).

2.1.2 Data analysis in TRTS experiments

In this section, we explain experiment details and protocols to obtain the frequency resolved complex conductivity of a given material to monitor carrier dynamics.

To investigate frequency resolved complex conductivity in a sample, we first record in the time domain the transmission of THz field through unexcited sample as a reference (Figure 2.4 - Top). Then, we photoexcite the sample with pump beam and consequitively we probe the photoinduced change in THz field ($\Delta E(t) = E_{exc}(t) - E_{unexc}(t)$, in Figure 2.4) by fixing the delay between pump and sampling pulse while changing the sampling delay stage (Figure 2.4 - Bottom). By FFT, we calculate frequency resolved waveforms of $E_{unexc}(\omega)$ and $\Delta E(\omega)$. We extract complex conductivity from THz waveforms of $E_{unexc}(\omega)$ and $\Delta E(\omega)$ which propagate through a medium. For thin samples with photoexcited region, L in micrometers or less, which is observed in semiconductors with strong optical absorption or in very thin films, the photo-induced complex conductivity can be calculated according to the following equation:[83]

$$\Delta\sigma(\omega) = -\frac{n+1}{Z_0 L}\frac{\Delta T(\omega)}{T_0(\omega)} \quad (2.3)$$

where Z_0 = 377 Ω is the impedance of free space, L is the thickness of the photoexcited region and n is the refractive index of the medium after photoexcited region (substrate, cuvette or unexcited region of the same material). The SI unit of the extracted photoconductivity is S/m.

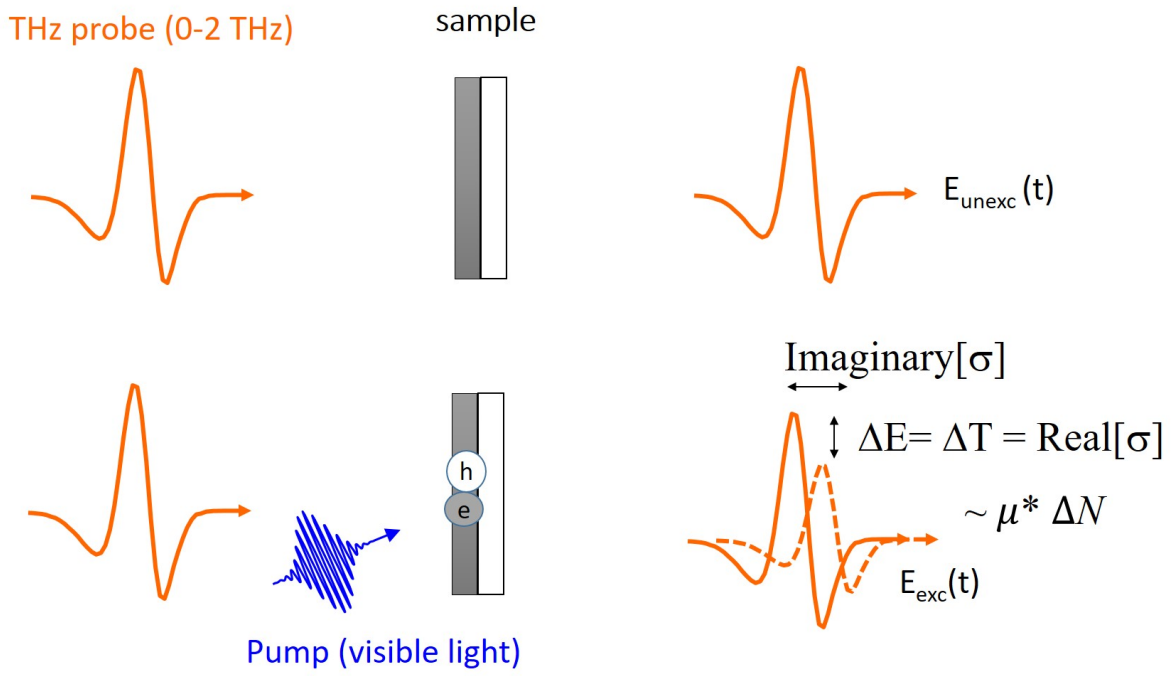

Figure 2.4 A typical TRTS experiment. Top: Measurement of THz probe through the unexcited sample, $E_{unexc}(t)$ as a reference experiment where the optical chopper is placed in front of the generation beam. Here, the differential signal of the probe field with and without the sample is measured. Bottom: Measurement of THz probe through the excited sample $E_{exc}(t)$ via pump where the chopper is placed in front of the pump beam. Here, the differential signal of the probe field with and without the pump is measured.

To monitor carrier dynamics in samples studied in this thesis, we record pump induced changes at the peak of the THz probe pulse transmitted through the sample by varying the time delay between the pump and probe/sampling pulses. The recorded field ΔE can be then interpreted as the time-dependent, frequency-averaged real photoconductivity Re[σ] (t) of the photogenerated carrier (Figure 2.4). It contains both the response of electrons and holes as follows:

$$\text{Re}[\sigma]\,(t) \propto N_e(t) * \mu_e + N_h(t) * \mu_h \quad (2.4)$$

Where $N_e(t)$ and $N_h(t)$ are carrier density for electrons and holes at a given time delay, μ_e and μ_h are mobility of electrons and holes in the sample, respectively. It is possible to conduct pump-probe TRTS measurements to investigate the rates of charge generation, recombination, trapping and exciton condensation in intrinsic semiconductors like the perovskite presented in Chapter 3[76,84,85] and confined nanostructured semiconductors like the tetrapod presented in Chapter 5. Also, these measurements have been conducted to study the electron transfer (ET) dynamics at the surfaces of bulk materials, such as dyes[86,87] or quantum dots (QDs)[88,89] sensitized mesoporous oxides as in the case of dye sensitized mesoporous oxides studies presented in Chapter 4. TRTS measurements for monitoring ET in sensitized architectures probe directly the carrier population in the mesoporous oxides. This is because the carriers are totally confined in the sensitizer (dye molecule or QD) and their THz conductivity is zero (zero Re[σ]). Hence, the amplitude change of the peak of THz field (ΔE) can be directly related to the number of free carriers times mobility in the oxide (Equation 2.4). As the mobility of holes photogenerated in the sensitizer (located at the HOMO of the sensitizer) is very small compared to the mobility of electrons injected to the oxide, the TRTS technique is only sensitive to free electrons in the CB of the oxide. Therefore, the carrier densitiy and mobility of holes are assumed to be zero in the Equation 2.4, and the equation becomes as:

$$\text{Re}[\sigma]\,(t) \propto N_e(t) * \mu_e \quad (2.5)$$

2.2 Conductivity models

2.2.1 The Drude Model

The interaction of THz radiation with free carriers in bulk materials can be described by the Drude model. This is a model for describing the transport of charges where the electrons and holes are not interacting with each other, behaving like an ideal classical gas. In the Drude model, it is assumed that the transport is determined only through momentum randomizing scattering events with an averaged scattering time τ_s.

In the absence of an electric field, charge carriers in a 3 dimensional system move with a thermal velocity of $v_t = \sqrt{3k_BT/m^*}$, where k_B, T and m^* are the Boltzmann constant, temperature and effective mass of the specific carrier (electron or hole), respectively. The value of the charge carriers' mean velocity in the absence of electric field is zero as the direction of the velocity of the carrier after collision is considered random. On the other hand, in the presence of a time dependent electric field E(t), carriers gain a mean drift velocity v_d.

Charge carriers can be scattered by phonons or defects in the lattice; the distance that a carrier travels on average between two scattering events is the mean free path. As a result of these collisions, carrier motion is damped by a frictional force with a characteristic time of τ_s between collisions. In the presence of a time dependent applied field E(t), the motion is described by the first order differential equation:

$$\frac{d}{dt}v_d(t) + \frac{1}{\tau_s}v_d(t) = -\frac{e}{m^*}E(t) \qquad (2.6)$$

where e is the elementary charge of an electron. For a sinusoidal electric field with an angular frequency ω, $E(t) = E_0e^{-i\omega t}$, the solution for the differential equation 2.6 reveals:

$$v_d(t) = -\frac{e\tau_s}{m^*}\frac{1}{1-i\omega\tau_s}E_0e^{-i\omega t} \qquad (2.7)$$

Because the drift velocity is dependent on the applied driving field, the model explains how the ac mobility looks like in semiconductors. Here the mobility, μ, can be written using the proportionality factor between E and v_d:

$$\mu(\omega) = \frac{v_d(t)}{E(t)} = \frac{e\tau_s}{m^*}\frac{1}{1-i\omega\tau_s} \qquad (2.8)$$

As μ defines how easily a carrier moves in a material, carriers are relatively immobile and are not easily perturbed by an applied field if the time between collisions is small. This property is often defined with the DC (direct current) mobility measured at frequency $\omega \to 0$.

The conductivity of a material is then described by the average mobility and the density of charge carriers (N) as:

$$\sigma(\omega) = Ne\mu(\omega) = \frac{Ne^2\tau_s}{m^*}\frac{1}{1-i\omega\tau_s}, \qquad (2.9)$$

$$\sigma(\omega) = \frac{\varepsilon_0 \tau_s \omega_p^2}{1 - i\omega\tau_s} \ , \ \omega_p^2 = \frac{e^2 N}{\varepsilon_0 m^*} \qquad (2.10)$$

where ω_p and ε_0 are plasma frequency and vacuum permittivity, respectively. Figure 2.4 shows the complex conductivity described by the Drude model.

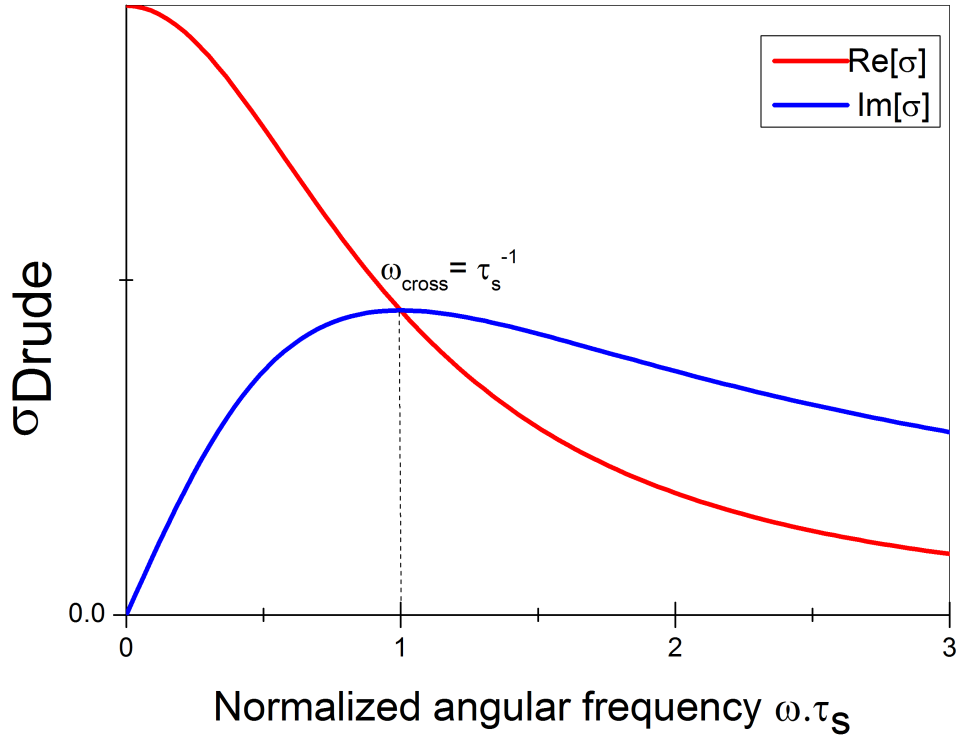

Figure 2.4. Drude conductivity versus angular frequency (ω) times scattering time (τ_s). The angular frequency where real and imaginary components cross is related to the scattering time, $\tau_s = {\omega_{cross}}^{-1}$.

Charge carriers in typical semiconductor materials can be scattered by ionized impurities, phonons, neutral defects, surfaces and interfaces and other carriers (scattering between electron and hole).[90] In general, more than one of these sources can present in semiconductors and influence the scattering mechanisms that can be combined using Matthiessen's rule as follows:

$$\frac{1}{\tau_s} = \frac{1}{\tau_{impurities}} + \frac{1}{\tau_{defects}} + \frac{1}{\tau_{phonon}} + \cdots \qquad (2.10)$$

or can be rewritten in terms of the mobility;

$$\frac{1}{\mu} = \frac{1}{\mu_{impurities}} + \frac{1}{\mu_{defects}} + \frac{1}{\mu_{phonon}} + \cdots \qquad (2.11)$$

where $\tau_{impurities}, \tau_{defects,}\ \tau_{phonon}$ are scattering times correspond to impurity scattering, defect scattering and phonon scattering. This equation can be used if these scattering mechanisms are independent of each other.[91] The dominating scattering mechanism in a material can be determined by measuring the temperature dependent mobility of the given material, as the different scattering mechanisms usually have distinct temperature. The temperature dependence of scattering times can be inferred from temperature dependent TRTS measurements (see Figure 2.4). In Chapter 3, we will explain our study using temperature dependent TRTS measurements.

2.2.2 The Drude-Smith Model

The Drude-Smith Model is a modified version of the Drude Model where the assumption of isotropic carrier scattering is no longer valid. This can be valid for materials with large surface to bulk ratio, where carriers can scatter at boundaries of the crystals. The conductivity is then described by the following equation:

$$\sigma(\omega) = \frac{\varepsilon_0 \tau_s \omega_p^2}{1 - i\omega\tau_s} * \left(1 + \frac{c}{1 - i\omega\tau_s}\right) \qquad (2.12)$$

where the additional parameter c (can be between 0 and -1) refers to the backscattering parameter of the scattering event. Figure 2.5 shows the complex conductivity described by the Drude-Smith model with various backscattering parameters. Here, $c = -1$ describes complete backscattering. For $c = 0$, the model reduces to the classical Drude model describing fully momentum randomizing scattering. As can be seen in Figure 2.5, the sign of Re[σ] is positive, while that of Im[σ] changes from positive towards negative as c parameter approaches to -1. This negative sign of Im[σ] can originate from the presence of confiment within the carriers as THz photons can polarize the confined carriers via non-resonant interactions, while positive Im[σ] mainly refers to free charges without confinement effect.

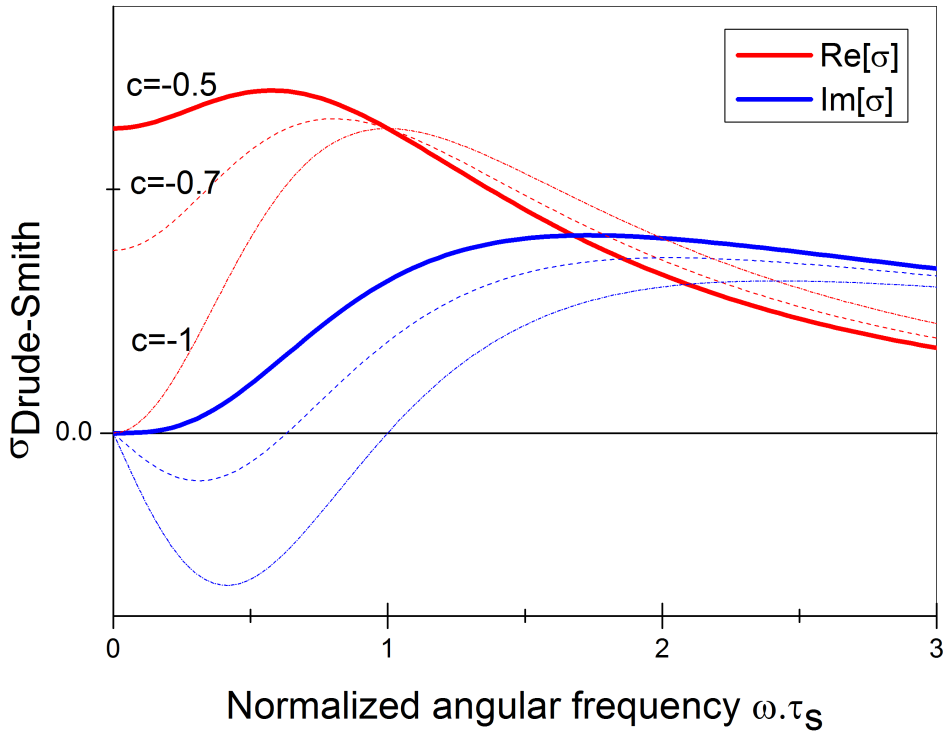

Figure 2.5 Drude-Smith conductivity versus angular frequency (ω) times scattering time (τ_s) for various c parameters of -0.5, -0.7 and -1. The c=-1 refers complete backscattering where the σ_{DC}=0 and negative imaginary conductivity Im[σ]. This behavior is equal to Lorentz oscillator model.

2.2.3 The Lorentz Oscillator Model

The Lorentz Oscillator model describes the conductivity of completely localized charge carriers or excitons due to a confined environment or a strong electron-hole Coulomb attraction.[76] The conductivity described by the Lorentz Oscillator model is obtained by adding a restoring force term to the Equation 2.10 resulting in the equation:

$$\sigma(\omega) = \frac{\varepsilon_0 \tau_s \omega_p^2}{1 - i\omega\tau_s + i\tau_s\omega_0^2/\omega} \qquad (2.13)$$

where ω_0 is the angular frequency of the oscillatory response. Then, the resonance frequency is $\nu_0 = \omega_0 / 2\pi$. Therefore, the Drude Equation 2.10 refers to a Lorentzian oscillator centered at ω_0 = 0. The conductivity predicted by the Lorentz oscillator model is

shown at low THz energies (Figure 2.6). As seen in the figure, the Lorentz oscillator model represents a zero Re[σ] because the energy of THz photons is typically much lower than the interband transitions of excitons in confined semiconductors. Hence, THz field at the same low frequency is not able to produce transitions within the absorber. And, a negative Im[σ] is observed due to the fact that THz photons can polarize the excitons or confined carriers via non-resonant interactions.

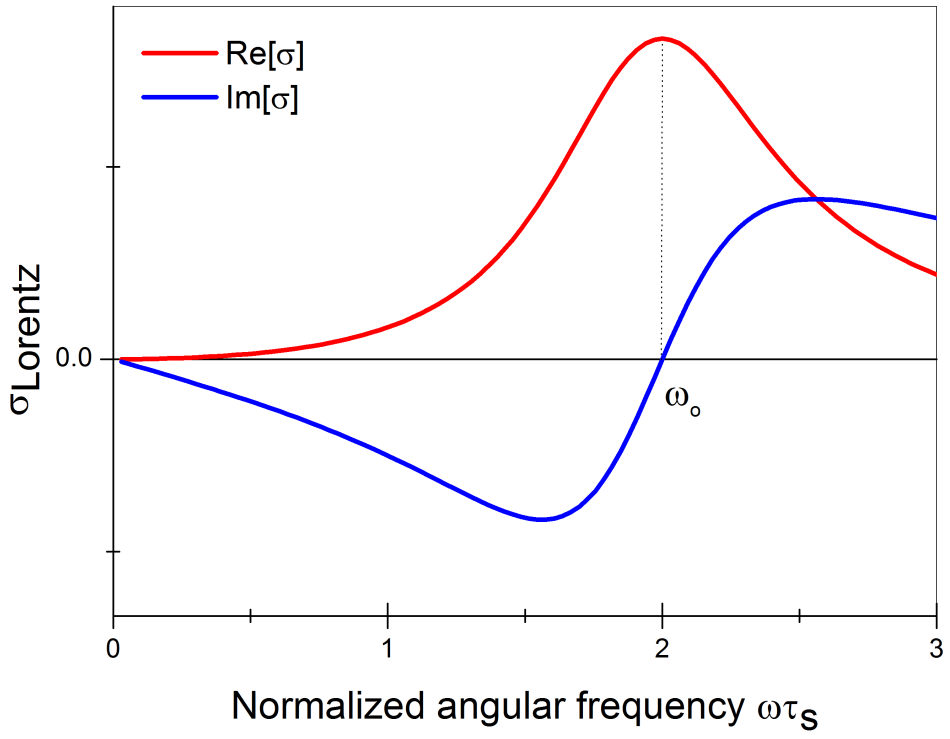

Figure 2.6 Lorentz-oscillator conductivity versus angular frequency (ω) times scattering time (τ_s). The resonance frequency ω_0 for excitonic transitions is typically much higher than the THz probe frequencies.

2.3 Materials and sample preparations

2.3.1 Preparation of $MAPbI_3(Cl)$ perovskite films

We follow standard procedures described in previous works as:[9,92] 27.86 ml methylamine (40 wt. % in methanol) was stirred with 30 mL hydrogen iodide (HI) (57 % in water) at 0 ^{o}C

for 2 hours under nitrogen to obtain methylammonium iodide (MAI). The precipitate was obtained by a rotary evaporator at 50 ^{o}C, and then recrystallized by ethanol and diethylether. The crystals were recovered by suction filtration, and dried at 60 ^{o}C in a vacuum oven for 24 hours.[92] The crystals were stored in a nitrogen glove box in a dark environment. Then, $MAPbI_3(Cl)$ perovskite layers were prepared from a % 40 wt solution of MAI and $PbCl_2$ in 3:1 molar ratio in anhydrous N,N-Dimethylformamide (DMF) deposited on the substrates and spin coating at 2000 rpm in a nitrogen filled glove box.[93] After spin-coating, the films were left to dry at room temperature for 30 minutes, then annealed for 45 min on a 100 ^{o}C hotplate in the glove box.

2.3.2 Preparation of TiO_2 mesoporous oxide films

TiO_2 paste is used as purchased from Solaronix (Ti-Nanooxide T). The corresponding oxide films are prepared by the doctor blading technique on fused silica substates (LG Optical Ltd.) The films were dried at 150 °C for 1 hour and sintered at 450 °C for 2 hours in an oven.

2.3.3 Preparation of sensitized mesoporous oxide films

We use dip coating technique to prepare sensitized mesoporous oxide films from $5.0*10^{-4}$M solutions of Ru(4,4'-dicarboxylic acid-2,2'-bipyridine)$_2$(NCS)$_2$ (N3 dye) (Solaronix), 4,4'-dicarboxy-2,2'-bipyridine (dcbpy) (Sigma Aldrich) in ethanol (≥ 99.5 Sigma Aldrich).

2.3.4 Tetrapods

Materials are synthesized by Sung et al in The National Creative Research Initiative Center for Intelligent Hybrids, National University, Seoul, Republic of Korea and are used as received.[70]

Chapter 3

Phonon-Electron Scattering Limits Free Charge Mobility in Methylammonium Lead Iodide Perovskites

In the following chapter, the nature of the photoconductivity in solution-processed films of methylammonium lead iodide perovskite is investigated by using TRTS (Figure 3.1) and determining the variation of the photoconductive response with temperature. Ultra-broadband Terahertz (THz) photoconductivity spectra in the 0.3-10 THz range can be reproduced well by a simple Drude-like response at room temperature, where free charge carrier motion is characterized by an average scattering time. The scattering time determined from Drude fits in the 0.3−2 THz region increases from ~4 fs at 300 K (tetragonal phase; mobility of ~27 $cm^2 V^{-1} s^{-1}$) to almost ~25 fs at 77 K (orthorhombic phase, mobility of ~150 $cm^2 V^{-1} s^{-1}$). For the tetragonal phase (temperature range 150 < T <300 K) the scattering time shows a $\sim T^{-3/2}$ dependence, approaching the theoretical limit for pure acoustic phonon (deformation potential) scattering. Hence, electron-phonon, rather than impurity scattering, sets the upper limit on free charge transport for this perovskite (see footnote 9).

[9] *Adapted with permission from (J. Phys. Chem. Lett., 2015, 6, 4991-4996). Copyright (2015) American Chemical Society*

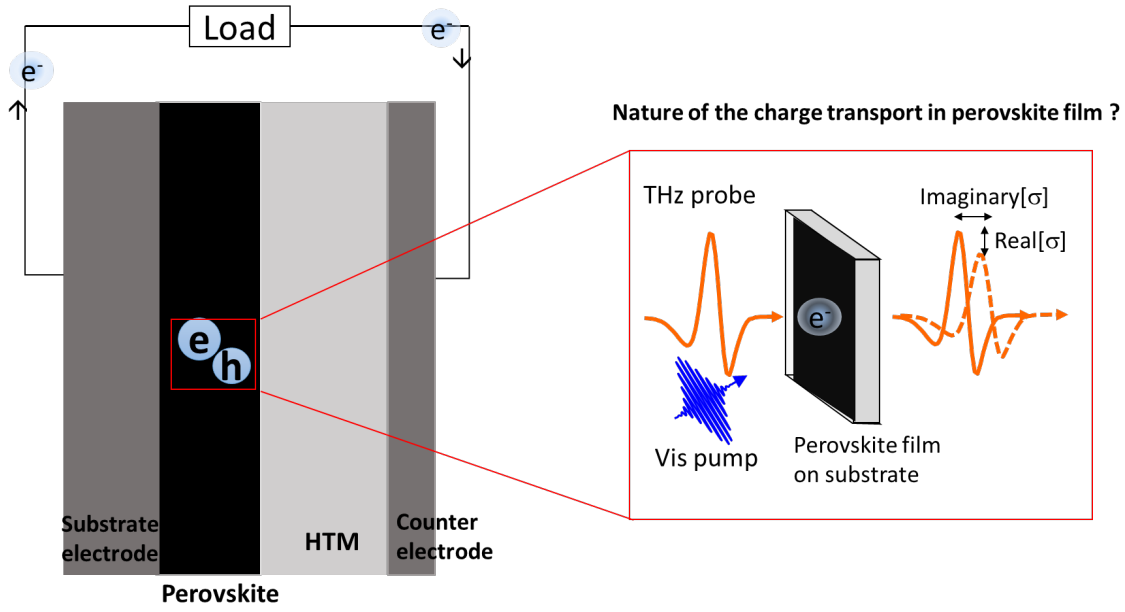

Figure 3.1 Schematic representation for TRTS experiment in perovskite films deposited on a flat substrate.

3.1 Introduction and aim of the work

Owing to their solution processability, tunable band gap, defect free nature and strong optical absorption, methylammonium lead halide perovskites have emerged as promising low-cost candidates for highly efficient active materials in optoelectronic devices such as solar cells.[9,18,22,23,92,93] A steep increase in perovskite-based solar cell efficiencies has been reported in recent years, however, several fundamental intrinsic key aspects in perovskite films remain controversial, such as the nature and relative yield of the relevant photogenerated products (excitons, free carriers or both)[14,25] and their transport properties.[22,23] Here, using ultra-broad band (0.3-10 THz) time resolved THz spectroscopy (TRTS),[76] we interrogate the nature of the photoconductivity in solution-processed methylammonium lead iodide perovskite films as a function of temperature. We find that photoexcitation of the tetragonal phase (T > 150 K), produces free charges exhibiting long-lived first-order recombination kinetics (for fluences < 30 μJ cm^{-2}) indicative of low impurity content. The frequency-resolved photoconductivity spectra can be described well by the Drude model, which provides temperature-dependent scattering times consistent with $MAPbI_3(Cl)$ mobilities solely limited by phonon (rather than impurity) scattering in the tetragonal perovskite phase; i.e. behavior characteristic of an intrinsic semiconductor. This

conclusion is derived from samples displaying mobilities which parallel those in state-of-the-art reports; on the other hand, our findings are discussed in the context of unintentional sample-to-sample variability within the set of analyzed samples and available literature.

3.2 Materials and Methods

We have introduced TRTS set up, experimental details of TRTS dynamics and frequency resolved complex conductivity measurements and how to extract complex conductivity in Chapter 2. Here, we also conducted complex conductivity analysis in high frequency THz window (0.3-10 THz) that will be explained briefly in Appendix 3.5. The low temperature measurements in TRTS and photoluminescence (PL) measurements were performed in a liquid nitrogen cooled cryostat under $p < 1.4x10^{-4}$ mbar vacuum conditions.

Preparation of $MAPbI_3(Cl)$ perovskite films has been explained in Chapter 2, Section 2.4.1. Depending on the employed characterization method, different substrates were employed: fused silica substrates for TRTS in the spectral range 0.3-2.0 THz, optical absorbance, photoluminescence (PL) and time-resolved photoluminescence (TRPL); high-resistivity silicon substrates for ultra-broadband TRTS in the range 2.5-12.0 THz; and silicon, glass and fused silica substrates for SEM and XRD characterization.

3.3 Results and Discussion

We first report TRTS carrier dynamics in our best performing sample, with inferred room temperature mobility of ~27±3 $cm^2 V^{-1} s^{-1}$, at temperatures ranging from 300 K to 77 K. At room temperature the real-valued photoconductivity at 10 ps pump probe delay was found to scale linearly with excitation fluence up to ~56 $\mu J\ cm^{-2}$ (see Figure 3.5-right). The transition from first to second order relaxation relaxation kinetics was found at < 30 $\mu J\ cm^{-2}$ (see Figure 3.5-left) in fair agreement with previous reports.[33,20,94] The onset of the second-order relaxation regime could have different origins, e.g. trap filling or time-dependent carrier concentration and/or mobility.[20,95] To stay well clear of this regime, the measurements reported here were performed for very low excitation fluences, at ~3 μJ cm-2, unless explicitly noted in the text. Figure 3.2a shows the time-dependent normalized real-

valued conductivity, averaged over the 0.3-2 THz probe window for different sample temperatures following excitation with 2.8 μJ cm^{-2} pump pulses (under vacuum conditions, < $1.4x10^{-4}$ mbar). The carrier recombination dynamics can be described by a first order recombination processes (see Figure 3.5 - left). Above ~150 K (tetragonal phase, black to light gray solid lines in Figure 3.2a)[96,97] the photoconductivity appears quasi-instantaneously upon excitation, i.e. faster than the ~200 fs time resolution of our spectrometer (see Figure 3.6), and it decays only slightly over the 1 ns time window, consistent with low defect concentration in these solution processed samples. By contrast, for temperatures below ~150 K, corresponding to orthorhombic crystal phase,[96,97] (dark red to orange dashed lines in Figure 3.2a) the photoconductivity decays faster (with an inferred exponential decay time of 1.35±0.02 ns). The appearance of this temperature-activated carrier decay channel correlates with the emergence of a broad defect related sub-bandgap photoluminescence peaking at ~860 nm (see Figure 3.2b). This emission has recently been reported and assigned to acceptor (hole) states.[98] Interestingly, at 77 K both tetragonal and orthorhombic phases clearly coexist, as evident from the presence of the 2 characteristic emission peaks at ~ 775 nm and ~750 nm, see orange dotted line in Figure 3.2b, in agreement with a previous report;[99] the persistence of both crystal phases at low temperature could reflect the existence of domains with different degree of ordering of methyl ammonium ions. This could translate to local perturbations of band edges (between or within single crystal domains) which could potentially assist exciton dissociation and electron-hole localization.[100]

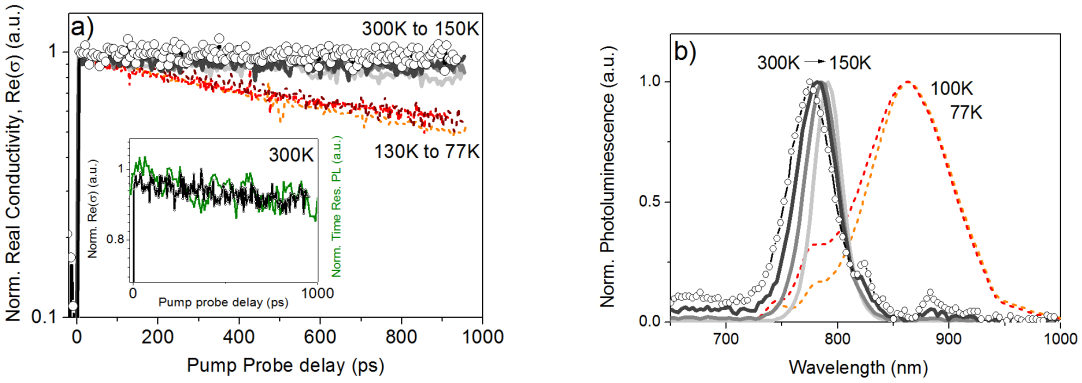

Figure 3.2 a) Normalized real-valued photoconductivity (log scale) as a function of pump-probe delay for $MAPbI_3(Cl)$ for temperatures >150 K (black-300K, dark gray-250 K, gray-200 K, LT gray-150 K) and <150 K (dark red-130K, red-100K, orange-77 K) with excitation wavelength 400 nm at a fluence of 2.8 μJ cm^{-2}. The inset shows the correlation between normalized real-valued photoconductivity (in black) and time resolved photoluminescence (in green) over 1 ns temporal window at room temperature. b) Normalized photoluminescence in the 300 – 77 K temperature ranges, excitation 400 nm, power ~1 mW. Measurements at 300 K are highlighted with open circles in both panels. The transition around 150 K in both conductivity and photoluminescence can be attributed to a transition from the high-temperature tetragonal phase to the low-temperature orthorhombic phase.

Time-resolved photoluminescence (TRPL) data in a temporal window of 1 μs (see Figure 3.7) reveal first-order decay dynamics for the ~775 nm emission with τ(300 K) = 129.1±0.7 ns. The first-order decay lifetime is within the range of values previously reported for $MAPbI_3$ and $MAPbI_3(Cl)$ samples (in the range 1-300 ns).[9,15,22,33,94,101,102] A TRPL decay trace measured under the same excitation conditions as for TRTS, is shown in the inset of in Figure 3.2a. The agreement between the TRPL and TRTS lifetimes for these samples leads to the conclusion that the carrier mobility remains constant over the probed time range[21], i.e. there are no signatures of dispersive transport within the analyzed time window.

Previous THz spectroscopy studies on perovskites have been primarily performed using ZnTe based generation and detection with a frequency window of 0.3-2.0 THz.[20,21,32,33] These studies have provided spectra without dispersion in the real and imaginary

components of the conductivity. Aiming to gain additional insights into the nature of the photoconductivity on our samples, we employed broadband THz spectroscopy in transmission mode in $MAPbI_3(Cl)$ perovskites over the wider frequency range (see Appendix). Figure 3.3a shows the characteristic room temperature photo-response under ambient conditions several picoseconds after photoexcitation, for samples deposited on fused silica (circles in the range 0.3-2 THz; excitation wavelength 400 nm, fluence 2.8 μJ cm^{-2}) and high resistivity silicon (squares in the range 6-10 THz, excitation wavelength 400 nm, fluence 48.6 μJ cm^{-2}) respectively. The high THz frequency data was scaled down to account for the higher excitation fluence (see Appendix). The selected frequency range 6-10 THz shown in Figure 3.3a is free of complications at low (silicon substrate contributing to the photoconductivity signal, causing significant Drude like contributions at frequencies below 6 THz) and high (phonons above 10 THz) frequencies (see Appendix, Figure 3.8 and Figure 3.9). The conductivity spectra in Figure 3.3a show, within the uncertainty of the measurement (e.g. samples deposited onto different substrates, see Appendix, Figure 3.10), an almost dispersion-less real conductivity, and essentially zero imaginary conductivity within the analyzed broadband THz window. These spectral signatures are indicative of conductivity mediated by free charges that undergo momentum-randomizing scattering events at a very high rate, well exceeding the maximum frequency of 10 THz.[76] If the monitored free carriers in these samples would experience a substantial restoring force and/or any degree of localization, one would expect both of these effects to manifest themselves in the THz frequency window as a dispersive real conductivity component and negative, potentially zero-crossing imaginary component as predicted by, e.g., the Drude-Smith model.[76,103–105] In absence of evidence for carrier localization over the broad spectral range, the Drude model appears, in first approximation, as the most suitable description given in Equation 2.9. A fit to the Drude model is shown as black solid lines in Figure 3.3a (note that fits to Drude-Smith provide Drude response as well, with a Drude−Smith parameter equaling 0); here ωp was fixed using N determined from the number of impinging photons (assuming a 100% quantum yield for electron and hole generation), and an electron-hole averaged effective mass of $m^* = 0.26\ m_0$.[31] Hence, the only free parameter in the Drude model is the momentum scattering time, τ_s, which determines both the shape and the amplitude of the conductivity. From the fit in Figure 3.3a we find τ_s = 4.0±0.5 fs. From this scattering time the mean free path (l)

between momentum randomizing scattering events can be estimated through the relation: l = v·τ_s = 0.8 nm (where v refers to the thermal velocity; v = $(3kBT/m^*)^{1/2}$ = 0.2 nm / fs with m* = 0.26 m_0, and τ_s= 4 fs), i.e. ~60 times smaller when compared with the typical room temperature values for GaAs (where l = 50 nm at τ_s = 100 fs and m* = 0.067 m_0). For the solution processed $MAPbI_3$(Cl) perovskite films analyzed here, the scattering time corresponds to a room temperature DC mobility of μ=27±3 $cm^2\ V^{-1}\ s^{-1}$ (with μ =e·τ_s/m*). These results are in quantitative agreement with those reported for vapor deposited $MAPbI_3$(Cl) thin films (m = 33 $cm^2\ V^{-1}\ s^{-1}$);[20] such correlation could be a good indication of the quality of our samples, and is considered here a figure of merit (as discussed below). The similarity between results obtained for samples of different morphology (and therefore likely defect density) can be rationalized by noting that, owing to the high frequency, and short pulse duration, the THz technique determines the conductivity on short time and length scales. As such, charge mobilities inferred from TRTS represent intrinsic upper limits for electron transport.[76] Screening literature THz reports,[20,32,33] mobilities in the range of μ ~ 30-35 $cm^2\ V^{-1}\ s^{-1}$ seems to constitute the upper threshold limit for $MAPbI_3$ solution processed crystals[24], and our results fit that number reasonably well.

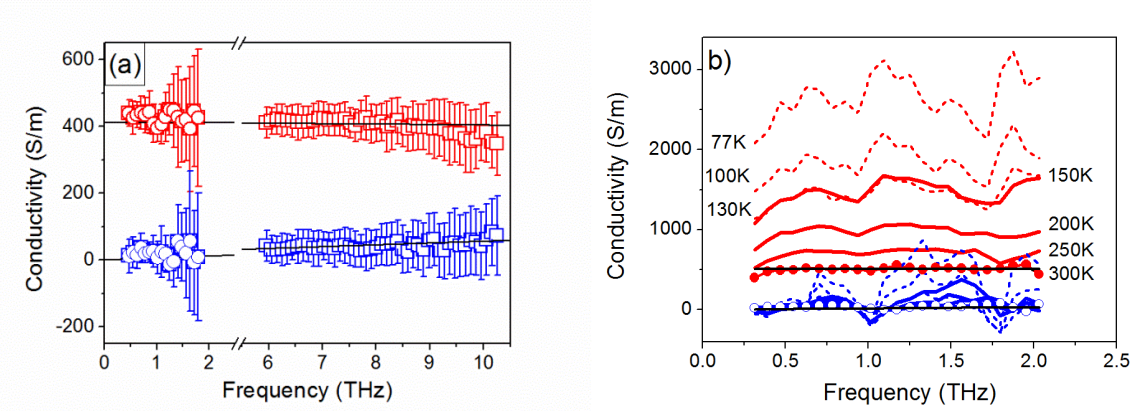

Figure 3.3 a) Real (red) and imaginary (blue) components of the complex-valued photoconductivity in the 0.3-10 THz frequency range (circles; sample deposited on fused silica, measured in the 0.3-2 THz range and squares; sample deposited on high resistivity silicon wafer, measured in the 6-10 THz range), both at room temperature in air. Black solid lines represent best fits to the Drude model to show the model is applicable up to 10 THz at room temperature. b) Complex-valued photoconductivity as a function of temperature (between 300 and 77 K) in the 0.3-2.0 THz frequency range measured at 6 ps after photo-excitation. Solid and dashed lines represent the response for the tetragonal and orthorhombic phases respectively. Black solid lines represent best fits to the Drude model as described in the text.

In line with previous studies conducted in the 0–3 THz range,[33,20,32] our THz spectroscopy results, on samples displaying state-of-the-art upper threshold mobilities, strongly support the notion of photoconductivity being purely governed by free charges, and not by bound excitons or partially confined carriers. Although exciton binding energies up to 75 meV have been reported,[25,106,107] our findings are consistent with binding energies smaller than the room-temperature thermal energy of 26 meV. Indeed, recent measurements of the static dielectric constant ε_{static} ~70 imply exciton-binding energies as low as ~2 meV.[108] The large dielectric screening necessarily suppresses Coulomb binding between electrons and holes, leading to the low exciton stability. Given the strong screening of carrier-carrier interactions, Coulomb scattering is likely to have a negligible effect on the carrier conduction in the perovskite, and the question arises: which momentum scattering

mechanisms dominate the free carrier transport? Below we will demonstrate that, in samples displaying upper-valued mobilities, pure acoustic phonon (deformation potential) scattering provide the primary mechanism limiting mobilities for the free carriers in $MAPbI_3(Cl)$ films.

As shown in Figure 3.3b, the room temperature photoconductivity spectra in the 0.3−10 THz range illustrate that the data can be reproduced well by a simple Drude-like response; in the following, we consider the 0.3−2 THz region to extract, using the Drude model, the temperature dependent scattering time. Figure 3.3b shows the evolution of the frequency-resolved complex photoconductivity for $MAPbI_3(Cl)$ films measured 6 ps after photo-excitation in the temperature range between 300 K and 77 K (the responses measured 0.5 and 1 ns after photo-excitation are equally Drude-like as shown in the Appendix, Figure 3.11). At all temperatures the photoconductivity response features a positive real part and a small positive imaginary part within the 0.3-2 THz window (fits to Drude model for all temperatures are given in the Appendix, Figure 3.12). At lower temperatures the presence of at least two resonances can be clearly resolved in the complex-valued photoconductivity respectively at ~0.9 THz and ~1.8 THz (Figure 3.3b). These spectral features in the photoconductivity are also present in the THz transmission of the unexcited perovskite film (see Appendix, Figure 3.13), and they spectrally overlap with the free carrier response (in agreement with previous observations).[20,32,33] These resonances, which have been resolved before in THz studies, have been attributed to LO-phonon modes[33,20,32] and by theoretical modelling, to sub-lattice phonon modes associated with bending and stretching of the lead-halide bonds,[109] which in this case, can be modulated by the optical excitation.[110–112] The resonances appear stronger for the orthorhombic phase in our samples, consistent with the enhancement of MA ion ordering in the low temperature phase.[96,97] From the temperature-dependence shown in Figure 3.3b, it is clear that the real part of the conductivity increases with decreasing temperature. Assuming that the excitation quantum yield remains unity, independent of the temperature, and the effective carrier mass m* changes only at the phase transition temperature (from m*=0.26 for the tetragonal phase[31] to m*= 0.56 for orthorhombic phase),[113] the only factor determining the carrier mobility according to Equation 2.9 is the mean momentum scattering time τ of the free carriers. With these assumptions we find carrier momentum scattering times increasing

from 4.5 ± 0.5 fs (at 300 K, tetragonal phase) to almost 25±0.5 fs (at 77 K, orthorhombic phase). These figures imply a mobility increase from ~27±3 $cm^2 V^{-1} s^{-1}$ at room temperature to ~150 $cm^2 V^{-1} s^{-1}$ at 77 K.

Figure 3.4 summarizes the inferred scattering times versus temperature for a sample displaying upper threshold mobilities at room T (~27±3 $cm^2 V^{-1} s^{-1}$). Notably, for temperatures above the phase transition at 150 K we find that the data can be described very well by a power law $\tau \propto T^p$ where the exponent p approaches a value of -3/2 (p = -1.52±0.05). It is important to note here that uncertainties in the assumed input parameters such as the refractive index of the fused silica substrate (see Appendix), m* and the excitation quantum yield employed for the calculation of τ would affect its absolute value, but would not significantly affect the temperature dependence and the exponent p. The obtained power law temperature-dependence of the scattering time with temperature is characteristic for free carrier transport limited primarily by acoustic phonon (deformation potential) scattering.[90] This finding is consistent with the long lived dynamics of the photoconductivity in the tetragonal phase (Figure 3.2a) found in these samples; which is indicative of low defect concentrations, e.g. intrinsic semiconducting behavior. The smaller value obtained for p below ~150 K for our samples (p = -1.18±0.13; orthorhombic phase) suggests an enhanced weight of other scattering mechanisms (e.g. impurity scattering, consistent with the below-bandgap PL emission observed below 150 K in Figure 3.2b). Interestingly, in bulk semiconductors, the theoretical limit for pure deformation potential response has been resolved for 2DEG at the interface of lattice matched GaAs/AlGaAs heterojunctions (by segregating electron transport and impurity regions by “modulation doping”.[90,114] Further work is ongoing in our group to reveal whether such scenario could be consistent with $MAPbI_3(Cl)$ samples defined by local domains of distinct nature (e.g. doping,[115] ferroelectricity[116] or crystal structure[99,100,117]).

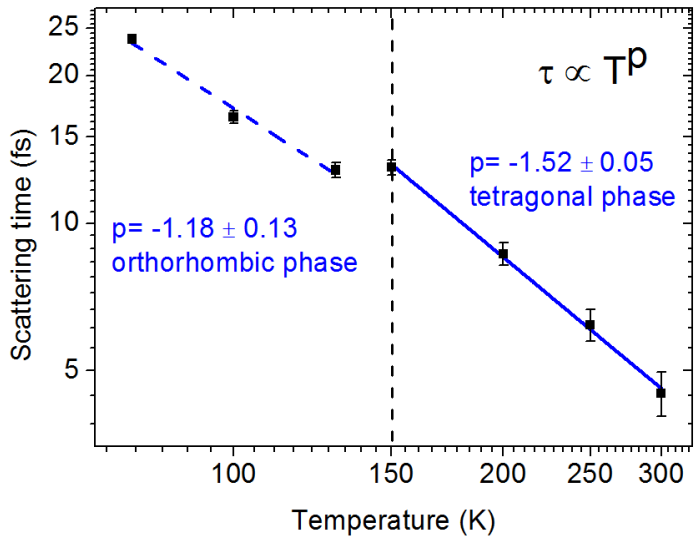

Figure 3.4 Carrier momentum scattering time versus temperature for a $MAPbI_3(Cl)$ perovskite film. The $T^{-3/2}$ dependence in the high-temperature range (tetragonal phase) is consistent with electron-phonon interactions determining the scattering time. The reduced exponent observed for the orthorhombic phase ($T < 150$ K) indicates a contribution from impurity scattering at low T.

The $T^{-3/2}$ dependence in the high-temperature range shown in Figure 3.4 is in agreement with recent work by the Herz group.[32] In that work,[32] solution processed $MAPbI_3$ samples were investigated using narrow-band THz spectroscopy; similar temperature dependent mobilities were observed for samples characterized by first-order dynamics with 66 ns lifetimes at room temperature (compared to 129 ns reported here). In both studies below bandgap defect PL emission peaks in the low temperature perovskite phase are resolved, although at different emission wavelengths – indicative of distinct defect chemistry. Both works also resolved an enhancement of the phonon modes in the orthorhombic phase, while, in contrast to our findings, a deviation from Drude-like response was observed in their work for this phase, which was assigned to charge carrier localization effects, possibly a consequence of enhanced weight of backscattering due to submicron-sized $MAPbI_3$ polycrystalline samples.[32] The large sized grains for our samples (exceeding micron length scales as revealed by SEM - see Figure 3.10) together with the lack of negative

imaginary component at all temperatures suggest that the contribution of boundary scattering to the overall signal is negligible in our samples. We note here that long lifetimes are not necessarily directly correlated with high mobilities, which are limited by scattering.[24] Our results in Figure 3.4 can also be compared to recent microwave photoconductivity measurements in $MAPbI_3$[101,118] films deposited onto mesoporous oxide matrices (Al_2O_3 and TiO_2). These works revealed power law dependencies of scattering time vs temperature with exponents p=-1.6 and -1.4 in the GHz frequency region; these results suggest that the same upper limit scattering mechanism prevails on samples in contact with an oxide scaffold (which can e.g. affect MA ordering in depleted regions).[119] Thus other scattering mechanisms, such as impurity scattering, seem to play a minor role in high mobility perovskite absorbers at room temperature (tetragonal phase). While these different reports seem consistent with each other, further work is needed to obtain clear correlations between spectroscopic fingerprints (e.g. absorbance), transport (e.g. mobility), sample structure (e.g. grain size), nature (e.g. defects), history (e.g. characterization and synthesis steps) and measurement conditions (e.g. excitation wavelength and fluence).

Intrinsic sample to sample reproducibility and/or extrinsic changes induced by the experimental conditions are important issues in the field of solution-processed perovskite films. In this work we prepared and studied up to six samples with inferred room temperature mobilities ranging from 22 to 27 $cm^2 V^{-1} s^{-1}$). Above we have discussed in detail the TRTS response vs temperature for a solution processed $MAPbI_3(Cl)$ sample with inferred room temperature mobility of μ ~27±3 $cm^2 V^{-1} s^{-1}$, close to that obtained for vapor deposited $MAPbI^3(Cl)$ films; μ = 33 $cm^2 V^{-1} s^{-1}$.[20] A detailed characterization for a separate sample showing Drude like response in the 0.3-2 THz window but with the smallest room T mobility inferred within the range of samples studied (μ~ 22±3 $cm^2 V^{-1} s^{-1}$) is given in the Appendix. For the tetragonal phase, this sample exhibits a weak, but apparent decay component within ~100 ps, (see Figure 3.14) in the TRTS carrier dynamics, and correspondingly shorter lifetimes as inferred from TRPL (see Figure 3.15). Moreover, the complex-valued photoconductivity does not exhibit the activation of phonon modes related with MA ordering as clearly as in Figure 3.3b (see Figure 3.16). Furthermore, the sample response is characterized by a smaller exponent $p < -3/2$ in the temperature-dependent scattering rates (see Figure 3.17); these results strongly suggest that other scattering mechanisms (e.g. alloy,

impurity scattering and/or piezoelectric acoustic phonon scattering) are contributing to the monitored response in this sample. It is worth commenting here that within the range of samples we characterized, we noted that "poorer" mobilities (obtained from Drude-like response) seemed to be correlated with a reduced optical density (O.D.) at ~480 nm (see Figure 3.18). We are presently analyzing these findings in detail and will report them elsewhere.

3.4 Summary

In this work we applied optical pump THz probe spectroscopy to study the nature of photoconductivity in solution processed $MAPbI_3(Cl)$ perovskite films. The virtually dispersionless real-valued broadband THz conductivity and the absence of a negative imaginary part for the conductivity at room temperature indicate that photo-generated free carriers do not experience localization or preferential backscattering at grain boundaries in our samples; a Drude response describes the data well. Finally, and arguably most importantly, we determined the nature of electron momentum scattering in methylammonium lead iodide perovskites (displaying room temperature mobilities of μ ~30 $cm^2\ V^{-1}\ s^{-1}$): we find that the momentum scattering time versus temperature for the tetragonal phase follows a $T^{-3/2}$ dependence, indicating that acoustic phonon (deformation potential) scattering represent the upper limit mechanism impeding larger mobilities in these technologically relevant materials.

3.5 Appendix

3.5.1 Sample Characterization

Structural analysis of $MAPbI_3(Cl)$ deposited on a glass substrate was conducted by X-ray diffraction (XRD, Bruker D8 Advance 2 / θθ -Diffractometer). The absorption spectra of the films were measured using a UV-Vis spectrometer (Perkin Elmer Lambda 900). Temperature dependent fluorescence spectra were measured by a J&M TIDAS II Fluorescence spectrometer combined with a liquid nitrogen cooled cryostat enabling cooling down to 77 K under $<1.4x10^{-4}$ mbar mbar vacuum conditions. The thickness of the films were measured by

a Tencor P-10 Step Profiler using 3500 µm scan length and 20 µm s^{-1} scan speed. The deposited films had an average thickness of 300 nm (rms roughness of 75 nm). Room temperature absorption and luminescence measurements reveal a band gap onset at ~775 nm (1.6 eV). For energies exceeding the band gap, the optical absorption increases smoothly towards the UV, peaking at ~480 nm (see Appendix, Figure 3.18). X-ray diffraction (XRD) (See Appendix, Figure 3.19) revealed (110), (220) and (330) peaks, characteristic for the pristine perovskite tetragonal crystal structure at room temperature.[96,97] Finally, scanning electron microscopy (SEM) revealed micron-sized crystalline domains in various substrates (see Appendix, Figure 3.10).

3.5.2 Extracting Complex Conductivity from TRTS Measurements

The details for extracting conductivity from TRTS measurements are explained in Chapter 2, Section 2.1.2. By using equation 2.2 and the parameters; d is the penetration depth of the 400 nm pump ($d \sim 90$ nm) represented as L in equation 2.2. and n is the refractive index of the unexcited substrate ($n_{fs} = 1.95$ in the case of fused silica and $n_{Si} = 3.42$ in the case of silicon), we obtain complex conductivity in $MAPbI_3(Cl)$ films.[120] The penetration depth at 400 nm wavelength was estimated by using the absorbance values shown in Figure 3.18, (measured on the fused silica substrate) and assuming a reflection coefficient R = 0.19.[107]

3.5.3 High THz frequency measurements

The high THz frequency measurements were conducted using THz air-photonics.[121] Here, the THz probe pulses were generated by dual-color laser mixing in air-plasma and detected using self-referenced air-biased-coherent detection (ABCD) to suppresses potential spectral artifacts induced by phase instabilities of the high THz frequencies.[122]

When the undoped silicon is used instead of the fused silica as a substrate, the residual transmitted optical light into the silicon (~2.5% of the incident intensity) promotes electrons in the conduction band, which are then probed together with the perovskite transient photo-conductivity. In a first approximation, the measured overall transient conductivity derived using Equation 2.2 (points in Figure 3.8) could be simply considered as the sum of the sample and substrate conductivities, $\sigma_{meas} = \sigma_{per} + \sigma_{Si}$.[83] The strength of the substrate effect to the total measured conductivity is determined by the photo-induced

carrier density in the high-resistivity silicon substrate. The latter can be evaluated under the approximation of continuous and homogenous excitation by using the Beer-Lambert law:[123]

$$N_{el}(L \pm \Delta L) = N_0 \exp\left[-\frac{L \pm \Delta L}{d}\right] \qquad (4.3)$$

where N_0 is the photo-induced electron density at the air-sample interface and $L \pm \Delta L$ and d are respectively the thickness ($L = 300 \pm 75$ nm) and the penetration depth of the perovskite layer. Since the optical reflectance at the sample/substrate interface is less than 11% we neglected any effect induced by these reflections.[124] The penetration depth of the silicon substrate ($d_{Si} \sim 100$ nm) is very close to that of the perovskite sample, which justifies the assumption of a continuous carrier density profile at the sample/substrate interface.

The transient photoconductivity of silicon has been described in detail in many studies.[125,126] By fixing both the effective mass ($0.26m_0$) of the free carriers and the scattering time (0.19 ps) with literature values, we evaluated the Drude-like silicon photoconductivity (lines in Figure 3.8) when the carrier densities were varied in the range given by Equation 4.3.[126] It should be noted that at high THz frequencies the contribution of the excited silicon to the total measured photoconductivity vanishes rapidly for the real component ($\propto 1/\omega^2$) and it mostly affects the lower frequencies of the imaginary component since the latter is proportional to $1/\omega$. To avoid what could be perceived as a too rough and arbitrary correction to the broadband photoconductivity data by subtracting the Drude photoconductivity response of the silicon substrate, we restricted our reliable spectral range over a smaller frequency window (Figure 3.9). The reconstructed photoconductivity of our perovskite sample was then divided by the carrier density of the low frequency THz photoconductivity measurements for comparison (Figure 3.3a) since the photoconductivity signal is simply proportional to the pump fluence (Figure 3.5). We notice that even in the entire conductivity spectra, no relevant dispersion can be observed until frequencies >12 THz are approached, and the imaginary conductivity grazes zero over a wide frequency range. The error bars shown in Figure 3.3a were estimated from the statistics of the measured transient transmissivity.

Responses < 6 THz and > 10 THz frequency windows (Figure 3.9) are compromised by few technical (t) and fundamental (f) aspects: (t1) For the broadband THz data, a higher excitation fluence was needed to get meaningful S/N ratios in ABCD detection (Air-Biased Coherent Detection); although the maximal photoinduced amplitude of the signals over this pump range is linear (see Figure 3.5 - right) – dynamics at this excitation are bimolecular. (t2) There is a significant signal arising from silicon on broadband measurements made on transmission < 6 THz (see Figure 3.8), also, silicon and perovskite phonons >10 THz can potentially contribute to the overall signal (see Figure 3.9).[90,127] (t3) The signal to noise ratio rapidly increases at frequencies above 10 THz. (t4) The slight drop-off affecting frequencies < 4 THz for the broad band data can be contributed to an artifact due to diffraction-limited beam waist (frequency components approaching the diameter of the optical pump beam). (f1) samples compared in Figure 3.3a are different (e.g. deposited in different substrates, which can affect e.g. sample morphology as illustrated in Figure 3.10); however, the quantitative agreement in the real conductivity amplitude of the signals is notable, implying that mobilities for the 3 samples are the same.

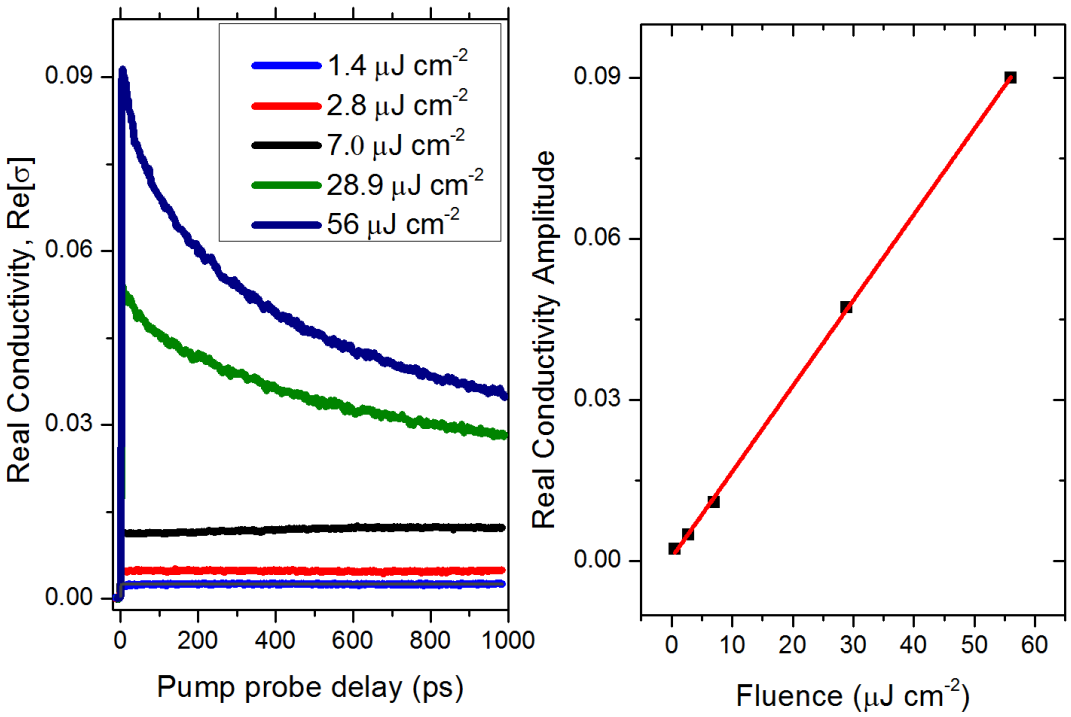

Figure 3.5 (left) Fluence dependent photoconductivity versus pump probe delay measured in $MAPbI_3(Cl)$ perovskite at 400 nm pump wavelength under vacuum. (right) Real conductivity amplitude versus fluence at 10 ps pump probe delay.

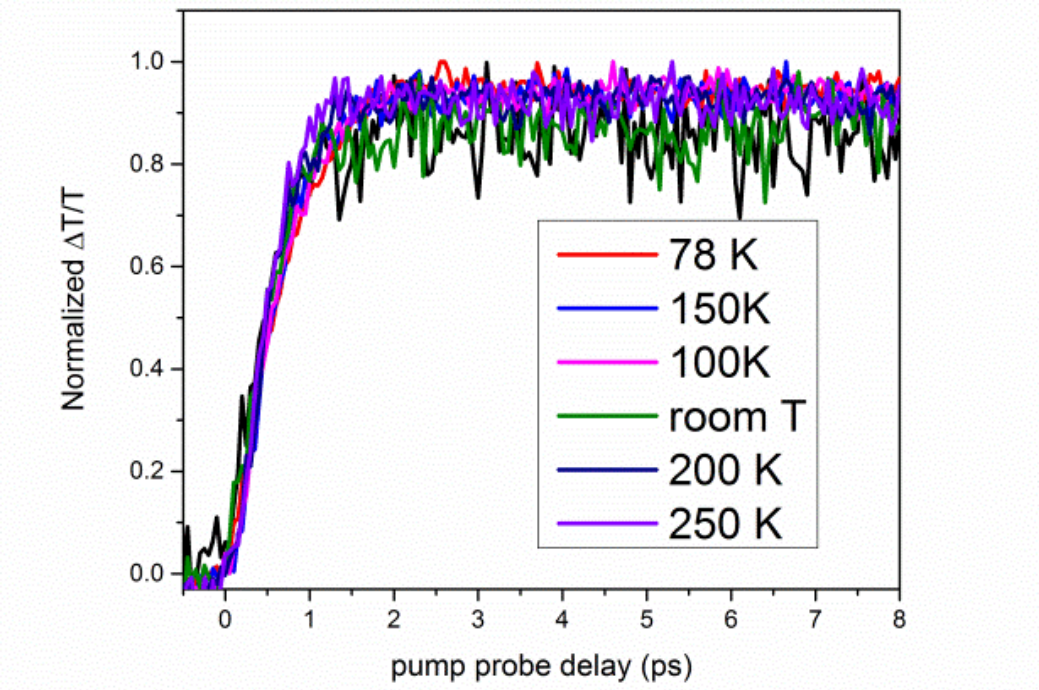

Figure 3.6 High resolution TRTS dynamics vs temperature in $MAPbI_3$ (Cl) perovskite.

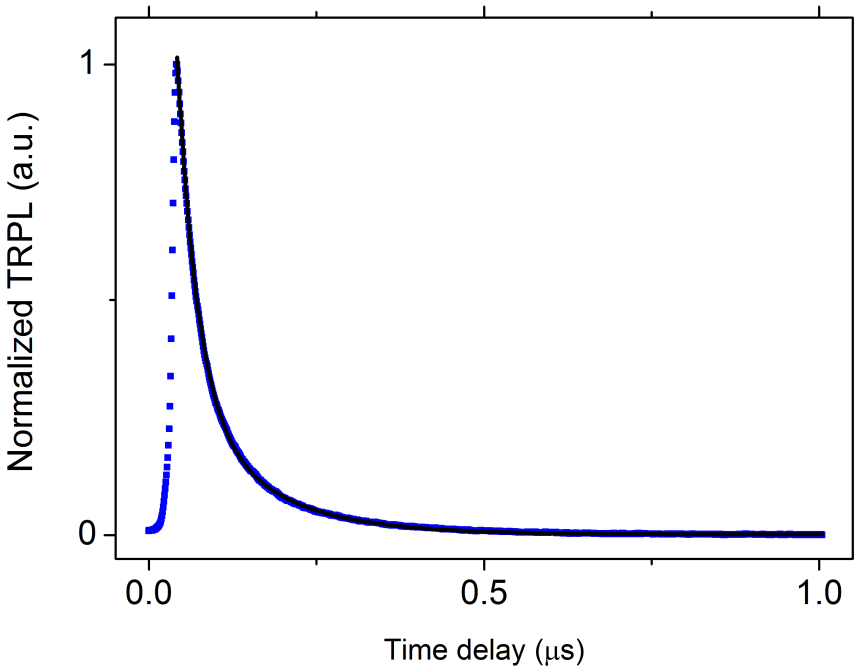

Figure 3.7 Time resolved photoluminescence dynamics (blue) and exponential fits (black). Excitation wavelength 400 nm, fluence 45 μJ cm^{-2}, under vacuum. Biphasic decay dynamics for the ~775 nm emission with τ_1(300 K) = 30.8±0.1 ns (88% amplitude) and τ_2(300 K) = 129.1±0.7 ns (12 % amplitude).

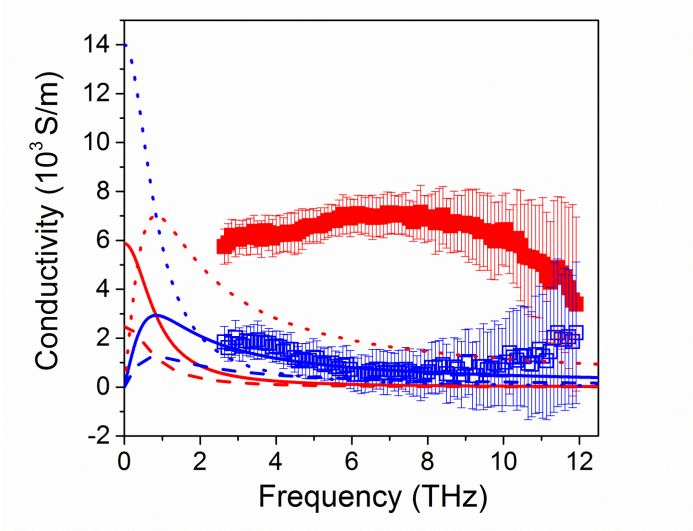

Figure 3.8 Squares: real (red) and imaginary (blue) measured transient photoconductivity of the $MAPbI_3$ (Cl) perovskite film on the high-resistivity silicon substrate ($\sigma_{per} + \sigma_{Si}$). Lines: modeled real (red) and imaginary (blue) photoconductivity components induced by the silicon substrate after absorption of residual transmitted pump excitation. The silicon response is calculated by assuming respectively the expected $MAPbI_3$ (Cl) thickness (300nm; solid lines) and deviations given by the roughness of the sample (375 nm; dotted line and 225 nm; dashed lines).

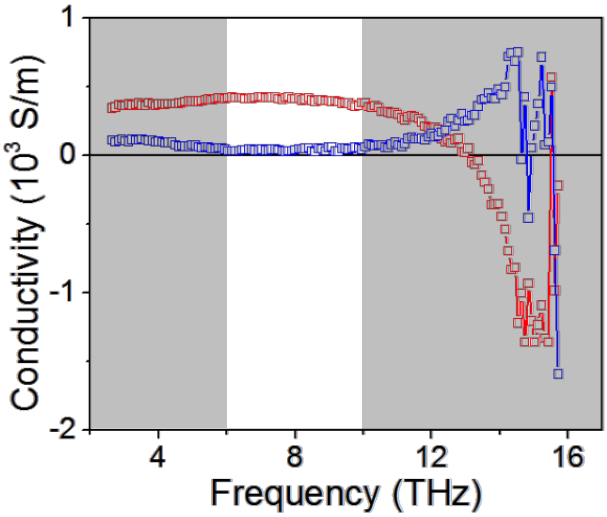

Figure 3.9 Reliable window (white) of the real (red) and imaginary (blue) components of the complex-valued photoconductivity for a sample deposited on high resistivity silicon wafer measured in transmission.

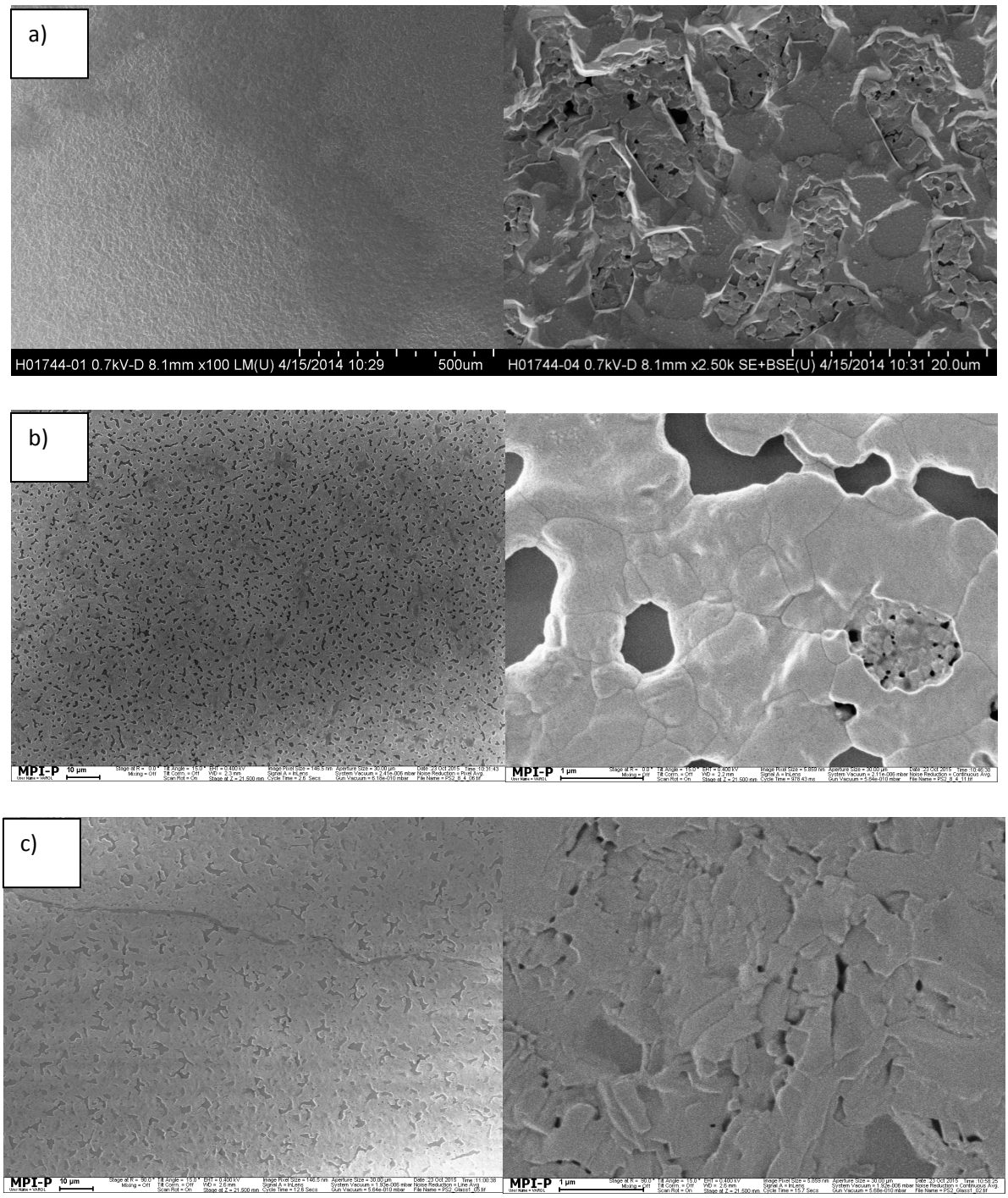

Figure 3.10 Representative SEM images of $MAPbI_3$ (Cl) perovskite film on various substrates, a) silicon (500 μm-left and 20 μm-right scales), b) fused silica (10 μm-left and 1 μm-right scales) and c) glass (10 μm-left and 1 μm-right scales) showing micron sized $MAPbI_3$(Cl) crystals.

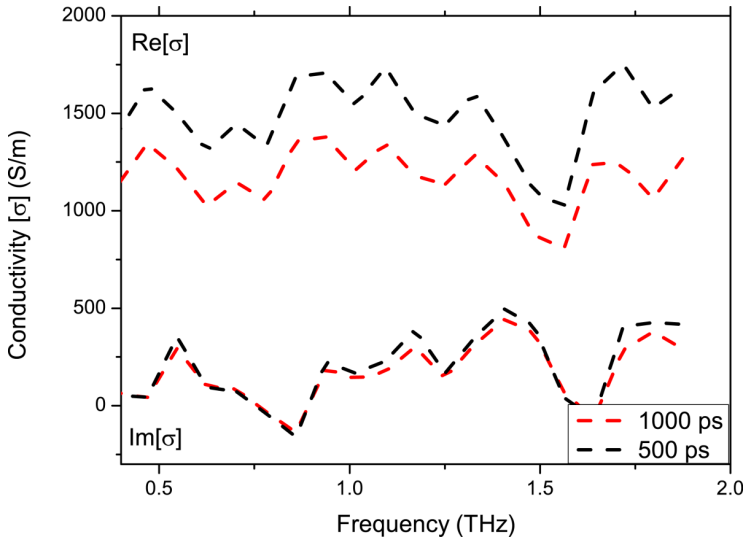

Figure 3.11 Frequency resolved complex photoconductivity for a $MAPbI_3$ (Cl) perovskite film at 77 K under vacuum for pump-probe delay at 500 ps and 1000 ps. Pump wavelength 400 nm, fluence 2.8 μJ cm^{-2}.

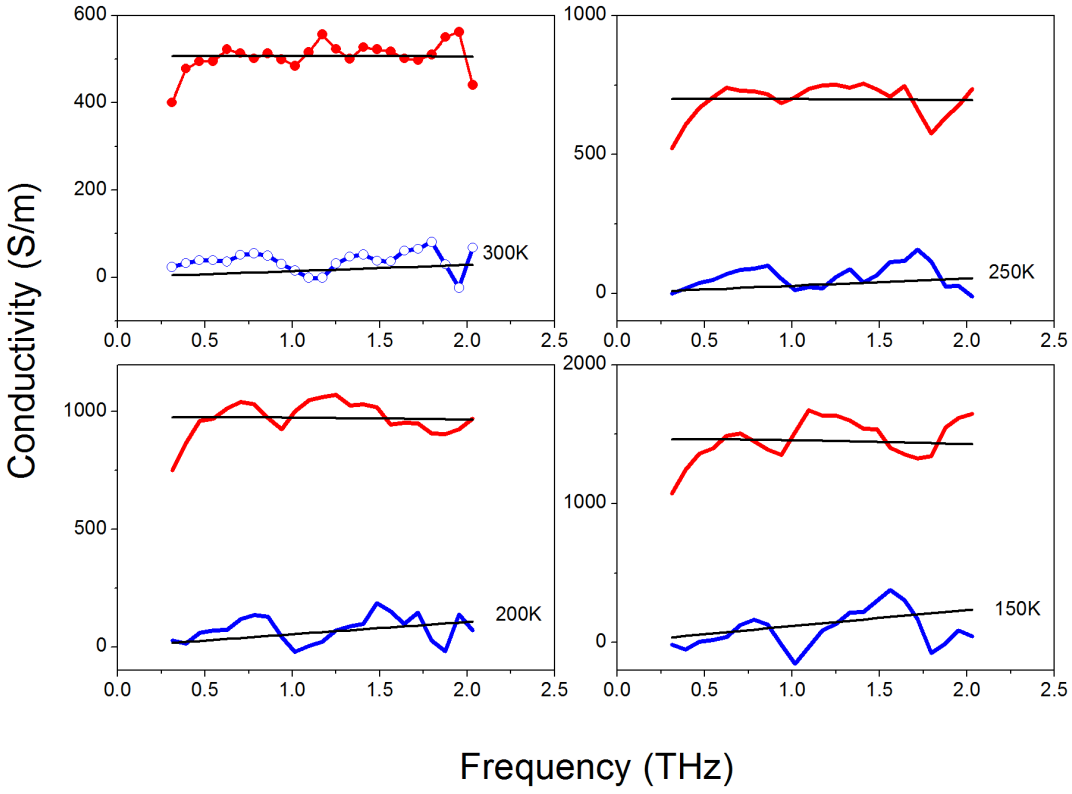

Figure 3.12 Drude fits (black solid lines) for complex-valued photoconductivity as a function of temperature (between 300 and 150 K-data in Figure 3.3b) in the 0.3-2.0 THz frequency range measured at 6 ps after photo-excitation.

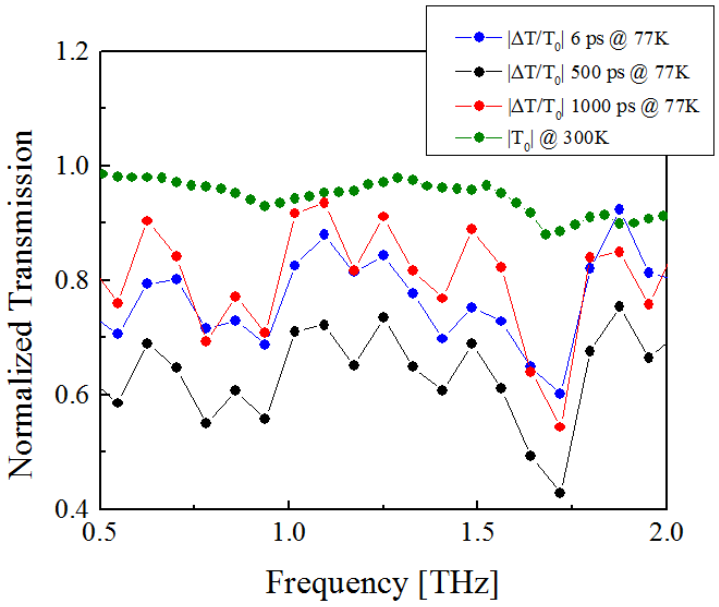

Figure 3.13 Steady state THz transmission (not photo-induced; green line-dot trace) versus frequency at 300K compared with photo-induced THz transmission for pump-probe delay at 6 ps (blue line-dot trace), 500 ps (black line-dot trace) and 1000 ps (red line-dot trace) measured in a $MAPbI_3$ (Cl) perovskite film at 77K.

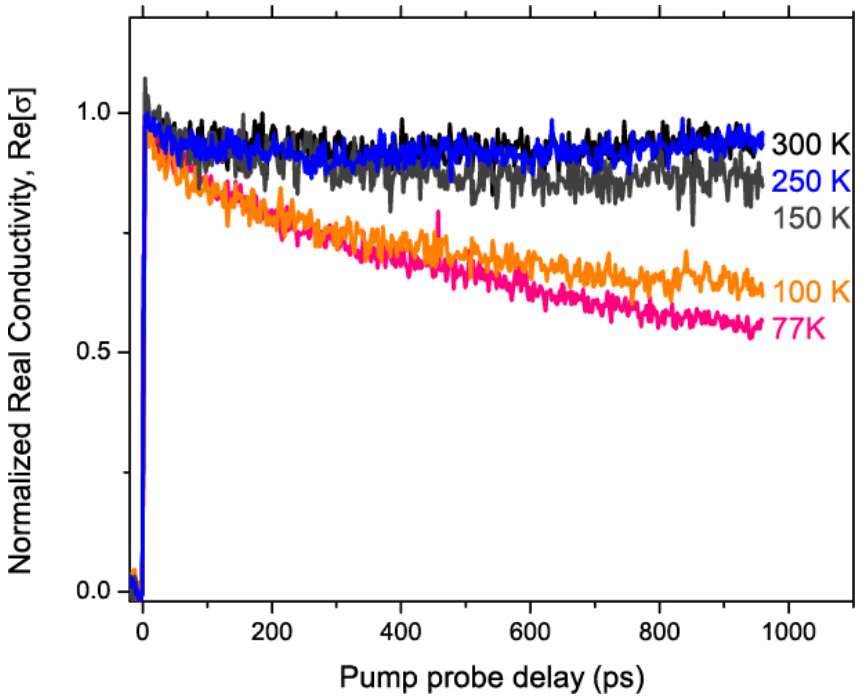

Figure 3.14 Temperature dependent optical pump-THz probe conductivity versus pump-probe delay in a $MAPbI_3$ (Cl) perovskite film with reduced OD at 480 nm (red trace in Figure 3.15). Excitation wavelength 400 nm, fluence 2.8 μJ cm^{-2}, under vacuum.

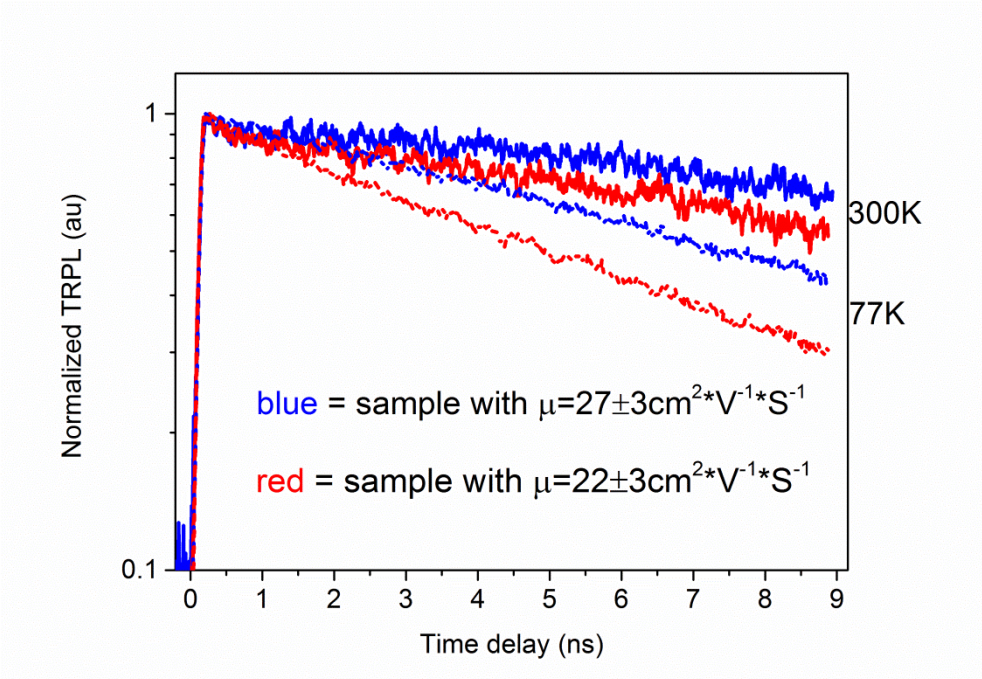

Figure 3.15 Time resolved photoluminescence dynamics for the 2 samples with maximum and minimum mobilities. Excitation wavelength 400 nm, fluence 9 μJ cm^{-2}, under vacuum.

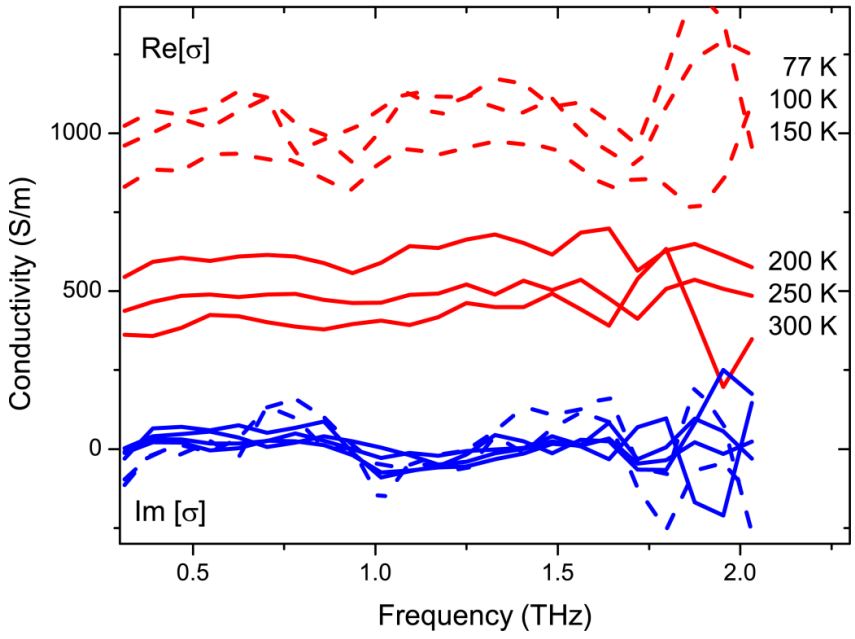

Figure 3.16 Complex-valued photoconductivities as a function of temperature measured 6 ps after photoexcitation under vacuum in $MAPbI_3$ (Cl) perovskite film with reduced OD at 480 nm (red trace in Figure 3.18).

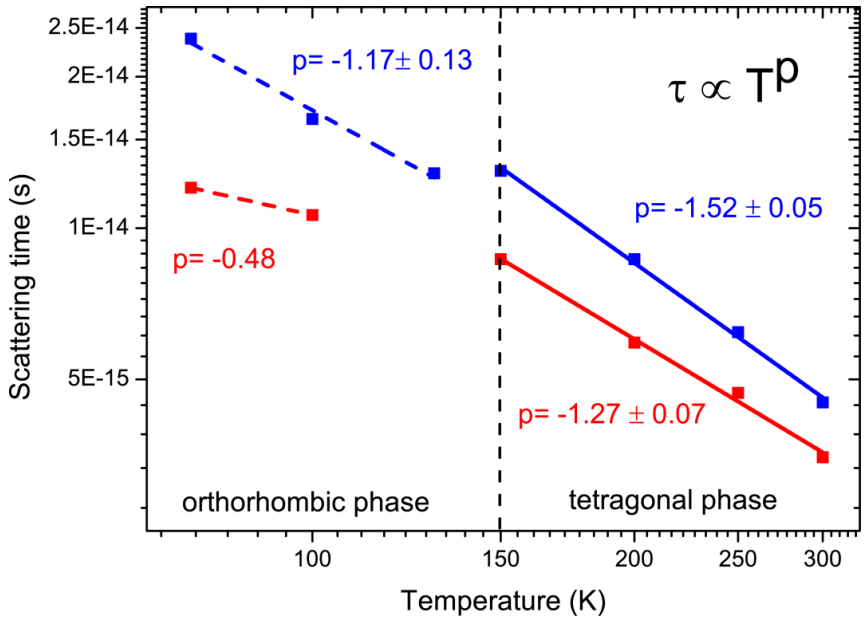

Figure 3.17 Comparison of scattering times vs temperature for 2 $MAPbI_3$ (Cl) perovskite films (blue - sample with μ 27 $cm^2 V^{-1} s^{-1}$; red - sample with μ 22 $cm^2 V^{-1} s^{-1}$) with different OD at 480 nm (Figure 3.18).

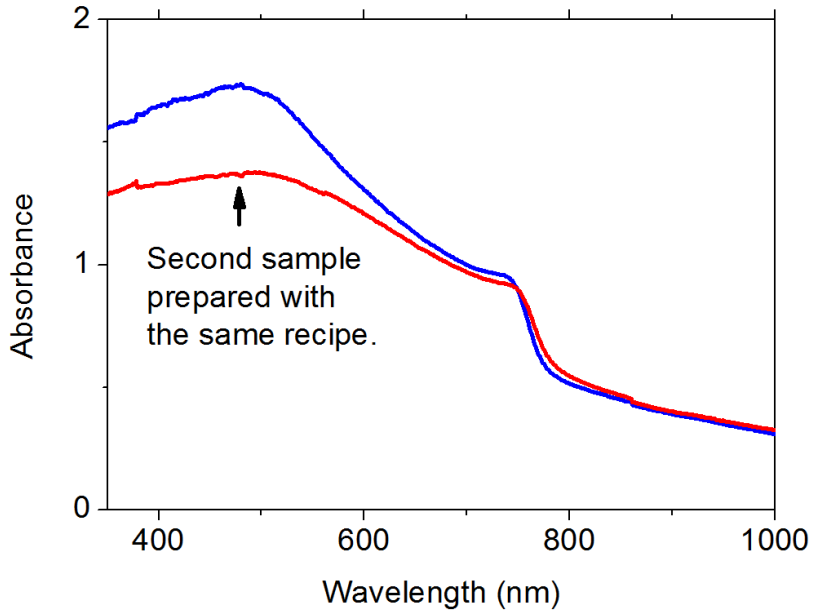

Figure 3.18 Absorbance spectrum of two freshly prepared $MAPbI_3$ (Cl) perovskite films with maximum and minimum mobilities (blue-sample with μ = 27 $cm^2 V^{-1} s^{-1}$; red-sample with μ = 22 $cm^2 V^{-1} s^{-1}$).

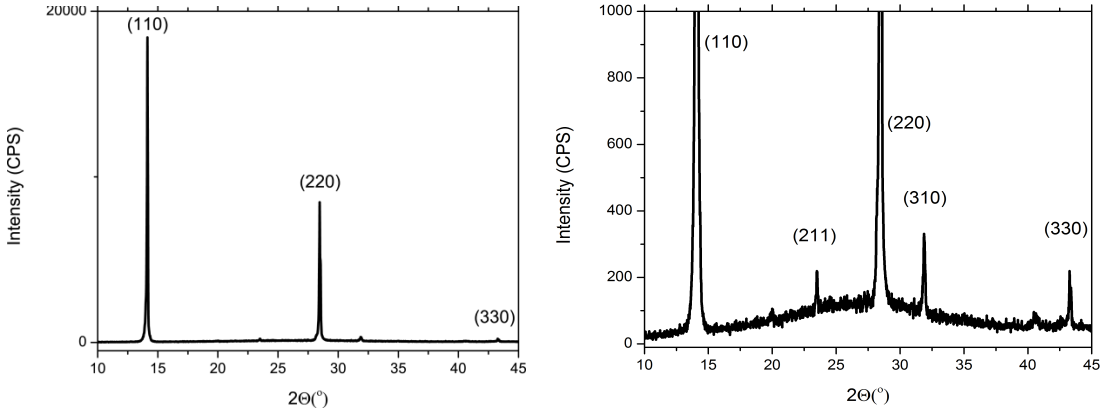

Figure 3.19 XRD patterns of $MAPbI_3(Cl)$ perovskite film spin-coated on a glass slide (left). Same spectra with zooming into the low intensity peaks (right).

Chapter 4

Electron transfer from 4,4'-dicarboxylic acid-2,2'bipyridine emerges upon dye photodegradation in N3 sensitized TiO_2

The long-term stability of dye sensitized solar cells (DSSCs) is determined to a large extent by the photodegradation of their sensitizers. Understanding the mechanism of light-induced decomposition of dyes sensitizing a mesoporous oxide matrix may therefore contribute to solutions to increase the life span of DSSCs. Here, we investigate, using ultrafast terahertz photoconductivity measurements (Figure 4.1), the evolution of interfacial electron transfer (ET) dynamics in N3 dye-sensitized mesoporous TiO_2 electrodes upon dye photodegradation. Under inert environment, interfacial ET dynamics do not change over time, indicating that the dye is stable and photodegradation is absent; the associated ET dynamics are characterized by a sub-100 fs rise of the photo-conductivity, followed by long-lived (>>1 ns) electrons in the oxide electrode. When the N3-TiO_2 sample is exposed to air under identical illumination conditions, dye photodegradation is evident from the disappearance of the optical absorption associated with the dye. Remarkably, approximately half of the amplitude associated with the sub-100 fs ET is observed to still occur, but is followed by very rapid (~10 ps) electron-hole recombination. Laser desorption/ionization mass spectrometry, attenuated total reflection FTIR and terahertz photoconductivity analyses reveal that the photo-degraded ET signal, and the fast electron-hole recombination, originates from the N3 dye photodegration product as dcbpy (4,4'-dicarboxy-2,2'-bipyridine), which remains bonded to the TiO_2 surface via either bidentate chelation or bridging type geometry.

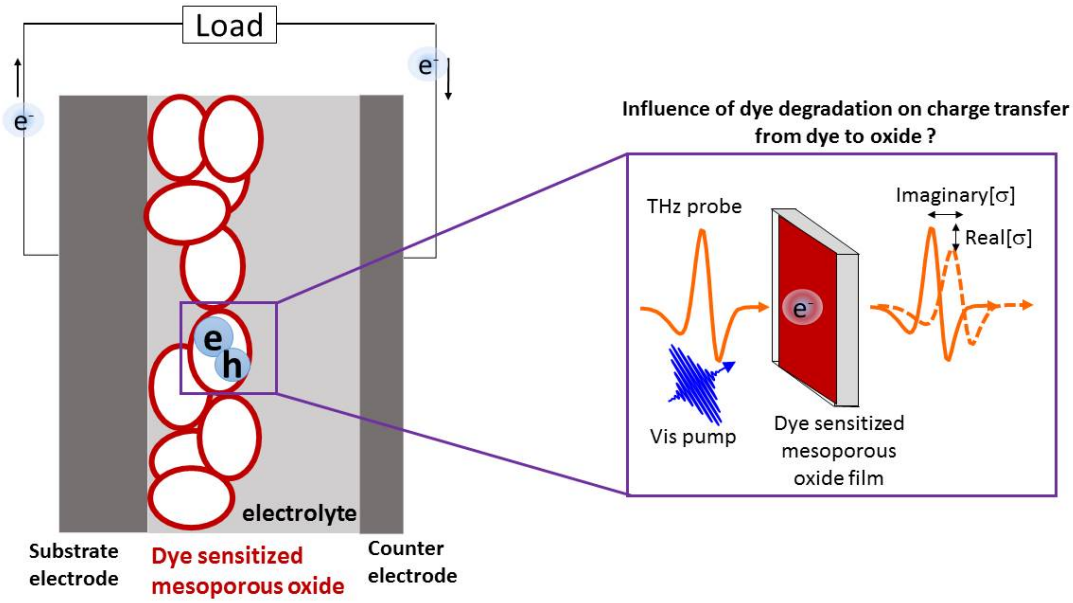

Figure 4.1 Schematic representation of TRTS experiment in dye sensitized mesoporous oxide films deposited on a flat substrate.

4.1 Introduction and aim of the work

Understanding the nature of photo-induced interfacial electron transfer (ET) dynamics at dye-oxide interfaces is fundamental for the rational design and development of sensitized architectures that can be exploited in solar energy conversion architectures (e.g. solar cells and solar fuels).[36,45,49,58] Although ET dynamics have been widely investigated for the N3 dye (Ru[4,4'-dicarboxylic acid-2,2'-bipyridine]$_2$[NCS]$_2$) sensitizing mesoporous TiO_2 electrodes, considerable debate remains regarding the nature of the ET process. In general, interfacial ET rates in N3-TiO_2 have been reported to be bi-phasic,[52,128–130] however, the precise ET time constants and the relative amplitudes of these 2 ET pathways differ substantially among the various reports, evidencing a strong dependence upon sample preparation and measurement history. Moreover, photodegradation of the dye sensitizer has been suggested to substantially affect the nature of interfacial ET rates and consequently the interpretation of interfacial ET signals.[131,132]

In this study, we investigate interfacial ET dynamics in N3 sensitized mesoporous TiO_2 electrodes upon purposely and controlled photodegradation of the dye. The degree of dye

photodegradation affects both the interfacial ET rates and the total amount of electrons transferred. Remarkably, we demonstrate that when the dye photodegradation is complete, i.e. when the N3-TiO_2 sample absorbance lacks any N3 dye related transitions, we still resolve a sub-ps ET signal equivalent to ~50 % of the non-degraded signal amplitude. This observation can be explained by the chemical identity of the N3 photodegradation products; combining LDI-TOF-MS, ATR-FTIR and TRTS characterization we conclude that the N3 dye is converted into dcbpy (4,4'-dicarboxy-2,2'-bipyridine), which sensitizes the TiO_2 electrode via either bidentate chelation or bridging type coordination. The surface-bound dcbpy gives rise to sub-picosecond charge injection into the oxide very similar to the N3 dye, but the injected charge recombines rapidly with the hole remaining on the dcbpy after ET.

4.2 Materials and Methods

TiO_2 paste is used as purchased from Solaronix (Ti-Nanooxide T). The corresponding oxide films are prepared by the doctor blading technique on fused silica substates (LG Optical Ltd.) The films were dried at 150 °C for 1 hour and sintered at 450 °C for 2 hours in an oven. The resulting films are immersed in $5.0*10^{-4}$ M solutions of Ru(4,4'-dicarboxylic acid-2,2'-bipyridine)$_2$(NCS)$_2$ (N3 dye) (Solaronix) and 4,4'-dicarboxy-2,2'-bipyridine (dcbpy) (Sigma Aldrich) in ethanol (≥ 99.5 Sigma Aldrich).

Photodegradation. Photodegradation of the samples is achieved under 400 nm photoexcitation (1 kHz pulses at a fluence of 20 μJ/cm^2) and ambient conditions. Applied fluence is selected in the first order regime according to fluence dependence measurements.

Laser desorption/ionization time of flight mass spectrometry (LDI-TOF-MS). All mass spectrometry experiments were performed on a SYNAPT G2-Si instrument (Waters Corp., Manchester, UK) with a matrix-assisted laser desorption/ionization (MALDI) source. For the analysis of the fused silica substrate with the N3 dye on TiO_2, the sample wafer was fixed on the MALDI sample plate by a double-sided adhesive tape. A frequency-tripled Nd:YAG solid state laser (355 nm) was used, operated at a repetition rate of 1000 Hz. The mass range between 50 and 2000 Da was recorded at a resolution of 10000. The laser power was adjusted in an intermediate range, slightly above the desorption threshold for intact molecules, to avoid irradiation damage of surface bound dye molecules. The spectrum of

each sample was acquired for 3 minutes to obtain representative signals from bleached and unbleached surface regions.

4.3 Results and Discussions

4.3.1 Evolution of carrier dynamics upon dye photodegradation in N3-TiO_2 electrodes

The sub-picosecond dynamics of dye-oxide electron transfer are monitored using optical pump-Terahertz probe, or time-resolved THz spectroscopy (TRTS). Following optical excitation of selectively the dye molecules, the photoconductivity of the sample is measured using ~1 ps long, single cycle THz pulses. THz spectroscopy allows for contact-free measurements of the conductivity by measuring the effect of charge carriers on the THz pulse of propagation through the sample. Prior to ET, the conductivity of the sample is zero, as the excited electrons in the dye molecules are not mobile. Following ET into the conduction band of the oxide, the conductivity will become finite, owing to the free motion of charge carriers. Recombination with the hole remaining on the dye molecule (or trapping in the oxide) will cause a subsequent decay of the conductivity.

Figure 4.2a shows the evolution of the carrier dynamics monitored by TRTS when an N3-sensitized TiO_2 sample is photo-excited by 400 nm light (20 μJ/cm^2, 100 fs FWHM) under air during 25 hours. In absence of the dye, the bare TiO_2 shows no photo-response. As evident from Figure 4.2a, under these ageing conditions, the TRTS signal evolves over time, changing both its shape and its amplitude. The black trace in Figure 4.2a (labelled as 0 hours) represents the TRTS response of the sample when dye photodegradation was prevented by preparing and measuring the sample under inert N_2 environment conditions. Once the 400 nm pulse excites the sample (zero pump probe delay in Figure 4.2a), an instrument-limited sub-120 fs rise of real conductivity is observed, which then remains constant on at least a nanosecond timescale and scales linearly with pump photon flux. Under inert N_2 environment, this experiment can be repeated over hours, without any noticeable change in the dynamics. The sub-ps rise of the photoconductivity points to ET taking place from the N3 dye into the TiO_2 acceptor; the subsequent absence of photoconductivity decay over the

probed 400 ps time window indicates a lack of recombination of photo-generated free electrons in the TiO_2 conduction band (with a lifetime >>1 ns). Ageing of the sample is triggered by exposing it to air under the same 400 nm irradiation conditions. As evident from Figure 4.2b, photodegradation is associated with the disappearance of the dye-related absorbance, and the appearance of a featureless absorbance which extends to the IR. The time evolution from 1 h to 25 h of the photoconductivity response upon photodegradation is shown in Figure 4.2a. These results reveal an increasingly rapid decay of the photoconductivity, which eventually becomes zero at pump-probe delays > 100 ps (i.e. no electrons left in the oxide). Remarkably, the sub-ps rise of the photoconductivity does not vanish completely, but only fades to approximately half of the initial amplitude, to then remain constant (also this TRTS signal scales linearly with pump fluence). The sub-ps rise for the fully photo-degraded sample indicates that, despite the degradation, substantial transfer of electrons from dye photoproducts into the oxide occurs. These electrons, however, are only short lived: the observed ~10 ps photoconductivity decay component points to rapid electron back-transfer and electron hole-recombination.

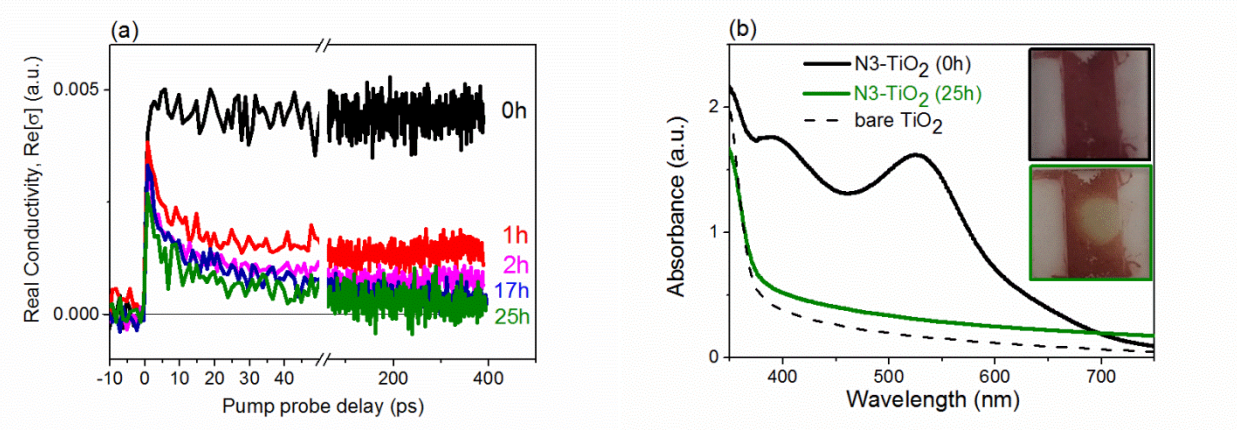

Figure 4.2 (a) The evolution of carrier dynamics in N3 sensitized mesoporous TiO_2 upon photodegradation (from 0 to 25 h; from black to green trace) measured by time-resolved terahertz spectroscopy. (b) The evolution of the absorbance of N3-TiO_2 sample prior photodegradation (0h) and after 25 h of photodegradation (400 nm photoexcitation under air); the black dash line represents the bare oxide absorbance; the insets show pictures of the N3-TiO_2 sample at 0 h (top) and after 25 h (bottom) of photodegradation.

The photo-conductivity Re[σ] of free electrons in the oxide CB is proportional to the product of the number N_e and mobility μ of electrons in the material: Re[σ] $\propto N_e \cdot \mu$. The overall reduction of Re[σ] shown in Figure 4.2a is consistent with a reduction in electron density in the oxide conduction band upon N3 photodegradation: over time, fewer sensitizers inject electrons contributing to the photo-induced real conductivity. This assignment is fully consistent with previous reports on quantum dot-sensitized systems.[88,89,133] The results shown in Figure 4.2a demonstrate that, even after full photodegradation, electrons are still injected into the oxide on a sub-120 fs timescale. The number of electrons injected in this manner is approximately half of those of the pristine dye, and decays very quickly, and will not contribute substantially to the photocurrent in a device unless holes can be removed from the photoproduct at a similar rate. In the next sections we interrogate the nature of these signals and discuss its possible chemical identity.

4.3.2. Frequency-resolved photoconductivity upon dye photodegradation in N3-TiO_2 electrodes

To unravel the nature of the remaining photoconductivity signal after full N3 dye photodegradation, we investigate the frequency-resolved complex photoconductivity measured by TRTS prior and after N3-TiO_2 photodegradation. As evident from Figure 4.3, the frequency-resolved complex photo-conductivity (recorded at 1.5 ps pump-probe delay) is shape-wise identical before and after N3 photodegradation, only decreasing in its overall amplitude, consistent with the reduced peak photoconductivity upon photodegradation. The observed frequency-resolved complex photo-conductivity response in the THz region for N3-TiO_2 samples prior and after dye photodegradation can be well modelled by the phenomenological Drude-Smith (DS) conductivity model, where the photoconductivity is attributed to free carriers experiencing preferential backscattering events at the boundaries of the nanocrystalline mesoporous TiO_2 electrode.[134,76] Fitting the complex photoconductivity data using the DS model provides indistinguishable fitting parameters; with scattering times (τ) and backscattering parameters (c) of $\tau = 55 \pm 5$fs and $c = -0.81 \pm 0.02$. These results, which agree quite well with previous THz reports analyzing the THz photoconductivity on

dye sensitized and bare TiO_2 electrodes,[104,134–136] demonstrate that the nature of the TRTS signal for both the pristine and the fully photodegraded sample (associated with a featureless background absorbance) originate from photo-induced free electrons populating the oxide conduction band.

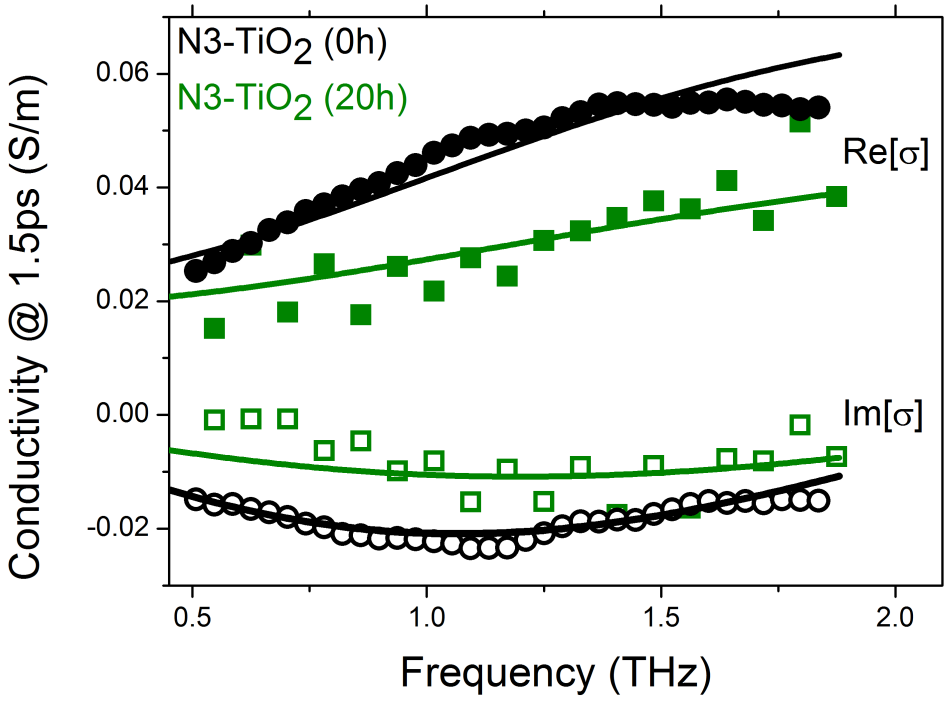

Figure 4.3 Frequency-resolved complex photoconductivity in N3 sensitized mesoporous TiO_2 at the beginning (0h) (black circles: solid-real conductivity, empty-imaginary conductivity) and after (20h) photodegradation (green diamond: solid-real conductivity, empty-imaginary conductivity) at 1.5 ps pump delay. Black and green solid lines represent Drude-Smith fits, with $\tau = 55$ fs and $c = -0.81$ for both samples, with a 1.65 scaling factor between the pristine and photo-degraded sample.

4.3.3 Chemical identity of the ultrafast photoconductivity signal in the fully photodegraded N3-TiO_2 electrode

Photodegradation products of Ru based dyes (including N3) have been investigated previously by other authors.[53–55,137–140] Several photo-products have been identified, e.g. the formation of bis(cyano) complexes (known as Ru505 dyes) by Sulfur loss,[138] the formation of

complexes with H_2O or OH^- ligands by a ligand exchange reaction[53] and/or the formation of moieties from the N3 dye by a ligand dissociation reaction.[140,55] In our fully photodegraded N3-TiO_2 electrode (see Figure 4.2b), the observed featureless absorbance suggests a lack of Ru metal-to-ligand transitions.[138,141,142] In order to identify the nature of the photoproducts in our fully degraded samples, we performed laser desorption/ionization time of flight mass spectrometry (LDI-TOF-MS) and ATR-FTIR measurements.

The N3-sensitized TiO_2 electrode irradiated during 25 h was characterized by LDI-TOF-MS. Two micron-sized spots with a different degree of discoloration (and hence dye photodegradation, see Figure 4.4a inset) were investigated by LDI-TOF-MS separately under identical experimental conditions. The results are shown in Figure 4.4a. Both spectra, which are normalized to the same noise level (at 100m/z) to allow for a better comparison of relative amplitudes, reveal rich LDI-MS spectra, in particular associated with photo-products upon N3 dye photodegradation. The unbleached, pristine region, shows only weak signal intensities as opposed to the strongly discolored irradiated region, which can be explained by an increased amount of "loose" N3 decomposition products already detached from the TiO_2 surface. Among the peaks resolved for the fully bleached area, signals at 244 Da, 488 Da and 470 Da, highlighted with *'s in the figure, can be unambiguously assigned to dcbpy, dcbpy dimers and an anhydride of the dcbpy dimer, respectively. The appearance of dcbpy fragments after N3-TiO_2 photodegradation demonstrates that at least one decomposition pathway for the N3 dye involves the breaking of non-covalent dcbpy-ruthenium bonds, which is consistent with the absence of Ru-ligand compounds in the absorption spectra in Figure 4.2b.

To evaluate whether dcbpy moieties remain bonded to the oxide electrode upon full photodegradation we performed ATR-FTIR measurements. Figure 4.4b shows the ATR-FTIR spectra of free N3 dye powder film (black dashed line), N3 dye sensitized TiO_2 before (black line) and after (green line) full photodegradation and dcbpy-sensitized TiO_2 (blue line). First we comment on the spectra of intact N3 and N3-TiO_2 electrodes. The vibrational bands for the N3 dye at 1735 cm^{-1} and 1705 cm^{-1} have previously been assigned to C=O stretching of carboxylic trans- to –NCS and pyridine respectively.[143] The bands in the 1400–1600 cm^{-1} range have been associated with C=C stretching modes from the bipyridyl units. After dye

attachment to the oxide, the band at 1740 cm^{-1} is barely affected, suggesting that some carboxylic acids remain unbound; the disappearance of the 1708 cm^{-1} band from the bare N3 dye after bonding to TiO_2 suggests that the carboxylic acids in trans confirmation to pyridine are involved in the bonding, as also previously suggested by other authors.[143] Direct evidence of the bonding of the N3 dye onto the oxide is revealed by the appearance of asymmetric and symmetric stretch of the deprotonated carboxylate groups at 1597 cm^{-1} and 1381 cm^{-1}. The frequency difference between these bands has previously been used as a criterion to determine the bonding geometry of the dyes.[143–147] For our samples, the difference between the symmetric and asymmetric bands (216 cm^{-1}) is consistent with the N3 dyes being attached to the oxide via bridging or bidentate coordination. As evident from Figure 4.4b, we observe the same frequency difference between carboxylate asymmetric and symmetric bands for the sample which is fully photodegraded (green line Figure 4.4b); this strongly suggest that dcbpy moieties remain attached to the oxide surface upon full dye decomposition. In support of this finding, the same frequency difference between the carboxylate symmetric and asymmetric bands is revealed for samples consisting of dcbpy sensitizing TiO_2 (blue line Figure 4.4b). Finally, the appearance of a feature at 1650 cm^{-1} for the fully photodegraded sample is tentatively attributed to C=N stretches of dcbpy units (when Ru bonds are broken). This assignment is supported by the identical feature observed in the dcbpy-sensitized TiO_2 sample and the LDI-TOF-MS spectra discussed above. Taken together, these observations indicate that dcbpy moieties from the N3 dye remain attached to the oxide surface in the fully photodegraded N3-TiO_2. As such, the ultrafast TRTS signal upon complete sample photodegradation shown in Figure 4.2a most likely refers to dcbpy fragments sensitizing the TiO_2 electrode.

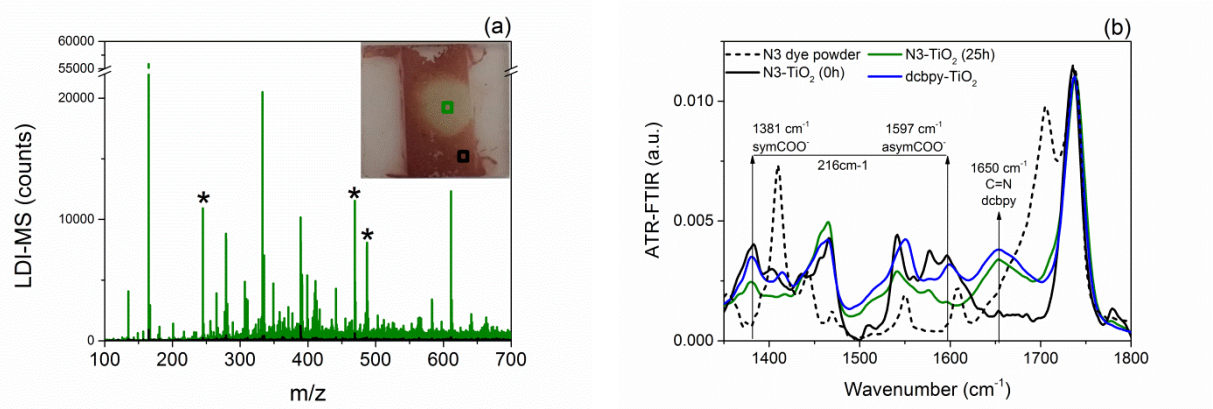

Figure 4.4 (a) LDI-TOF-MS spectrum of N3-TiO_2 (0h, black trace) and photodegraded N3-TiO_2 (25h, green trace). The inset shows picture of the N3-TiO_2 sample for the non-photodegraded area, referred as 0 h (top, highlighted in green) and after 25h (bottom, highlighted in black) of photodegradation. (b) FTIR spectra of N3-TiO_2 (0h, black line), photodegraded N3-TiO_2 (25h, green line), N3 film (dashed line) and dcbpy-TiO_2 (blue line). Note the remarkably good agreement between the spectra of the photodegraded sample (green) and the dcbpy-TiO_2 sample (blue).

To verify this hypothesis, we conducted TRTS measurements of dcbpy-sensitized TiO_2 electrodes. As shown in Figure 4.5a, both the dynamics and the frequency-resolved conductivity of the dcbpy-TiO_2 sample agree well with those obtained for the fully photodegraded N3-TiO_2 electrodes. The fast back electron recombination dynamics associated with dcbpy-TiO_2 sample can be associated to a stronger coupling between HOMO orbital in dcbpy and electrons in the oxide CB when compared with pristine N3-TiO_2 electrodes (where the HOMO of N3 dye is physically located further from the oxide surface, namely at the –SCN groups). Also consistent with our hypothesis, the TRTS dynamics of the dcbpy-TiO_2 sample barely evolve upon photodegradation and the absorbance induced by dcbpy attachment to the TiO_2 electrode is further consistent with that obtained for the fully photodegraded N3-TiO_2 sample (Figure 4.5a - inset). Finally, the frequency-resolved complex conductivity response for the dcbpy-TiO_2 electrode can be well described by the DS model with τ= 80 fs and c= -0.63, revealing that the nature of the TRTS signal refers to free carriers populating the oxide electrode. All these findings demonstrate that dcbpy remains attached to the oxide surface upon N3-TiO_2 electrode photodegradation, and that dcbpy provides an

ultrafast ET path to the TiO_2 electrode. These findings are also consistent with previous works where the dcbpy molecule was employed as a model system for better understanding the nature of ultrafast ET processes at N3-TiO_2 interfaces.[148–150] The dcbpy molecular adsorption onto TiO_2 surface was found to promote a new ground state for the dcbpy molecule which is located ~1 eV below the conduction band of TiO_2.[50,150] Both experiment[50,148,149,151] and theory[148,150,152] have revealed that strong coupling between dcbpy and the oxide provide fs ET paths towards the TiO_2 electrode under UV irradiation; these paths can be related with a direct adiabatic ET mechanism[129,153,154] taking place at the dye-oxide interface. Our results suggests that ~50% of the TiO_2 electrode surface is characterized by N3 dyes strongly coupled to the oxide electrode by the bridging or bidentate coordination; these dyes eventually develop into dcbpy moieties upon N3-TiO_2 electrode photodegradation. Note that the nature of the bonding affects the stability; in this respect the ~50% reduction for the fs component upon N3 photodegradation (Figure 4.2a) may indicate that weakly couple dyes decompose into fragments that do not allow for photo-induced ET paths towards the oxide electrode.

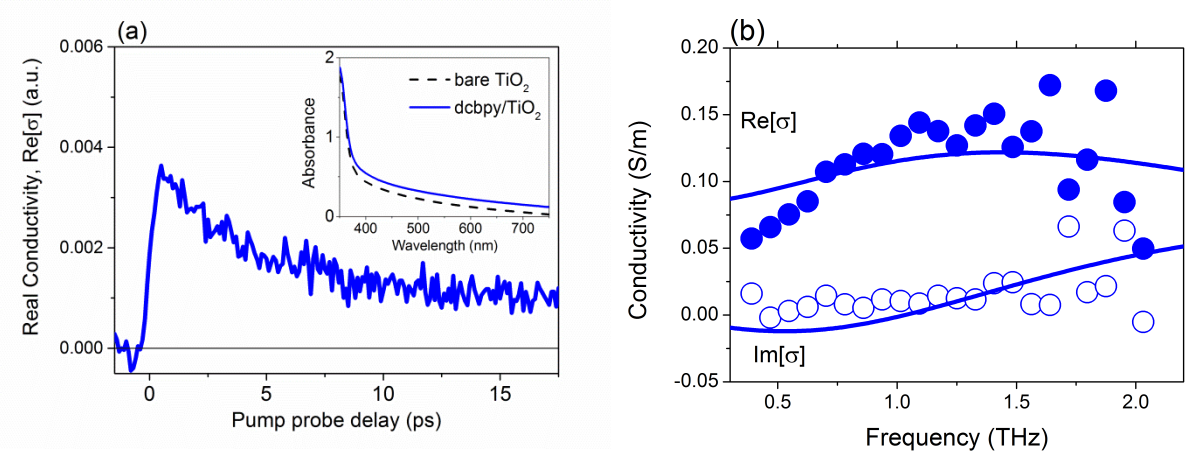

Figure 4.5 (a) Carrier dynamics in dcbpy-TiO_2 monitored by time-resolved terahertz spectroscopy under 400 nm photoexcitation (Inset: Absorbance of dcbpy-TiO_2 and bare TiO_2), (b) Frequency-resolved complex photoconductivity in dcbpy-TiO_2 (after 2 ps, 400 nm photo-excitation); blue solid lines represent Drude-Smith fits.

4.4 Summary

In conclusion, we have investigated the evolution of interfacial electron transfer (ET) upon dye photodegradation in N3 sensitized mesoporous TiO_2 electrodes by time-resolved terahertz spectroscopy (TRTS). Remarkably enough, we observe that, upon complete N3-TiO_2 photodegradation, substantial electron injection into the oxide remains, amounting to ~50% of the pristine system. This remnant ET signal is unambiguously attributed to dcbpy (4,4'- dicarboxylic acid - 2,2'-bipyridine), a photodegradation product of the N3 dye that remains bonded to the TiO_2 electrode.

4.5 Appendix

Extracting and modelling frequency-resolved complex photoconductivity from TRTS measurements.

The frequency-resolved complex photoconductivity of N3-TiO_2 electrode was obtained by Fourier transformation of the time-resolved probe traces transmitted through the films. Frequency-resolved complex photoconductivity $\Delta\sigma(\nu)$ can be expressed as a function of the differential transmissivity $\Delta T(\nu)$ via the following formula:[155]

$$\Delta\sigma(\nu) \propto \frac{n+1}{Z_0 d}\left(\frac{1}{1+\frac{\Delta T(\nu)}{T_0(\nu)}} - 1\right) \qquad (1)$$

where Z_0 = 377 Ω is the impedance of free space, d is the thickness of the films ($d \sim 10$ μm), $T_0(\nu)$ is the transmitted reference THz spectrum and n is the refractive index of the unexcited substrate ($n_{fs} = 1.95$).[120] The frequency-resolved complex photoconductivity spectra of N3-TiO_2 and dcbpy-TiO_2 samples are fitted by using Drude-Smith (DS) model as:

$$\square(\square) = \frac{\square_p^2 \varepsilon_0 \tau}{1 - i\,\square\,\tau} * \left(1 + \sum_{n=1}^{\infty} \frac{c_n}{(1 - i\,\square\,\tau)^n}\right) \qquad (2)$$

where ω_p, ε_0, τ and c_n are the plasma frequency and vacuum permittivity, scattering time and scattering parameter, respectively.

Chapter 5

Correlating Carrier Dynamics and Photocatalytic Hydrogen Generation in Pt Decorated CdSe Tetrapods

We investigate photo-induced carrier dynamics by time resolved terahertz spectroscopy (TRTS) in Pt nanoparticle-decorated CdSe tetrapods as a function of Pt nanoparticles size. We find that the collection efficiency of electrons photo-generated in the tetrapods by the Pt particle increases as a function of Pt nanoparticle size. However, the photocatalytic H_2 generation efficiency is reduced for tetrapods decorated with larger Pt particles. Our results demonstrate a competition between electron capture efficiency at the semiconducting/metal interface, increasing with nanoparticles size, and electron release efficiency at the metal/water interface, decreasing with nanoparticles size. This trade-off defines an optimum for photocatalytic H_2 generation in Pt co-catalyst decorated CdSe tetrapods as a function of Pt size.

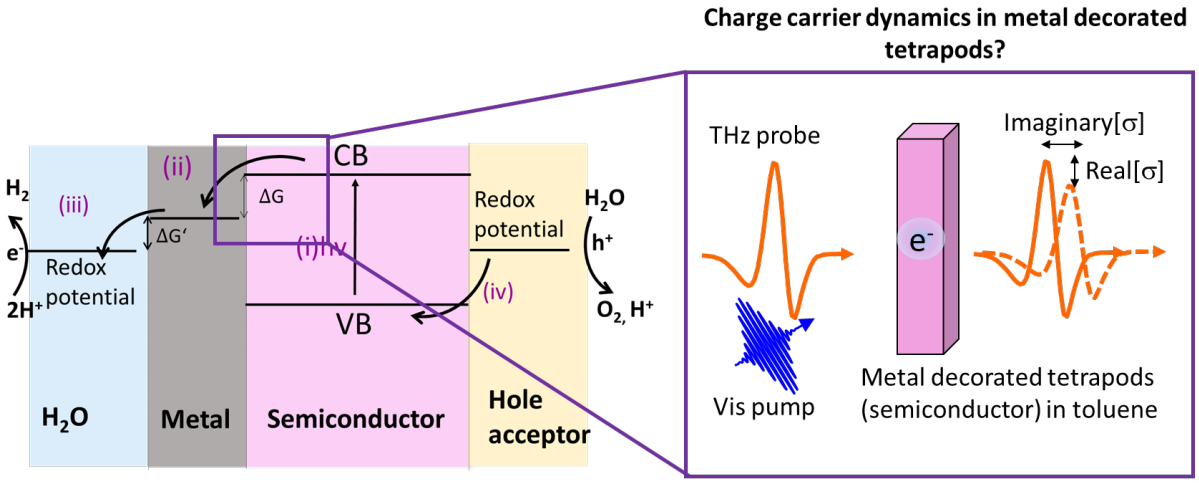

Figure 5.1 Schematic representation of time-resolved spectroscopy (TRTS) experiment in CdSe tetrapods in toluene.

5.1 Introduction and aim of the work

Photocatalysis represents an appealing approach for energy storage in chemical fuels such as hydrogen, methane or methanol.[56,156] Semiconductor nanocrystals constitute a class of building block systems that are promising photocatalysts for H_2 generation owing to the fact that their optical and electronic properties are tunable by size, composition and morphology.[61–66] Wave function engineering in type II band-alignment core/shell QDs,[67,157] dot-in-rod nanorods[64,68] and tetrapods[68,158] architectures allows for fine tuning electron and hole localization within the semiconducting hetero-nanostructures; this aspect has a direct impact on photo-induced charge carrier relaxation within the semiconducting nanostructure and hence on the photocatalytic H_2 generation.[64,67,68] Furthermore, the photocatalytic activity of semiconducting nanostructures can be boosted by decorating them with metal nanoparticles acting as charge scavengers; the so-called co-catalysts.[5,63,64,69] Therefore, controlling the size, composition, coverage and specific location of the metal co-catalyst is an important factor for improving photocatalytic H_2 generation efficiency.[62,70–75]

Specifically, the interplay between metal co-catalyst loading (size and coverage) and the photocatalytic H_2 generation performance for metal decorated nanostructures has been interrogated by several groups.[70–72,75] Berr et al. and Schweinberger et al. have previously reported photocatalytic H_2 generation efficiency in Pt decorated CdS nanorods as a function of metal particle coverage and size (for Pt clusters between 8 atoms and 68 Pt atoms).[71,72] They found that co-catalyst coverage improves photocatalytic H_2 generation efficiency. On the other hand, for a fixed co-catalyst coverage, they reported that an intermediate Pt cluster size among those analyzed (specifically ~1 nm consisting of 46 Pt atoms) provided the best photocatalytic H_2 generation efficiency.[71] Analogously, Ben-Shahar et al.[75] analyzed the effect of gold co-catalyst particle size in gold-tipped CdS rods. While increasing the Au particle size was found to speed up the rates of electron collection at the co-catalyst, an intermediate Au particle size provided the maximum photocatalytic H_2 generation efficiency. All of these previous findings on metal-decorated semiconducting nanorods have been rationalized by assuming the work function of the co-catalyst to be size-dependent, directly affecting interfacial charge transfer rates at both the semiconducting/metal and metal/water interfaces. Similarly, some of us recently reported[70] on the photocatalytic H_2 generation performance of Pt-decorated CdSe tetrapods as a function of co-catalyst size

(with identical coverages and Pt particle diameters in the range of ≤1.5 nm to ~2.5 nm). We found that samples containing the smallest ≤1.5 nm diameter Pt particles provided the highest photocatalytic H_2 generation.[70] Understanding whether metal decorated tetrapods follow similar photo-physics when compared to those reported in nanorods as a function of co-catalyst size requires establishing a clear correlation between co-catalyst Pt sizes, photocatalytic H_2 generation and carrier dynamics.

In this study, we interrogate photo-induced carrier dynamics by Time Resolved Terahertz Spectroscopy (TRTS) in Pt decorated CdSe tetrapods showing reduced H_2 photocatalytic performances as a function of Pt size. From our analysis of the carrier dynamics, we conclude that electron collection efficiency from the semiconducting tetrapod towards the Pt particle improves from ~94% (for small co-catalyst size of Pt ≤1.5 nm) to unity quantum yield for higher loading (size of Pt ~2.5 nm). However, the photocatalytic H_2 generation efficiency of the Pt decorated CdSe tetrapods shows an opposite trend: the samples decorated with ≤1.5 nm sized Pt particles outperform the tetrapods decorated with larger Pt sizes (Pt ~2.5 nm) by ~35-fold. This demonstrates that the collection of photogenerated electrons at the larger Pt particles does not represent a kinetic bottleneck for photocatalytic H_2 generation (where larger Pt co-catalyst particles capture electrons faster than smaller Pt particles). Rather, the recombination of the electron from the Pt particle with the hole in the tetrapod hybrid represents a kinetic bottleneck for larger Pt sizes. This relaxation channel, consistent with a Pt size-dependent work-function, competes with electron release from the Pt particle at the metal/water interface. A change in the work function would explain modified interfacial metal/semiconductor energetics within a Marcus–Gerischer[1,159,160] electron transfer picture. Analogous to the case of metal decorated nanorods,[71,72,75] our results demonstrate that electron capture efficiency at the semiconducting/metal interface and electron release efficiency at the metal/water interface follow competing trends as a function of co-catalyst particle size towards photocatalytic H_2 generation in Pt decorated CdSe tetrapods. This trade-off sets an optimum for photocatalytic H_2 generation as a function of Pt loading.

5.2 Materials and Methods

We introduced experimental details for measuring carrier frequency-resolved complex conductivity dynamics by TRTS and how to extract complex conductivity in Chapter 2.

CdSe tetrapods (with a band gap offset of ~680 nm) were synthesized from CdSe Zinc Blende (ZB) seeds by continuous precursor injection (CPI) method; a detailed description is given elsewhere.[70] In brief, the loading of the Pt nanoparticles decorating primarily the tetrapod arms was controlled by changing the mass of Pt precursor solution from 1 mg to 25 mg that was injected into the reaction solution containing 25 mg CdSe tetrapods. The end products were purified from free Pt nanoparticles by centrifugation and then capped by 11-mercaptoundecanoic acid (MUA) (hole acceptor ligand).[161] These recipes produced a constant Pt particle areal density but different average sizes with diameter of ≤1.5 nm and ~2.5 nm as determined by High Angle Annular Dark Field-Scanning Transmission Electron Microscopy (HAADF-STEM).[70] The resulting Pt-decorated CdSe tetrapods with different Pt nanoparticle sizes were characterized by high-resolution transmission electron microscopy (HR-TEM), revealing large uniformity in the arm/core aspect ratios of 50/5 for each Pt decorated tetrapods (see ref [70]). Furthermore, the HR-TEM analysis revealed CdSe arms consisting of wurtzite (WZ) structure and zinc blende (ZB) tetrapod core.[70] Both HR-TEM images and X-ray diffraction (XRD) analysis confirmed WZ arms, ZB core and face centered cubic (fcc) crystal lattice of Pt nanoparticles.[70] The two distinct crystal structures of ZB core and WZ arms result in quasi type II band structure between core and arms in the CdSe tetrapods.[65,66,162,163]

5.3 Results and Discussions

Figure 5.2 (left) shows transmission electron microscopy (TEM) images of bare CdSe tetrapods, Pt decorated CdSe tetrapods from 1 mg Pt and 25 mg Pt precursor. The tetrapod nanostructures are defined by QD cores of ~5 nm diameter and ~50 nm nanorod arms (Pt coverage, primarily on the arms, amounts to ~20 nanoparticles per arm). Figure 5.2 (right) summarizes the photocatalytic hydrogen generation of the Pt decorated CdSe tetrapods decorated by different sizes of Pt nanoparticles (0 nm: bare CdSe, 1.5 nm: Pt (1 mg)/CdSe and 2.5 nm: Pt (25 mg)/CdSe samples).[70] The photocatalytic hydrogen generation of the Pt

decorated CdSe tetrapods decorated by different sizes of Pt nanoparticles was reported in ref 20. As summarized in Figure 5.2 (right), for the samples analyzed in this work, we found photocatalytic H_2 generation of ~3 $nH_2/\mu molg^{-1}$ for bare CdSe tetrapods, ~250 $nH_2/\mu molg^{-1}$ for ≤1.5 nm Pt decorated CdSe tetrapods and ~7 $nH_2/\mu molg^{-1}$ for ~2.5 nm Pt decorated CdSe tetrapods. Note that the photocatalytic H_2 generation for tetrapods decorated with small ≤1.5 nm Pt clusters represents a ~35-fold increase compared to samples loaded with Pt clusters of ~2.5 nm.

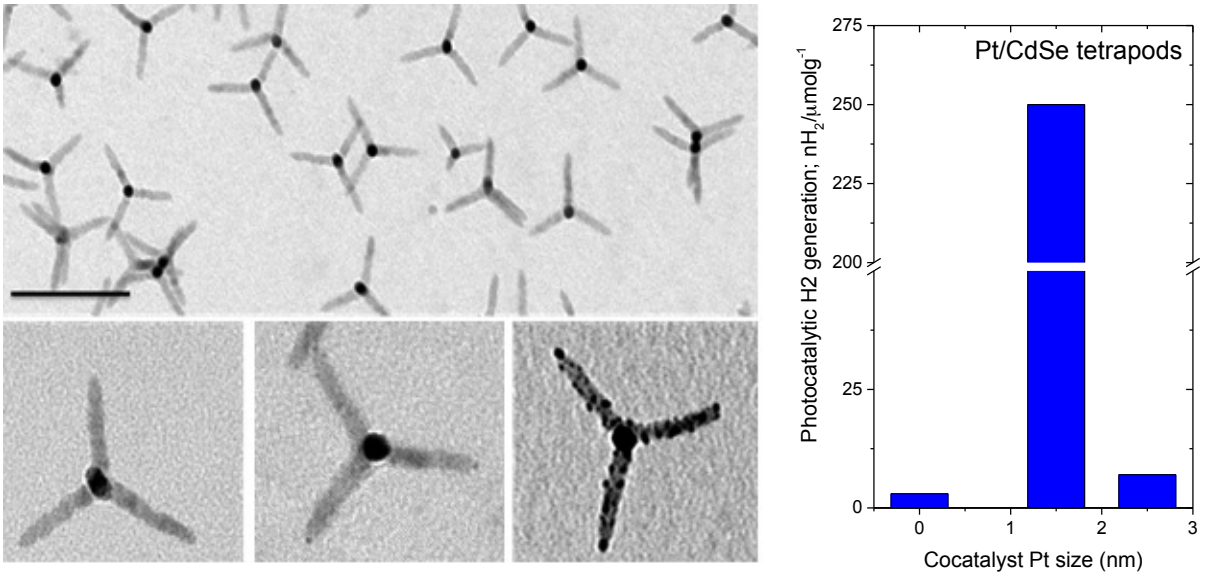

Figure 5.2 (Left upper panel): TEM image of bare CdSe tetrapods (scale bar: 100 nm); (Left bottom panel) TEM bare, ≤ 1.5 nm Pt decorated CdSe and ~2.5 nm Pt decorated CdSe tetrapods. (Right): Photocatalytic hydrogen generation of the Pt decorated CdSe tetrapods versus different sizes of Pt nanoparticles (0 nm: bare CdSe, ≤1.5 nm Pt and 2.5 nm Pt decorated CdSe tetrapods (see ref [70] for further details).

In Figure 5.3, we present the time-dependent real conductivity following photoexcitation measured by TRTS of toluene solutions containing bare tetrapods (red squares) and tetrapods decorated with Pt particles with averaged diameters of ≤1.5 nm and ~2.5 nm (blue and black squares respectively). All the measurements were carried out in the regime of, on average, appreciably less than one electron-hole pair being generated per tetrapod (400 nm pump fluence ~10 $\mu J/cm^2$), and the optical density of the samples at 400 nm was kept the same, allowing for a direct comparison of the photoconductivity amplitudes

measured on different samples. The time-dependent real photoconductivity in bare CdSe tetrapods (Figure 5.3 - red squares) reveals a sub-picosecond rise followed by biphasic decay dynamics with characteristic lifetimes of 1.25 ± 0.05 ps and 500 ± 25 ps. A similar fast component (< 2 ps) has been resolved by transient absorption spectroscopy for CdSe tetrapods and was assigned to localization of electrons from the arm to the core.[162,163] The localization of the electron at the core is a consequence of the type II band alignment between ZB core and WZ arm for CdSe tetrapods,[65,66,70] and is consistent with the frequency resolved THz conductivity of our samples presented below. The long lived TRTS lifetime resolved for bare CdSe tetrapods can be assigned to the lifetime of quasi-free carriers populating tetrapod, $\tau_{\mathrm{e-h,rec}}$ = 500 ± 25 ps.

The blue trace in Figure 5.3 shows the effect of ≤1.5 nm Pt decoration in CdSe tetrapods on the carrier dynamics. The real conductivity signal right after pump is comparable in magnitude to that obtained for bare tetrapods (red trace in Figure 5.3), revealing a similar yield of quasi-free carrier generation. The dynamics are still well modelled by a biphasic decay, where the fast component is assigned as in the case of bare tetrapods to the localization of electrons in the core (with the same lifetime that is observed for the bare tetrapods ($\tau_{\mathrm{e,localization}}$ = 1.25 ± 0.05 ps). The slow component for this sample is characterized by a lifetime of ~30 ps, and associated with the capture of electrons at the ≤1.5 nm Pt particles ($\tau_{\mathrm{tr,e\ Pt}}$). This assignment is consistent with the expected role of the metal co-catalyst as electron scavenger.[63,164] The lifetime of electron capture at the metal Pt particle competes with the exciton recombination lifetime in the tetrapod ($\tau_{\mathrm{e-h,rec}}$ = 500 ± 25 ps); this will co-determine the efficiency of the photocatalytic process as will be discussed later.

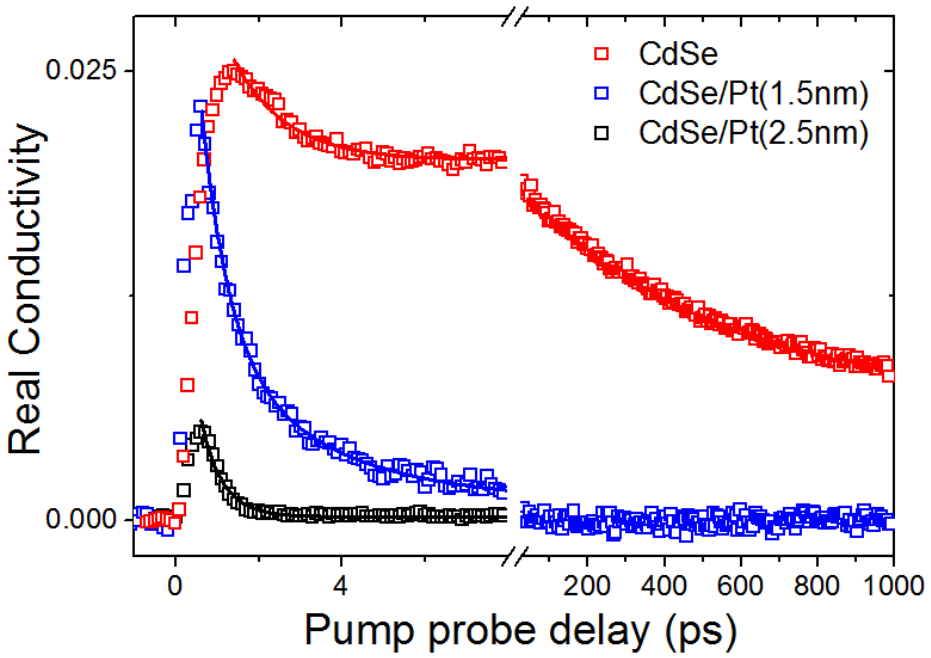

Figure 5.3 Real conductivity (a.u.) versus pump probe delay in CdSe and Pt decorated CdSe tetrapods in toluene. Solid lines show exponential fits providing lifetimes $\tau_{\mathrm{e,localization}}$ = 1.25 ± 0.05 ps and $\tau_{\mathrm{e-h,rec}}$ = 500 ± 25 ps for bare CdSe, $\tau_{\mathrm{e,localization}}$ = 1.30 ± 0.05 ps and $\tau_{\mathrm{tr,e\ Pt}}$= 26.9 ± 4.8 ps for ≤1.5 nm Pt decorated CdSe, and $\tau_{\mathrm{tr,h}}$= 0.53 ± 0.02 for ~2.5 nm Pt decorated CdSe tetrapods.

The decoration of tetrapods with larger Pt co-catalyst sizes (~2.5 nm, black trace in Figure 5.3), reduces the overall amplitude of the real conductivity when compared with bare and 1.5 nm Pt decorated tetrapods. The reduced amplitude indicates that a substantial fraction of electrons populating the tetrapod are captured at the Pt particles faster than our experimental resolution of ~200 fs. The remaining signal is characterized by a lifetime of ~ 0.5 ps (Figure 5.3 - black squares); the nature of this signal is discussed below.

To investigate the nature of the monitored photoconductivity in the samples, we determined the frequency-resolved complex conductivity (( )) of the bare CdSe tetrapods (15 ps after photoexcitation) and of the ~2.5 nm Pt decorated CdSe tetrapods (0.9 ps after photoexcitation), respectively. The spectral response of bare tetrapods shows an increasing positive real conductivity Re[σ] and decreasing negative imaginary conductivity Im[σ] that can be well modelled by phenomenological Drude-Smith model (red traces in Figure 5.4a; see experimental section for fitting details); this response is characteristic for conductivity

mediated by quasi-free carriers experiencing backscattering due to confinement effects.[103] Using Drude-Smith fitting, we infer a backscattering parameter of c = -0.99 ± 0.01 (and scattering time of τ = 20 fs) which refers to the complete backscattering for highly localized charges (e,g, electrons). For ~2.5 nm Pt decorated CdSe tetrapods, fitting of Drude-Smith[103] model to the data provides a value of c = -0.91 ± 0.01 (and scattering time of τ = 27 fs) (black line in Figure 5.4b). Note that, the degree of confinement can be inferred from the *c* parameter as described in the experimental section (with *c* = 0 and *c* = -1 representing a lack and complete backscattering experienced by photogenerated charges, respectively).[76,165] Hence, these numbers imply increased delocalization for the photogenerated free charges in the sample loaded with larger Pt particles. We therefore assign the short-lived component resolved in the pump-probe traces to holes partially delocalized within the 1D tetrapod arms with a lifetime of ~ 0.5 ps (Figure 5.3 - black squares). The localized character of signal attributed to electrons (Drude-Smith model with *c* = -1) and quasi-delocalized nature of probed holes (Drude-Smith model with *c* = -0.92) is consistent with the expected type II band alignment[65,66] induced by the two distinct crystal structures of ZB core and WZ arm in CdSe tetrapods (with electrons localized in the 0D core and holes partially delocalized in the 1D tetrapods arms). Within this scenario, the amplitude of the terahertz signal observed for the bare CdSe tetrapod is determined by the response of both electrons and holes, while that of the ~2.5 nm Pt decorated CdSe sample right after the pump (~0.9 ps pump-probe delay) is determined by holes only. As such, the ratio of the two signals should reflect the effective mass ratio of quasi-free holes versus electrons for CdSe (m_h/m_e). This ratio amounts to ~4, which is within the range of the reported values in the literature for CdSe (m_h/m_e = 3-6),[67,162,166,167] supporting the assignment of the real conductivity signal monitored in 2.5 nm Pt decorated CdSe tetrapods (Figure 5.3 - black squares) being associated with hole dynamics (with a lifetime of $\tau_{\mathrm{tr,h}} = 0.5$ ps).

From our data, we cannot establish the nature of the hole trapping, e.g. a bulk or surface trap and/or eventually capture at the hole acceptor MUA ligands.[164] Trapping of holes in dot-in-rod structures CdSe/CdS[168] and CdSe nanorods[68] has been resolved by transient absorption to occur in ~0.7 ps, and has been tentatively associated with unpassivated traps at the rod surface. The fast trapping of the hole has been suggested to be a kinetic bottleneck for photocatalytic H_2 generation efficiency by other authors.[161,164]

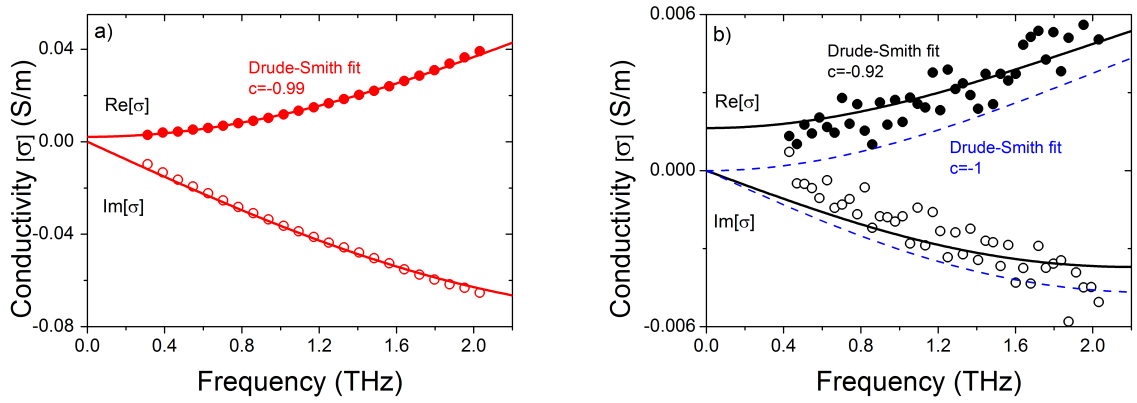

Figure 5.4 a) Frequency-resolved complex-valued photoconductivity for a) bare CdSe tetrapods after 15 ps pump-probe delay, b) ~2.5 nm Pt decorated CdSe tetrapods after 0.9 ps pump-probe delay. Red, black and blue lines represent fits using the Drude-Smith model providing different c parameters as shown.

In Figure 5.5, we summarize our findings of electron and hole dynamics in Pt decorated CdSe tetrapods. The overall photocatalytic H_2 generation efficiency is related to 2 kinetically relevant steps as:[70–72,169] (i) electron capture from CdSe tetrapods to the Pt co-catalyst at CdSe/Pt interface (green line labelled as $k_{\mathrm{tr,e\ Pt}}$ in Figure 5.5), and (ii) electron release from Pt to water at the Pt/water interface (blue line in Figure 5.5; k_{H2}). In this respect, the overall photocatalytic H_2 generation efficiency (η_{H2}) measured in the Pt decorated tetrapods can be defined as:

$$\eta_{\mathrm{H2}} = \eta_{\mathrm{CdSe\rightarrow Pt}} * \eta_{\mathrm{Pt\rightarrow H2O}} = \{k_{\mathrm{tr,e\ Pt}}/(k_{\mathrm{tr,e\ Pt}} + k_{e-h,rec})\} * \{k_{\mathrm{H2}}/(k_{\mathrm{H2}} + k_{\mathrm{tr,e-h}})\} \quad (1)$$

where $k_{\mathrm{tr,e\ Pt}}$ and $k_{e-h,rec}$ are, respectively, the competing rates of electron trapping at Pt co-catalyst and exciton lifetime in the tetrapod (defining the electron capture efficiency at the Pt particle $\eta_{\mathrm{CdSe\rightarrow Pt}}$); and k_{H2} and $k_{\mathrm{tr,e-h}}$ are the rate of electron release from the Pt to water and competing relaxation back to the tetrapod (defining the electron release efficiency from the Pt particle; $\eta_{\mathrm{CdSe\rightarrow Pt}}$). From Equation 1 and the inferred TRTS rates, the electron capture efficiency at the Pt particle for the ≤1.5 nm Pt decorated CdSe tetrapods is estimated to be $\eta_{\mathrm{Cdse\rightarrow Pt}}$ ~94%; meaning that 94 out of 100 photogenerated electrons are

efficiently collected at the Pt co-catalyst. The electron capture efficiency for the sample containing larger Pt particles (~2.5 nm) reaches unity quantum efficiency; $\eta_{\mathrm{Cdse}\rightarrow\mathrm{Pt}}$ ~100%. The faster collection of electrons revealed in tetrapods decorated with larger Pt particles (blue vs black trace in Figure 5.3) is consistent with previous reports,[75] and might be directly related (for a fixed Pt particle areal density) to an increase in capture cross section (associated with donor-acceptor coupling) and/or with an increase in the excess free Gibbs energy between tetrapod LUMO and Pt Fermi level according to Marcus–Gerischer electron transfer reactions.[1,159,160]

As mentioned above, for the samples analyzed in this work, we found that photocatalytic H_2 generation (η_{H2} in Equation 1) was ~7 $nH_2/\mu molg^{-1}$ for ~2.5 nm Pt decorated CdSe tetrapods and ~250 $nH_2/\mu molg^{-1}$ for ≤1.5 nm Pt decorated CdSe tetrapods (see Figure 5.2 -right).[70] Given that the maximum photocatalytic H_2 generation is observed for 1.5 nm Pt decorated CdSe tetrapods (see Figure 5.2 -right), and according to the trend in $\eta_{\mathrm{Cdse}\rightarrow\mathrm{Pt}}$ vs Pt size, we have to conclude that the second term in Equation 1 ($\eta_{\mathrm{Pt}\rightarrow\mathrm{H2O}} = \{k_{\mathrm{H2}}/(k_{\mathrm{H2}} + k_{\mathrm{tr,e-h}})\}$) is necessarily larger for small Pt nanoparticles. Our findings thus indicate that, while electron capture at the Pt ($k_{\mathrm{tr,e\ Pt}}$) will be favored in larger Pt particles, the electron release rate from the Pt co-catalyst to water (k_{H2}) is reduced as Pt particles become larger. This trade-off sets an optimum for photocatalytic H_2 generation as a function of Pt loading, as the two kinetically relevant steps for electrons at semiconductor/metal and at metal/water interfaces follow opposite trends as a function of the Pt co-catalyst size, analogous to what has previously been concluded for gold-tipped CdS nanorods[75]. Our findings are consistent with the Marcus–Gerischer theory[1,159,160] where increasing the driving force for charge transfer between tetrapod LUMO and Pt Fermi level (ΔG in Figure 5.5) would increase the $k_{\mathrm{tr,e\ Pt}}$ rate but at the same time reduce the k_{H2} rate in proportion, thereby establishing a trade-off for the photocatalytic H_2 generation as a function of Pt size.

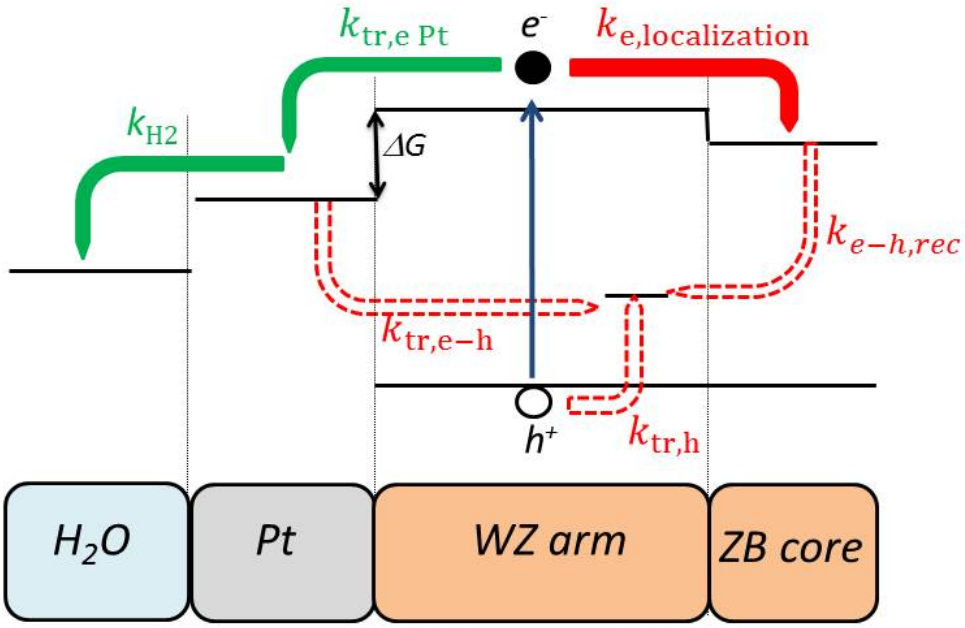

Figure 5.5 Summary for carrier dynamics taking place in Pt decorated CdSe tetrapods showing rates of electron trapping at Pt co-catalyst ($k_{\mathrm{tr,e\ Pt}}$), localization of quasi-free electrons from wurtzite arms (WZ) towards zinc blende core (ZB) ($k_{\mathrm{e,localization}}$), hole trapping ($k_{\mathrm{tr,h}}$), electron-hole recombination in tetrapod ($k_{\mathrm{e-h,rec}}$) and electron-hole recombination from Pt to the tetrapod ($k_{\mathrm{tr,e-h}}$).

5.4 Summary

The interplay between carrier dynamics and photocatalytic H_2 generation was analyzed in Pt decorated CdSe tetrapods as a function of Pt co-catalyst size. Our results demonstrate that a trade-off exist as a function of Pt size between the two kinetically relevant steps involved in photocatalytic H_2 generation; (1) electron transfer from the tetrapods towards the Pt particle increases as a function of Pt co-catalyst size and (2) electron capture from the metal towards water reduces as a function of Pt co-catalyst size. This trade-off set an optimum Pt co-catalyst size for obtaining maximized photocatalytic H_2 generation in metal decorated CdSe tetrapods.

Chapter 6

Conclusions and outlook

Solar energy provides promising solutions for today's world energy needs. We can directly convert solar energy into electricity via solar cells and store solar enegy into chemical energy via water splitting in environmental friendly schemes. However, photovoltaics and photocatalysis still represent a small percentage of the global energy production, that is dominated by non-renewable energy sources. This is partly due to the fact that the current solar energy conversion technologies are still costly with respect to the non-renewable energy sources.

In this thesis, we examine the optical and electronic properties of potential active hybrid materials for solar conversion energy processes by using time-resolved terahertz spectroscopy (TRTS). This contact free technique provides us to investigate charge carrier dynamics in terms of charge transport mechanisms in active materials and charge transfer dynamics at interfaces via pump-probe experiments. In these experiements, we photoexcite our samples by ultrashort laser pulse to generate charges (electron and hole) and probe those charges by a freely propagating single cycle THz pulse in the time domain. The time evolution of the carriers (carrier dynamics) can be obtained by conducting a pump-probe experiment where we change the delay between pump and probe, and simultaneously record the photo-induced change on the maxima of the THz pulse. Also, we can monitor the photo-induced complex conductivity spectra of materials in the THz frequency domain by conducting a pump-probe experiment where we change the delay of sampling beam, and simultaneously recording the photoinduced change of the THz probe profile. From these measurements, we can estimate the mobility and the scattering time of the photogenerated charge carriers. TRTS characterization is then able to provide a detailed picture of charge transport in active materials for solar energy conversion. In this thesis, we studied several hybrid systems:

In chapter 3, we employed TRTS technique to investigate the nature of photogenerated charge carriers and their charge transport mechanism in solution processed

$MAPbI_3(Cl)$ perovskite films. We find that photo-generated carriers do not experience localization or preferential backscattering at grain boundaries in our samples in line with a Drude model conductivity response in our samples (free carriers). Finally, we showed that the momentum scattering time versus temperature for the tetragonal phase (displaying room temperature mobilities of μ ~30 $cm^2 V^{-1} s^{-1}$) follows a $T^{-3/2}$ dependence, indicating that acoustic phonon scattering represent the upper limit mechanism impeding larger mobilities in these technologically relevant materials.

In chapter 4, we monitor the evolution of interfacial charge transfer upon photodegradation of molecular dye in N3 sensitized mesoporous TiO_2 electrodes by time-resolved terahertz spectroscopy (TRTS). We showed that sub-ps electron transfer, weighting 50% of the ET from N3 dye towards TiO_2, emerges upon sample's photodegradation. This transfer path is associated with dcbpy (4,4'-dicarboxy-2,2'-bipyridine) moieties remaining bonded to the oxide electrode upon photodegration. We demonstrate that dcbpy provides a direct sub-ps electron transfer when sensitizing TiO_2.

In Chapter 5, we studied the correlation between charge carrier dynamics and photocatalytic hydrogen generation in Pt decorated CdSe tetrapods as a function of Pt co-catalyst size. We demonstrated the presence of a trade-off as a function of Pt size between the electron transfer at the tetrapod / Pt particle interface and electron capture from the metal at Pt / water interface. We find that electron transfer from tetrapod towards Pt particle increases as a function of Pt size, while electron capture from the Pt particle to water decreases as a function of Pt size. This trade-off set an optimum Pt co-catalyst size for obtaining maximized photocatalytic H_2 generation in metal decorated CdSe tetrapods.

Besides the development of new active materials for solar energy conversion architectures, further research is still needed to improve their mobilities, device performances and long-term stabilities. To start with, solution processed perovskites have shown promising solar cell efficiencies (20.1 % according to NREL efficiency chart); however, their mobilities are actually not as high as inorganic semiconductors which are absorbers in commercial high efficiency solar cells. Many types of solution processed perovskites have stability issues; hence resulting in stability problems within their devices and device lifetimes. Additionally, current-voltage characterizations of perovskite-based solar cells suffer from hysteresis effects in devices. Another issue is that commonly studied solution

processed perovskites contain toxic lead which needs to be replaced with its non-toxic counterparts. Therefore, it is highly crucial to further investigate, understand and eventually engineer the perovskite-based solar cells for further improvement of their performances.

Like perovskite based solar cells, dye sensitized solar cells (DSSCs) are one of the emerging PV technologies. They are inspired by the principle of natural photosynthesis which are low cost alternatives for inorganic based solar cells. Although these device architectures have found niche applications in the market, the current device performances of ~12% are not competitive enough for market mass penetration. Further research can be focused on developing new sensitizers matching better the spectrum of sunlight (vis-IR-near IR spectral region). The mesoporous oxide nanostructures also need further characterization in order to be better understood in terms of the role of surface traps to eliminate the interfacial charge recombination proccesses. Furthermore, the lifetimes of devices, especially considering the fact that most dyes are prone to degradation, need to be further increased for the future commertializaition of DSSCs.

To produce hydrogen via sunlight driven by water splitting, many design principles of photocatalytic cells have been developed. Controlling the shape of these nanomaterials is still a major ongoing research topic in order to gain control on charge carrier dynamics at the nanoscale via wavefunction engineeering. But, many challeges are still present in this field, such as chemical stability of these nanostructures in aqueous solutions; non-oxide semiconductors (as the CdSe tetrapod samples analyzed in this thesis) are prone to photocorrosion because they are easily oxidized by photo-generated holes. This process can be prevented or at least substantially reduced by removing the holes from the semiconductor faster than oxidation takes place; this can be attempeted via sacrifial agents. Moreover, the specific morphology and chemistry of hybrid nanostructures needs to be further optimized to improve electron collection at the co-catalyst while preventing detrimental recombination processes. Furthermore, the kinetic competition between H_2 generation and capture at the co-catalyst needs to be fine tuned in order to improve their solar to hydrogen conversion efficiencies.

In conlusion, solar energy conversion processes for energy production and storage are expected to contribute to a better future owing to their renewable nature, low costs and eventually high conversion efficiencies. Although the challenges are huge, further research

and fundamental understanding will promote further developments and open new doors for future technologies.

Acknowledgements

BIBLIOGRAPHY

1. Osterloh, F. E. Inorganic nanostructures for photoelectrochemical and photocatalytic water splitting. *Chem. Soc. Rev.* **42,** 2294–2320 (2013).

2. Green, M. A. Improved value for the silicon free exciton binding energy. *AIP Advances* **3,** 112104–1 (2013).

3. Shockley, W. & Queisser, H. J. Detailed balance limit of efficiency of p-n junction solar cells. *J. Appl. Phys.* **32,** 510–519 (1961).

4. Bolton, J. R., Strickler, S. J. & Connolly, J. S. Limiting and realizable efficiencies of solar photolysis of water. *Nature* **316,** 495–500 (1985).

5. Li, J. & Wu, N. Semiconductor-based photocatalysts and photoelectrochemical cells for solar fuel generation: a review. *Catal. Sci. Technol.* **5,** 1360–1384 (2015).

6. Park, N.-G., Grätzel, M. & Tsutomu, M. *Organic- Inorganic Halide Perovskite Photovoltaics*. (Springer, 2016). doi:10.1007/978-3-319-35114-8

7. Kojima, A., Teshima, K., Shirai, Y. & Miyasaka, T. Organometal halide perovskites as visible-light sensitizers for photovoltaic cells. *J. Am. Chem. Soc* **131,** 6050–6051 (2009).

8. Im, J.-H., Lee, C.-R., Lee, J.-W., Park, S.-W. & Park, N.-G. 6.5% Efficient Perovskite Quantum-Dot-Sensitized Solar Cell. *Nanoscale* **3,** 4088 (2011).

9. Lee, M. M., Teuscher, J., Miyasaka, T., Murakami, T. N. & Snaith, H. J. Efficient hybrid solar cells based on meso-superstructured organometal halide perovskites. *Science* **338,** 643–7 (2012).

10. Mei, A. *et al.* A hole conductor free, fully printable mesoscopic perovskite solar cell with high stability. *Science* **345,** 295–297 (2016).

11. Li, F. *et al.* Ambipolar solution-processed hybrid perovskite phototransistors. *Nat. Commun.* **6,** 8238 (2015).

12. Mei, Y., Zhang, C., Vardeny, Z. V. & Jurchescu, O. D. Electrostatic gating of hybrid halide perovskite field-effect transistors: balanced ambipolar transport at room-

temperature. *MRS Communications* **5,** 297–301 (2015).

13. Grätzel, M. The light and shade of perovskite solar cells. *Nat. Mater.* **13,** 838–842 (2014).

14. Sheng, C. *et al.* Exciton versus Free Carrier Photogeneration in Organometal Trihalide Perovskites Probed by Broadband Ultrafast Polarization Memory Dynamics. *Phys. Rev. Lett.* **114,** 1–5 (2015).

15. Yamada, Y., Nakamura, T., Endo, M., Wakamiya, A. & Kanemitsu, Y. Photocarrier Recombination Dynamics in Perovskite CH3NH3PbI3 for Solar Cell Applications. *J. Am. Chem. Soc* **136,** 11610−11613 (2014).

16. Edri, E. *et al.* Why Lead Methylammonium Tri-Iodide Perovskite-Based Solar Cells Require a Mesoporous Electron Transporting Scaffold (but Not Necessarily a Hole Conductor). *Nano Lett.* **14,** 1000–1004 (2014).

17. Edri, E. *et al.* Elucidating the charge carrier separation and working mechanism of CH3NH3PbI3-xClx perovskite solar cells. *Nat. Commun.* **5,** 3461 (2014).

18. Green, M. A., Ho-Baillie, A. & Snaith, H. J. The emergence of perovskite solar cells. *Nat. Photonics* **8,** 506–514 (2014).

19. Etgar, L. in *Hole Conductor Free Perovskite-based Solar Cells* (ed. Etgar, L.) 2–3 (SpringerBriefs in Applied Sciences and Technology, 2016). doi:10.1007/978-3-319-32991-8

20. Wehrenfennig, C., Liu, M., Snaith, H. J., Johnston, M. B. & Herz, L. M. Charge-carrier dynamics in vapour-deposited films of the organolead halide perovskite CH3NH3PbI3−xClx. *Energy Environ. Sci.* **7,** 2269–2275 (2014).

21. Ponseca, C. S. *et al.* Organometal Halide Perovskite Solar Cell Materials Rationalized: Ultrafast Charge Generation, High and Microsecond-Long Balanced Mobilities, and Slow Recombination. *J. Am. Chem. Soc* **136,** 5189–5192 (2014).

22. Stranks, S. D. *et al.* Electron-hole diffusion lengths exceeding 1 micrometer in an organometal trihalide perovskite absorber. *Science (New York, N.Y.)* **342,** 341–344 (2013).

23. Xing, G. *et al.* Long-range balanced electron- and hole-transport lengths in organic-inorganic CH 3NH3PbI3. *Science* **342,** 344–347 (2013).

24. Brenner, T. M. *et al.* Are Mobilities in Hybrid Organic-Inorganic Halide Perovskites Actually ' High '? *J. Phys. Chem. Lett.* **6,** 4754–4757 (2015).

25. D'Innocenzo, V. *et al.* Excitons versus free charges in organo-lead tri-halide perovskites. *Nat. Commun.* **5,** 3586–3591 (2014).

26. Liu, M., Johnston, M. B. & Snaith, H. J. Efficient planar heterojunction perovskite solar cells by vapour deposition. *Nature* **501,** 395–398 (2013).

27. Etgar, L. *et al.* Mesoscopic CH3NH3PbI3 /TiO2 Heterojunction Solar Cells. *J. Am. Chem. Soc.* **134,** 17396−17399 (2012).

28. Selinsky, R. S., Ding, Q., Faber, M. S., Wright, J. C. & Jin, S. Quantum dot nanoscale heterostructures for solar energy conversion. *Chem. Soc. Rev.* **42,** 2963–85 (2013).

29. Beaujuge, P. M. & Fréchet, J. M. J. Molecular design and ordering effects in pi-functional materials for transistor and solar cell applications. *J. Am. Chem. Soc* **133,** 20009–20029 (2011).

30. Sirringhaus, H. Device physics of solution-processed organic field-effect transistors. *Adv. Funct. Mater.* **17,** 2411–2425 (2005).

31. Giorgi, G., Fujisawa, J., Segawa, H. & Yamashita, K. Small Photocarrier Effective Masses Featuring Ambipolar Transport in Methylammonium Lead Iodide Perovskite: A Density Functional Analysis. *J. Phys. Chem. Lett.* **4,** 4213−4216 (2013).

32. Milot, R. L., Eperon, G. E., Snaith, H. J., Johnston, M. B. & Herz, L. M. Temperature-Dependent Charge-Carrier Dynamics in CH3NH3PbI3 Perovskite Thin Films. *Adv. Funct. Mater.* **25,** 6218–6227 (2015).

33. Wehrenfennig, C., Eperon, G. E., Johnston, M. B., Snaith, H. J. & Herz, L. M. High Charge Carrier Mobilities and Lifetimes in Organolead Trihalide Perovskites. *Adv. Mater.* **26,** 1584–1589 (2014).

34. Stoumpos, C. C., Malliakas, C. D. & Kanatzidis, M. G. Semiconducting tin and lead

iodide perovskites with organic cations: Phase transitions, high mobilities, and near-infrared photoluminescent properties. *Inorg. Chem.* **52,** 9019–9038 (2013).

35. O'Regan, B. & Grätzel, M. A low-cost, high-efficiency solar cell based on dye-sensitized colloidal TiO2 films. *Nature* **353,** 737–740 (1991).

36. Yu, Z., Li, F. & Sun, L. Recent advances in dye-sensitized photoelectrochemical cells for solar hydrogen production based on molecular components. *Energy Environ. Sci.* **8,** 760–775 (2015).

37. Green, M. A., Emery, K., Hishikawa, Y., Warta, W. & Dunlop, E. D. Solar cell efficiency tables (Version 45). *Prog. Photovolt: Res. Appl.* **23,** 1–9 (2015).

38. Okada, K., Matsui, H., Kawashima, T., Ezure, T. & Tanabe, N. 100 mm x 100 mm Large-Sized Dye Sensitized Solar Cells. *Journal of Photochemistry and Photobiology A: Chemistry* **164,** 193–198 (2004).

39. Bach, U., Kruger, J. & Grätzel, M. in *Device Concepts in Organic Photovoltaics* (ed. Kafafi, Z. H.) **4108,** 1–7 (Proc. SPIE, 2001).

40. Kroon, Jan and Hinsch, A. in *Organic Photovoltaics* (ed. Brabec, C. J.) 273–290 (2003).

41. Grätzel, M. Solar energy conversion by dye-sensitized photovoltaic cells. *Inorganic chemistry* **44,** 6841–51 (2005).

42. Grätzel, M. Dye-sensitized solar cells. *Journal of Photochemistry and Photobiology C: Photochemistry Reviews* **4,** 145–153 (2003).

43. Hara, K. Molecular design of sensitizers for dye-sensitized solar cells. *Springer Series in Materials Science* **111,** 217–250 (2009).

44. Balzani, V., Barigelletti, F. & De Cola, L. *Metal complexes as light absorption and light emission sensitizers*. *Topics in Current Chemistry* **158,** (1990).

45. Listorti, A., Regan, B. O. & Durrant, J. R. Electron Transfer Dynamics in Dye-Sensitized Solar Cells. *Chem. Mater.* **23,** 3381–3399 (2011).

46. Grätzel, M. Conversion of sunlight to electric power by nanocrystalline dye-sensitized solar cells. *Journal of Photochemistry and Photobiology A: Chemistry* **164,** 3–14 (2004).

47. Furube, A. *et al.* Ultrafast stepwise electron injection from photoexcited Ru-complex into nanocrystalline ZnO film via intermediates at the surface. *J. Phys. Chem. B* **107,** 4162–4166 (2003).

48. Marcus, R. A. Electron transfer reactions in chemistry. Theory and experiment. *Rev. Mod. Phys.* **65,** 599–610 (1993).

49. Ardo, S. & Meyer, G. J. Photodriven heterogeneous charge transfer with transition-metal compounds anchored to TiO2 semiconductor surfaces. *Chem. Soc. Rev.* **38,** 115–164 (2009).

50. Duncan, W. R. & Prezhdo, O. V. Theoretical studies of photoinduced electron transfer in dye-sensitized TiO2. *Annu. Rev. Phys. Chem.* **58,** 143–184 (2007).

51. Ai, X., Anderson, N. a, Guo, J. & Lian, T. Electron injection dynamics of Ru polypyridyl complexes on SnO2 nanocrystalline thin films. *J. Phys. Chem. B* **109,** 7088–7094 (2005).

52. Asbury, J. B. *et al.* Femtosecond IR study of excited-state relaxation and electron-injection dynamics of Ru(dcbpy)2(NCS)2 in solution and on nanocrystalline TiO2 and Al2O3 thin films. *J. Phys. Chem. B* **103,** 3110–3119 (1999).

53. Agrell, H. G., Lindgren, J. & Hagfeldt, A. Degradation mechanisms in a dye-sensitized solar cell studied by UV-VIS and IR spectroscopy. *Sol. Energy* **75,** 169–180 (2003).

54. Ke, L. *et al.* Degradation mechanism of ZnO-based dye-sensitized solar cells. *Solar Energy Materials Solar Energy* **94,** 323–326 (2010).

55. Grünwald, R. & Tributsch, H. Mechanisms of Instability in Ru-Based Dye Sensitization Solar Cells. *J. Phys. Chem. B* **101,** 2564–2575 (1997).

56. Fujishima, A. & Honda, K. TiO2 photoelectrochemistry and photocatalysis. *Nature* **213,** 8656 (1972).

57. Inoue, T., Fujishima, A., Konishi, S. & Honda, K. Photoelectrocatalytic reduction of carbon dioxide in aqueous suspensions of semiconductor powders. *Nature* **277,** 637–638 (1979).

58. Linsebigler, A. L., Lu, G. & John T. Yates, J. Photocatalysis on TiO2 Surfaces: Principles, Mechanisms, and Selected Results. *Chem. Rev.* **95,** 735–758 (1995).

59. Jafari, T. *et al.* Photocatalytic Water Splitting—The Untamed Dream: A Review of Recent Advances. *Molecules* **21,** 900 (2016).

60. Hoffmann, M. R., Martin, S., Choi, W. & Bahnemannt, D. W. Environmental Applications of Semiconductor Photocatalysis. *Chem. Rev.* **95,** 69–96 (1995).

61. Berr, M. J. *et al.* Delayed photoelectron transfer in Pt-decorated CdS nanorods under hydrogen generation conditions. *Small* **8,** 291–297 (2012).

62. Bang, J. U., Lee, S. J., Jang, J. S., Choi, W. & Song, H. Geometric Effect of Single or Double Metal-Tipped CdSe Nanorods on Photocatalytic H2 Generation. *J. Phys. Chem. Lett.* **3,** 3781–3785 (2012).

63. Berr, M. *et al.* Colloidal CdS nanorods decorated with subnanometer sized Pt clusters for photocatalytic hydrogen generation. *Appl. Phys. Lett.* **97,** 93108 (2010).

64. Amirav, L. & Alivisatos, A. P. Photocatalytic hydrogen production with tunable nanorod heterostructures. *J. Phys. Chem. Lett.* **1,** 1051–1054 (2010).

65. Li, J. & Wang, L. W. Shape effects on electronic states of nanocrystals. *Nano Lett.* **3,** 1357–1363 (2003).

66. Wei, S.-H. & Zhang, S. B. Structure stability and carrier localization in Cd X (X = S , Se , Te) semiconductors. *Phys. Rev. B* **62,** 6944–6947 (2000).

67. Zhu, H., Song, N., Rodr, W. & Lian, T. Wave Function Engineering for Efficient Extraction of up to Nineteen Electrons from One CdSe/CdS Quasi-Type II Quantum Dot. *J. Am. Chem. Soc* **134,** 4250–4257 (2012).

68. Yang, Y. *et al.* Direct Observation of Photoexcited Hole Localization in CdSe Nanorods. *ACS Energy Letters* **1,** 76–81 (2016).

69. Vaneski, A. *et al.* Hybrid colloidal heterostructures of anisotropic semiconductor nanocrystals decorated with noble metals: Synthesis and function. *Adv. Funct. Mater.* **21,** 1547–1556 (2011).

70. Sung, Y. *et al.* Uniform decoration of Pt nanoparticles on well-defined CdSe tetrapods and the effect of their Pt cluster size on photocatalytic H2 generation. *CrystEngComm* **17,** 8423–8427 (2015).

71. Maximilian J. Berr, Florian F. Schweinberger, Markus Döblinger, Kai E. Sanwald, Christian Wolff, Johannes Breimeier, Andrew S. Crampton, Claron J. Ridge, Martin Tschurl, Ulrich Heiz, Frank Jäckel, and J. F. Size-Selected Subnanometer Cluster Catalysts on Semiconductor Nanocrystal Films for Atomic Scale Insight into Photocatalysis. *Nano Lett.* **12,** 5903–5906 (2012).

72. Schweinberger, F. F. *et al.* Cluster Size Effects in the Photocatalytic Hydrogen Evolution Reaction. *J. Am. Chem. Soc* **135,** 13262−13265 (2013).

73. Nakibli, Y., Kalisman, P. & Amirav, L. Less Is More: The Case of Metal Cocatalysts. *J. Phys. Chem. Lett.* **6,** 2265–2268 (2015).

74. Simon, T., Carlson, M. T., Stolarczyk, J. K. & Feldmann, J. Electron Transfer Rate vs Recombination Losses in Photocatalytic H 2 Generation on Pt-Decorated CdS Nanorods. *ACS Energy Lett.* **1,** 1137–1142 (2016).

75. Ben-Shahar, Y. *et al.* Optimal metal domain size for photocatalysis with hybrid semiconductor-metal nanorods. *Nat. Commun.* **7,** 10413 (2016).

76. Ulbricht, R., Hendry, E., Shan, J., Heinz, T. F. & Bonn, M. Carrier dynamics in semiconductors studied with time-resolved terahertz spectroscopy. *Rev. Mod. Phys.* **83,** 543–586 (2011).

77. Jensen, S. A. *Charge carrier dynamics in photovoltaic materials. PhD thesis, University of Amsterdam*. (2014).

78. Rice, A. *et al.* Terahertz optical rectification from 〈110〉 zinc-blende crystals. *Applied Physics Letters* **64,** 1324–1326 (1994).

79. Exter, V., Martin, F. C. & Grischkowsky, D. THz time domain spectroscopy of water vapor. *Optic Letters* **14,** 1128–1130 (1989).

80. Wu, Q. & Zhang, X. C. Free-space electro-optics sampling of mid-infrared pulses. *Appl.*

Phys. Lett. **71,** 1285–1286 (1997).

81. Planken, P. C. M., Nienhuys, H.-K., Bakker, H. J. & Wenckebach, T. Measurement and calculation of the orientation dependence of terahertz pulse detection in ZnTe. *Journal of the Optical Society of America B* **18,** 313–317 (2001).

82. Schmuttenmaer, C. A. Exploring dynamics in the far infrared with terahertz spectroscopy. *Chem. Rev.* **104,** 1759–1780 (2004).

83. Kužel, P., Kadlec, F. & Němec, H. Propagation of terahertz pulses in photoexcited media: Analytical theory for layered systems. *J. Chem. Phys.* **127,** 24506-1–11 (2007).

84. Hendry, E., Wang, F., Shan, J., Heinz, T. & Bonn, M. Electron transport in TiO2 probed by THz time-domain spectroscopy. *Phys. Rev. [Sect.] B* **69,** 81101 (2004).

85. Beard, M. C., Turner, G. M. & Schmuttenmaer, C. A. Transient photoconductivity in GaAs as measured by time-resolved terahertz spectroscopy. *Phys. Rev. B* **62,** 15764–15776 (2000).

86. Tiwana, P., Docampo, P., Johnston, M. B., Snaith, H. J. & Herz, L. M. Electron Mobility and Injection Dynamics in Mesoporous ZnO, SnO2, and TiO2 Films Used in Dye-Sensitized Solar Cells. *ACS Nano* **5,** 5158–5166 (2011).

87. Pijpers, J. J. H., Ulbricht, R., Derossi, S., Reek, J. N. H. & Bonn, M. Picosecond electron injection dynamics in dye-sensitized oxides in the presence of electrolyte. *J. Phys. Chem. C* **115,** 2578–2584 (2011).

88. Canovas, E. *et al.* Size dependent electron transfer from PbSe quantum dots to SnO2 monitored by picosecond Terahertz spectroscopy. *Nano Lett.* **11,** 5234–5239 (2011).

89. Wang, H., McNellis, E. R., Kinge, S., Bonn, M. & Cánovas, E. Tuning electron transfer rates through molecular bridges in quantum dot sensitized oxides. *Nano Lett.* **13,** 5311–5315 (2013).

90. Yu, P. Y. & Cardona, M. *Fundamentals of Semiconductors*. *Springer Berlin Heidelberg New York* **Third, Rev,** (Springer Berlin Heidelberg New York, 2010).

91. Takeda, Y. & Pearsall, T. Failure of Matthiessen's Rule in the Calculation of Carrier

Mobility and Alloy Scattering. *Electronics Letters* **17,** 1980–1981 (1981).

92. Noh, J. H., Im, S. H., Heo, J. H., Mandal, T. N. & Seok, S. Chemical management for colorful, efficient, and stable inorganic-organic hybrid nanostructured solar cells. *Nano letters* **13,** 1764–1769 (2013).

93. Ball, J. M., Lee, M. M., Hey, A. & Snaith, H. J. Low-temperature processed meso-superstructured to thin-film perovskite solar cells. *Energy Environ. Sci.* **6,** 1739–1743 (2013).

94. Wehrenfennig, C. & Liu, M. Homogeneous Emission Line Broadening in the Organo Lead Halide Perovskite CH3NH3PbI3–x Cl x. *J. Phys. Chem. Lett.* **5,** 1300–1306 (2014).

95. Baumann, A. *et al.* Persistent photovoltage in methylammonium lead iodide perovskite solar cells. *APL Mater.* **2,** 81501 (2014).

96. Baikie, T. *et al.* Synthesis and crystal chemistry of the hybrid perovskite (CH3NH3)PbI3 for solid-state sensitised solar cell applications. *J. Mater. Chem. A* **1,** 5628–5641 (2013).

97. Poglitsch, A. & Weber, D. Dynamic disorder in methylammoniumtrihalogenoplumbates (II) observed by millimeter-wave spectroscopy. *J. Chem. Phys.* **87,** 6373–6378 (1987).

98. Wu, X. *et al.* Trap States in Lead Iodide Perovskites. *J. Am. Chem. Soc* **137,** 2089–2096 (2015).

99. Wehrenfennig, C., Liu, M., Snaith, H. J., Johnston, M. B. & Herz, L. M. Charge carrier recombination channels in the low-temperature phase of organic-inorganic lead halide perovskite thin films. *APL Materials* **2,** 81513 (2014).

100. Ma, J. & Wang, L. Nanoscale Charge Localization Induced by Random Orientations of Organic Molecules in Hybrid Perovskite CH3NH3PbI3. *Nano Lett.* **15,** 248–253 (2015).

101. Savenije, T. J. *et al.* Thermally activated exciton dissociation and recombination control the carrier dynamics in organometal halide perovskite. *J. Phys. Chem. Lett.* **5,** 2189–2194 (2014).

102. Manser, J. S. & Kamat, P. V. Band filling with free charge carriers in organometal halide perovskites. *Nat. Photonics* **8,** 737–743 (2014).

103. Smith, N. Classical generalization of the Drude formula for the optical conductivity. *Phys. Rev. B* **64,** 155106–5 (2001).

104. Nemec, H., Kuzel, P. & Sundstrom, V. Far-infrared response of free charge carriers localized in semiconductor nanoparticles. *Phys. Rev. B* **79,** 115309 (2009).

105. Cooke, D. G., Meldrum, A. & Uhd Jepsen, P. Ultrabroadband terahertz conductivity of Si nanocrystal films. *Appl. Phys. Lett.* **101,** 211107–1 (2012).

106. Sun, S. *et al.* The origin of high efficiency in low-temperature solution-processable bilayer organometal halide hybrid solar cells. *Energy Environ. Sci.* **7,** 399–407 (2014).

107. Hirasawa, M., Ishihara, T., Goto, T., Uchida, K. & Miura, N. Magnetoabsorption of the lowest exciton in perovskite-type compound (CH3NH3)PbI3. *Phys. B* **201,** 427–430 (1994).

108. Lin, Q. *et al.* Electro-optics of perovskite solar cells. *Nature Photonics* **9,** 106–112 (2014).

109. Quarti, C. *et al.* The Raman Spectrum of the CH3NH3PbI3 Hybrid Perovskite: Interplay of Theory and Experiment. *J. Phys. Chem. Lett.* **5,** 279–284 (2014).

110. Gottesman, R. *et al.* Extremely Slow Photoconductivity Response of CH3NH3PbI3 Perovskites Suggesting Structural Changes under Working Conditions. *J. Phys. Chem. Lett.* 2662–2669 (2014).

111. Hoke, E. T. *et al.* Reversible photo-induced trap formation in mixed-halide hybrid perovskites for photovoltaics. *Chem. Sci.* **6,** 613–617 (2015).

112. Unger, E. L. *et al.* Hysteresis and transient behavior in current-voltage measurements of hybrid-perovskite absorber solar cells. *Energy Environ. Sci.* **7,** 3690–3698 (2014).

113. Feng, J. & Xiao, B. Crystal Structures, Optical Properties, and Effective Mass Tensors of CH3NH3PbX3 (X = I and Br) Phases Predicted from HSE06. *Phys. Chem. Lett.* **3,** 1278−1282 (2014).

114. Störmer, H. L., Gossard, A. C., Wiegmann, W. & Baldwin, K. Dependence of electron mobility in modulation-doped GaAs-(AlGa)As heterojunction interfaces on electron density and Al concentration. *Appl. Phys. Lett.* **39,** 912–914 (1981).

115. Dane, W. *et al.* Impact of microstructure on local carrier lifetime in perovskite solar cells. *Science* **348,** 683–686 (2015).

116. Kutes, Y. *et al.* Direct Observation of Ferroelectric Domains in Solution-Processed. *J. Phys. Chem. Lett.* **5,** 3335−3339 (2014).

117. Frost, J. M. *et al.* Atomistic origins of high-performance in hybrid halide perovskite solar cells. *Nano Lett.* **14,** 2584–2590 (2014).

118. Oga, H., Saeki, A., Ogomi, Y., Hayase, S. & Seki, S. Improved Understanding of the Electronic and Energetic Landscapes of Perovskite Solar Cells: High Local Charge Carrier Mobility, Reduced Recombination, and Extremely Shallow Traps. *J. Am. Chem. Soc* **136,** 13818–13825 (2014).

119. Vittoria Roiati, Edoardo Mosconi, Andrea Listorti,Silvia Colella,Giuseppe Gigli, and F. D. A. Stark Effect in Perovskite/TiO2 Solar Cells: Evidence of Local Interfacial Order. *Nano Lett.* **14,** 2168–2174 (2014).

120. Grischkowsky, D., Keiding, S., Exter, M. Van & Fattinger, C. Far-infrared time-domain spectroscopy with terahertz beams of dielectrics and semiconductors. *J. Opt. Soc. Am. B* **7,** 2006–2015 (1990).

121. Thomson, M. D., Kreß, M., Löffler, T. & Roskos, H. G. Broadband THz emission from gas plasmas induced by femtosecond optical pulses: From fundamentals to applications. *Laser Photonics Rev.* **1,** 349–368 (2007).

122. D'Angelo, F., Parekh, S. H., Bonn, M. & Turchinovich, D. Self-referenced Transient THz Spectroscopy with ABCD Detection. *J. Opt. Soc. Am.* **1,** 1–2 (2015).

123. Dressel, M. & Grüner, G. *Electrodynamics of Solids*. (Cambridge University Press, 2002).

124. Jellison, G. E. & Modine, F. A. Optical constants for silicon at 300 and 10 K determined from 1.64 to 4.73 eV by ellipsometry. *J. Appl. Phys.* **53,** 3745–3753 (1982).

125. Van Exter, M. & Grischkowsky, D. Carrier dynamics of electrons and holes in moderately doped silicon. *Phys. Rev. [Sect.] B* **41,** 12140–12149 (1990).

126. Jeon, T.-I. & Grischkowsky, D. Nature of Conduction in Doped Silicon. *Phys. Rev. Lett.* **78,** 1106–1109 (1997).

127. Mosconi, E., Quarti, C., Ivanovska, T., Ruani, G. & De Angelis, F. Structural and electronic properties of organo-halide lead perovskites: a combined IR-spectroscopy and ab initio molecular dynamics investigation. *Physical chemistry chemical physics : PCCP* **16,** 16137–44 (2014).

128. Asbury, J. B., Hao, E., Wang, Y., Ghosh, H. N. & Lian, T. Ultrafast Electron Transfer Dynamics from Molecular Adsorbates to Semiconductor Nanocrystalline Thin Films. *J. Phys. Chem. B* **105,** 4545–4557 (2001).

129. Akimov, A. V, Neukirch, A. J. & Prezhdo, O. V. Theoretical Insights into Photoinduced Charge Transfer and Catalysis at Oxide Interfaces. *Chem. Rev.* **113,** 4496–4565 (2013).

130. Tachibana, Y., Moser, J. E., Grätzel, M., Klug, D. R. & Durrant, J. R. Subpicosecond Interfacial Charge Separation in Dye-Sensitized Nanocrystalline Titanium Dioxide Films. *J. Phys. Chem* **100,** 20056–20062 (1996).

131. Moser, J. E. *et al.* Comment on ' Measurement of Ultrafast Photoinduced Electron Transfer from Chemically Anchored Ru - Dye Molecules into Empty Electronic States in a Colloidal Anatase TiO2 Film '. *J. Phys. Chem* **102,** 3649–3650 (1998).

132. T. Hannappel, B. Burfeindt, W. S. Measurement of Ultrafast Photoinduced Electron Transfer from Chemically Anchored Ru - Dye Molecules into Empty Electronic States in a Colloidal Anatase TiO2 Film ". *J. Phys. Chem. B* **101,** 6799–6802 (1997).

133. Cánovas, E., Wang, H., Karakus, M. & Bonn, M. Hot electron transfer from PbSe quantum dots molecularly bridged to mesoporous tin and titanium oxide films. *Chem. Phys.* **471,** 54–58 (2016).

134. Gordon M. Turner, Matthew C. Beard, C. A. S. Carrier Localization and Cooling in Dye Sensitized Nanocrystalline Titanium Dioxide. *J. Phys. Chem. B* **106,** 11716–11719 (2002).

135. Harlang, T. C. B. *et al.* Iron sensitizer converts light to electrons with 92% yield. *Nature Chemistry* **7,** 883–889 (2015).

136. Tiwana, P., Parkinson, P., Johnston, M. B., Snaith, H. J. & Herz, L. M. Ultrafast terahertz conductivity dynamics in mesoporous TiO2: Influence of dye sensitization and surface treatment in solid-state dye-sensitized solar cells. *J. Phys. Chem. C* **114,** 1365–1371 (2010).

137. Luitel, T. & Zamborini, F. P. Covalent Modi fi cation of Photoanodes for Stable Dye-Sensitized Solar Cells. *Langmuir* **29,** 13582−13594 (2013).

138. Kohle, B. O., Gratzel, M. & Meyer, T. B. The Photovoltaic Stability of Bis(isothiocyanato)ruthenium(II)-bis-2,2'-bipyridine-4,4'-dicarboxylic acid and related sensitizers. *Adv. Mater.* **9,** 904–906 (1997).

139. Thomalla, M. & Tributsch, H. Chromatographic studies of photodegradation of RuL2(SCN)2 in nanostructured dye-sensitization solar cells. *C. R.Chimie* **9,** 659–666 (2006).

140. K. Vinodgopal, Xiao Hua, Robin L. Dahlgren, A. G. Lappin, L. K. Patterson, P. V. K. Photochemistry of Ru(bpy)2(dcbpy)2+ on Al203 and Ti02 Surfaces. An Insight into the Mechanism of Photosensitization. *J. Phys. Chem* **2,** 10883–10889 (1985).

141. Kaes, C., Katz, A. & Hosseini, M. W. Bipyridine: The most widely used ligand. A review of molecules comprising at least two 2,2'-bipyridine units. *Chem. Rev.* **100,** 3553–3590 (2000).

142. Sebastiano Campagna, Fausto Puntoriero, Francesco Nastasi, Giacomo Bergamini, V. B. Photochemistry and Photophysics of Coordination Compounds : Ruthenium. *Top Curr Chem* **280,** 117–214 (2007).

143. Nazeeruddin, M. K., Humphry-Baker, R., Liska, P. & Grätzel, M. Investigation of Sensitizer Adsorption and the Influence of Protons on Current and Voltage of a Dye-Sensitized Nanocrystalline TiO 2 Solar Cell. *J. Phys. Chem. B* **107,** 8981–8987 (2003).

144. Pe, C., Kador, L., Peng, B. & Thelakkat, M. Characterization of the Adsorption of Ru-bpy Dyes on Mesoporous TiO 2 Films with UV - Vis , Raman , and FTIR Spectroscopies.

J. Phys. Chem. B **110,** 8723–8730 (2006).

145. Murakoshi, K. *et al.* Importance of binding states between photosensitizing molecules and the TiO2 surface for efficiency in a dye-sensitized solar cell. *Journal of Electroanalytical Chemistry* **396,** 27–34 (1995).

146. Nara, M., Torii, H. & Tasumi, M. Correlation between the vibrational frequencies of the carboxylate group and the types of its coordination to a metal ion: An ab initio molecular orbital study. *J. Phys. Chem.* **100,** 19812–19817 (1996).

147. Finnie, K. S., Bartlett, J. R. & Woolfrey, J. L. Vibrational Spectroscopic Study of the Coordination of (2,2‘-Bipyridyl-4,4‘-dicarboxylic acid)ruthenium(II) Complexes to the Surface of Nanocrystalline Titania. *Langmuir* **14,** 2744–2749 (1998).

148. Schnadt, J. *et al.* Experimental evidence for sub-3-fs charge transfer from an aromatic adsorbate to a semiconductor. *Nature* **418,** 620–623 (2002).

149. Schnadt, J. *et al.* Excited-state charge transfer dynamics in systems of aromatic adsorbates on TiO2 studied with resonant core techniques. *J. Chem. Phys.* **119,** 12462–12472 (2003).

150. Odelius, M., Persson, P. & Lunell, S. Bi-isonicotinic acid on rutile (1 1 0): Calculated molecular and electronic structure. *Surface Science* **529,** 47–58 (2003).

151. Schnadt, J. *et al.* Adsorption and Charge-Transfer Study of Bi-isonicotinic Acid on In Situ-Grown Anatase. *J. Phys. Chem. B* **2,** 3114–3122 (2004).

152. Lee, K. E., Gomez, M. A., Regier, T., Hu, Y. & Demopoulos, G. P. Further Understanding of the Electronic Interactions between N719 Sensitizer and Anatase TiO2 Films: A Combined X-ray Absorption and X-ray Photoelectron Spectroscopic Study. *J. Phys. Chem. C* **115,** 5692–5707 (2011).

153. Sánchez-de-Armas, R., San-Miguel, M. A., Oviedo, J. & Sanz, J. F. Direct vs. indirect mechanisms for electron injection in DSSC: Catechol and alizarin. *J. Phys. Chem. C* **115,** 11293–11301 (2011).

154. Furube, A. *et al.* Ultrafast direct and indirect electron-injection processes in a photoexcited dye-sensitized nanocrystalline zinc oxide film: The importance of

exciplex intermediates at the surface. *Journal of Physical Chemistry B* **108,** 12583–12592 (2004).

155. Jepsen, P. U., Cooke, D. G. & Koch, M. Terahertz spectroscopy and imaging - Modern techniques and applications. *Laser Photonics Rev.* **5,** 124–166 (2011).

156. Hashimoto, K., Irie, H. & Fujishima, A. TiO2 Photocatalysis: A Historical Overview and Future Prospects. *Jpn. J. Appl. Phys.* **44,** 8269–8285 (2005).

157. Francisco M. Gómez-Campos, M. C. Hole Surface Trapping in CdSe Nanocrystals: Dynamics, Rate Fluctuations, and Implications for Blinking. *Nano Lett.* **12,** 4508–4517 (2012).

158. Dmitri V. Talapin, James H. Nelson, Elena V. Shevchenko, S. A. & Bryce Sadtler, A. P. A. Seeded Growth of Highly Luminescent CdSe / CdS Nano-Heterostructures with Rod and Tetrapod Morphologies. *Nano Lett.* **7,** 2951–2959 (2008).

159. Marcus, R. a. On the Theory of Electron-Transfer Reactions. VI. Unified Treatment for Homogeneous and Electrode Reactions. *J. Chem. Phys.* **43,** 679 (1965).

160. Gerischer, H. Electron-transfer kinetics of redox reactions at the semiconductor/electrolyte contact. A new approach. *J. Phys. Chem.* **95,** 1356–1359 (1991).

161. Wu, K., Zhu, H. & Lian, T. Ultrafast Exciton Dynamics and Light-Driven H2 Evolution in Colloidal Semiconductor Nanorods and Pt-Tipped Nanorods. *Acc. Chem. Res.* **48,** 851–859 (2015).

162. Yang, Y., Wu, K., Chen, Z., Jeong, B.-S. & Lian, T. Competition of branch-to-core exciton localization and interfacial electron transfer in CdSe tetrapods. *Chem. Phys.* **471,** 32–38 (2015).

163. Jing, P. *et al.* Ultrafast carrier dynamics and hot electron extraction in tetrapod-shaped CdSe nanocrystals. *ACS Appl. Mater. and Interfaces* **7,** 7938–7944 (2015).

164. Kaifeng Wu, Zheyuan Chen, Hongjin Lv, Haiming Zhu, Craig L Hill, and T. L. Hole Removal Rate Limits Photodriven H2 Generation Efficiency in CdS-Pt and CdSe/CdS-Pt Semiconductor Nanorod−Metal Tip Heterostructures. *J. Am. Chem. Soc* **136,** 7708–

7716 (2014).

165. Jensen, S. A. *et al.* Ultrafast Photoconductivity of Graphene Nanoribbons and Carbon Nanotubes. *Nano Lett.* **13,** 5925–5930 (2013).

166. Klimov, V. I. Optical Nonlinearities and Ultrafast Carrier Dynamics in Semiconductor Nanocrystals. *J. Phys. Chem. B* **104,** 6112–6123 (2000).

167. Nestor Guijarro, Qing Shen, Sixto Gimenez, IvaMora-Sero, Juan Bisquert, Teresa Lana-Villarreal, Taro Toyoda, R. G. Direct Correlation between Ultrafast Injection and Photoanode Performance in Quantum-Dot Sensitized Solar Cells. *J. Phys. Chem. C* **114,** 22352–22360 (2010).

168. Wu, K., Zhu, H., Liu, Z., Rodríguez-Córdoba, W. & Lian, T. Ultrafast charge separation and long-lived charge separated state in photocatalytic CdS-Pt nanorod heterostructures. *J. Am. Chem. Soc* **134,** 10337–10340 (2012).

169. Shao, M., Peles, A. & Shoemaker, K. Electrocatalysis on Platinum Nanoparticles : Particle Size Effect on Oxygen Reduction Reaction Activity. *Nano Lett.* **11,** 3714–3719 (2011).